ABSTRACT

ZHOU, TONG. Benchmarking Thermal Neutron Scattering in Graphite. (Under the guidance of Prof. Ayman I. Hawari.)

The Very High Temperature Reactor (VHTR), one of the Generation IV reactor concepts, is a helium-cooled, graphite-moderated nuclear reactor with a core temperature reaching 1000˚C. It can provide high quality process heat for hydrogen production beside power generation and will become deployable around 2030. At such temperatures, graphite is an appropriate neutron moderator material due to its high sublimation temperature and high temperature strength. Furthermore, graphite has a large heat capacity and stable structure due to its large thermal inertia. However, the current thermal neutron cross-section libraries of graphite are based on models and data developed in the 1950s and 1960s. Significant discrepancies between measurements and the computational predictions of these libraries were observed. As a result, a study was performed in this dissertation to benchmark modern and traditional thermal neutron scattering libraries of graphite.

In this work, a Slowing-Down-Time experiment was designed and performed at the Oak Ridge National Laboratory (ORNL) by using the Oak Ridge Electron Linear Accelerator (ORELA) as a neutron source to study the neutron thermalization in graphite at room and higher temperatures. The MCNP5 code was utilized to simulate the detector responses and help optimize the experimental design including the size of the graphite assembly, furnace, shielding system and detector position. To facilitate such analysis, MCNP5 version 1.30 was modified to enable perturbation calculation using point detector type tallies. By using the modified MCNP5 code, the sensitivity of the experimental models to the graphite total thermal neutron cross-sections was studied to optimize the design of the experiment. Measurements of slowing-down-time spectrum in graphite were performed at room

temperature for a 70x70x70 cm graphite pile by using a Li-6 scintillator and a U-235 fission counter at different locations. The measurements were directly compared to Monte Carlo simulations that use different graphite thermal neutron scattering cross-section libraries. Simulations based on the ENDF/B-VI graphite library were found to have a 30%-40% disagreement with the measurements.

In addition to the graphite SDT experiment, which provided the data in the energy region above the graphite Bragg-cutoff energy, transmission experiments were performed for different types of graphite samples using the NIST 8.9 Å beam (located at NG-6) to investigating the energy region below the Bragg-cutoff energy. Measurements confirmed that reactor grade graphite, which is a two phase material (crystalline graphite and binder (amorphous-like) carbon), has different thermal neutron scattering cross section from pyrolytic graphite (crystalline graphite). Specifically, the transmission measurements gave a 8.9 Å neuron totals cross section of 1.40±0.03 barns for pyrolytic graphite and 0.61±0.05 for reactor grade graphite.

The experiments presented in this work compliment each other and provide an experimental data set which can be used to benchmark graphite thermal neutron scattering cross section libraries that are generated using different methodologies. Further investigation is necessary to benchmark the thermal scattering cross section data at temperatures greater than room temperature.

Benchmarking Thermal Neutron Scattering in Graphite

by

Tong Zhou

A dissertation submitted to the Graduate Faculty of

North Carolina State University

In partial fulfillment of the

Requirements for the degree of

Doctor of Philosophy

Nuclear Engineering

Raleigh, NC

2006

Approved by:

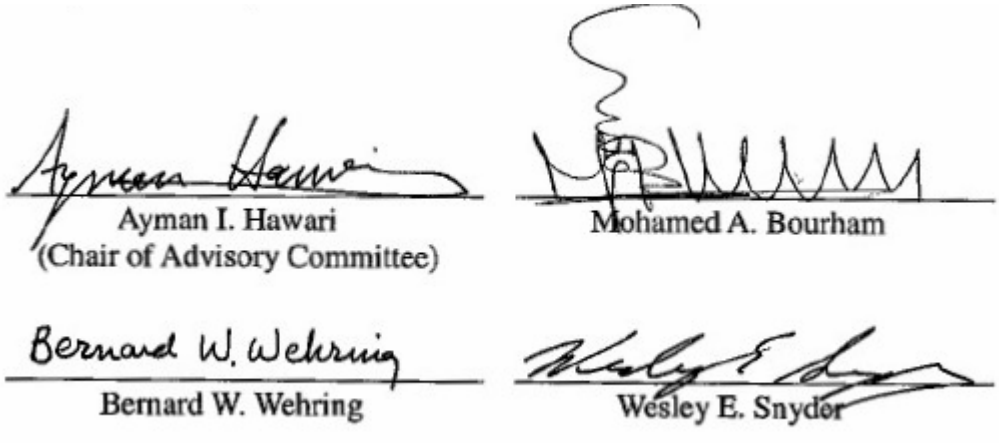

BIOGRAPHY

Tong Zhou was born in Shijiazhuang, China on February 22, 1977 and spent his youth there.

The author began attending Tsinghua University at Beijing China in 1995 and obtained a Bachelor of Science degree in Engineering Physics in 1999. After that, he continued his study in Tsinghua and received a Master of Science degree in Engineering Physics in 2001.

In 2001, the author went to Cincinnati University to study in the department of Nuclear Engineering for one quarter under Prof. Hawari's advisory. Right after that, he followed his advisor to move to North Carolina State University to continue his PhD program. Research interests included Monte Carlo simulation, nuclear instruments for radiation measurement, thermal neutron scattering, benchmarking experiment.

Along his study at NCSU, Tong Zhou married with Ruoyin Li in 2004.

ACKNOWLEDGMENTS

I would like to express my deepest appreciation to Dr. Ayman I. Hawari for his invaluable guidance and support through my five years PhD studying. His enthusiasm will always encourage me in my career life.

Also, I would like to highly appreciate Dr. Bernard W. Wehring for his advice and help. I did learn a lot from him and really enjoy the time we work together. I also want to thank Dr. Mohamed A. Bourham and Dr. Wesley E. Snyder for their comments and suggestions.

Special thanks to Dr. Paul Huffman for his support to my experiment at National Institute of Standard and Technology. As well, Dr. Victor Gillette and Iyad Al-Qasir are greatly appreciated for their collaboration and friendship.

Finally, I would like to dedicate this work to my beloved family, Ruoyin Li , Lingren Zhou and Yunshu Yue. Without their sacrifices and encouragement, I would not achieve anything.

Table of Contents

Page

List of Figures

List of Tables

Page

Chapter 1 Introduction

1.1 Very High Temperature Reactor (VHTR)

Generation IV reactor concepts are currently being investigated intensively [1] and will become deployable around 2030 (Figure1-1) [2]. Comparing to previous generation reactors, generation IV reactors improve nuclear safety and proliferation resistance, minimize long-lifetime radioactive nuclear waste as well as natural resource utilization and reduce capital costs. Initially 6 types of reactors are being considered for Generation IV technology. The Very High Temperature Reactor (VHTR), the Supercritical-Water-Cooled Reactor (SCWR) and the Molten Salt Reactor (MSR) are thermal reactors, while the Gas-Cooled Fast Reactor (GFR), the Sodium-Cooled Fast Reactor (SFR) and the Lead-Cooled Fast Reactor (LFR) are fast neutron reactors. Among them, the VHTR is being studied for power generation and for potentially providing high quality process heat for hydrogen production. [2]

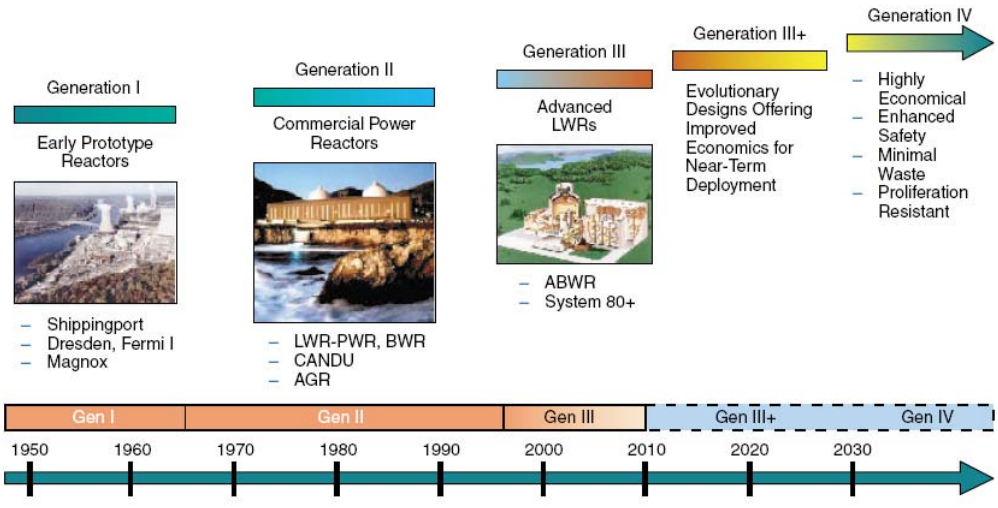

Figure 1-1. Roadmap for Generation IV nuclear reactors [2].

The Very High Temperature Reactor is a helium-cooled, graphite-moderated nuclear reactor (Figure 1-2) with either a "prismatic block" or a "pebble-bed" reactor core [2]. The high outlet temperature of helium gas coolant should reach 1000 degrees Celsius in order to improve the thermodynamics cycle economically and to achieve efficient hydrogen production via the thermal-chemical Sulfur-iodine cycle. At this temperature, most of the conventional neutron moderators such as water or heavy water fail. Graphite can withstand these conditions due to its high sublimation temperature (3652 – 3697 degrees Celsius) and high temperature strength. In addition, graphite can be used as a neutron moderator due to its low atomic mass and very low absorption cross-section and was used in the worlds first nuclear reactor built by Enrico Fermi at the University of Chicago in 1942 [3]. Furthermore, graphite has a large thermal inertia so that the reactor core composed of graphite has a large heat capacity and stable structure to make passive safety possible. All of these features make graphite appropriate for the Very High Temperature Reactor.

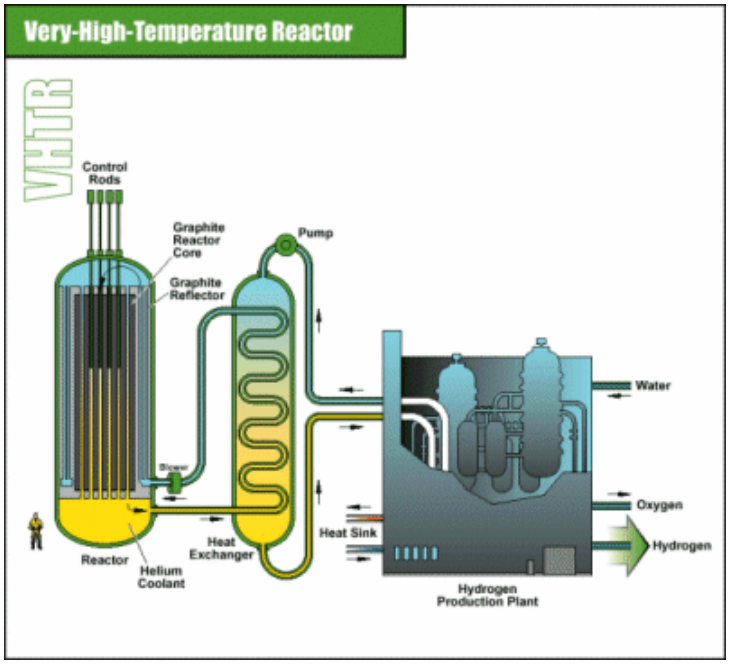

Figure 1-2. Very-High-Temperature Reactor [2].

Neurotically, the Mean Free Path of thermal or epithermal neutrons in graphite is 2.4cm, (compared to 0.29cm for thermal neutrons and 0.7cm for epithermal neutrons in water). In a "pebble-bed" VHTR core the fuel elements are sphere pebbles with 3 cm radius as shown in Figure 1-3 [4]. In a "prismatic block" VHTR core the fuel pins are 1.6 cm in diameter and 6 cm long [5]. The dimension of the fuel element in both types of VHTR is compatible to the neutron Mean Free Path in graphite. Hence, the neutrons generated from the fission chain reaction can have a collision with graphite moderator away from the current fuel element. From a neutronic point of view, the fine structure of the fuel element will not be seen. As a result, the graphite-moderated VHTR can be treated as a homogeneous reactor.

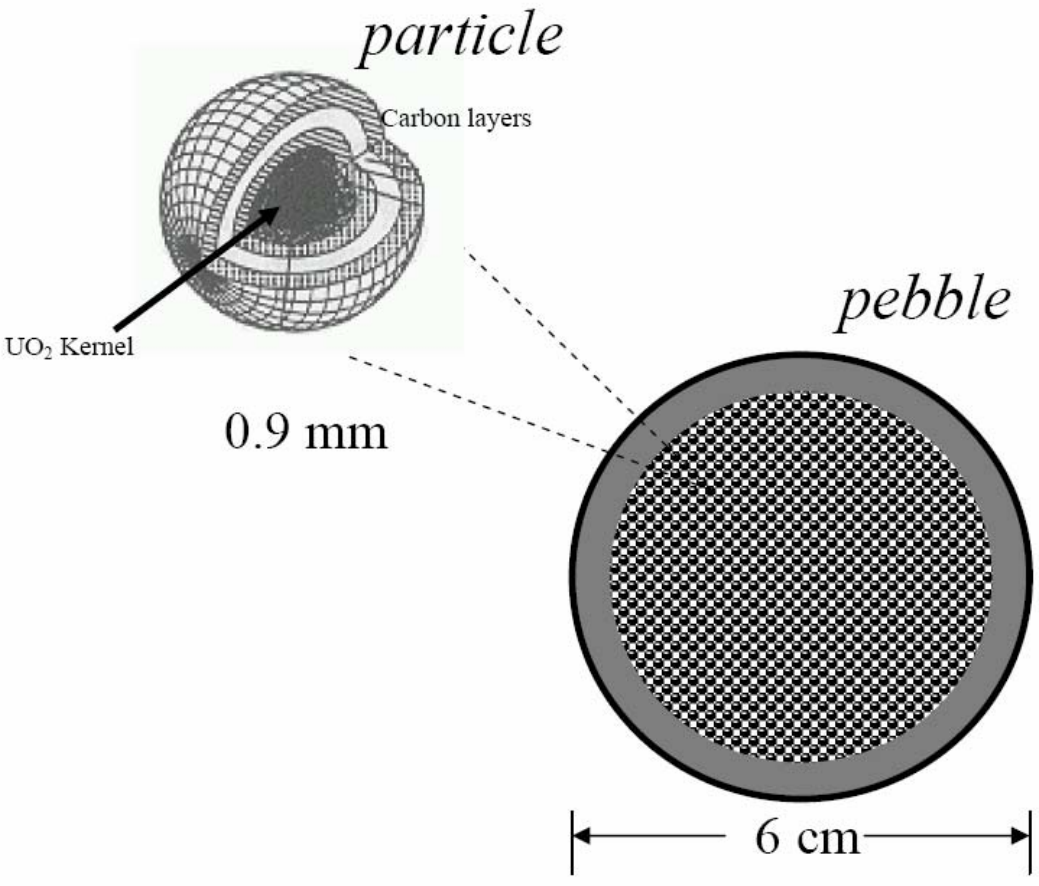

Figure 1-3. A schematic PBR fuel pebble [6].

This work focuses on establishing an improved understanding of the process of neutron thermalization in graphite. Recently, experiments were performed to validate the traditional cross section libraries and one generated [7] recently at North Carolina State University. It is anticipated that the use of more accurate thermal neutron scattering libraries for graphite in VHTR physics calculations will lead to improved utilization and safety performance for the reactors. The objective of this paper is to design and perform experiments to benchmark thermal neutron scattering in graphite at room and higher temperatures.

1.2 Graphite

As mentioned above, the VHTR is a thermal spectrum reactor. Prompt neutrons that are produced upon the fission of fuel nuclei, will slow-down and thermalize in the graphite moderator of the VHTR. At a moderator temperature of 1200 K it can be shown [8] that the average energy of the neutrons will be ~0.2eV. Neutron interactions in graphite (high to low energy) can be understood by studying the graphite neutron cross section data and libraries.

1.2.1 Graphite structure and manufacture

Graphite has a hexagonal crystal structure, shown in the Figure 1-4. There are two features, which make graphite unique. First, the large sheets of hexagonal rings are formed by strong chemical bonds. Second, the spaces between the carbon layer planes are relatively large and the forces between the layer planes are weak van der Waals forces. Based on the crystal structure, the density of graphite is predicted to be 2.26 g/cm^3 [9]. Pyrolytic graphite, which has a crystalline structure, can be made by heating a hydrocarbon nearly to its decomposition temperature, and permitting the graphite to crystallize (pyrolysis). The conventional method used to manufacture

graphite, which is called electrographite, is by using a petroleum-coke filler and coal-tar-pitch binder. The manufacturing process has been published in detail elsewhere [9-12]. Reactor grade graphite, which is used in the nuclear reactor as a neutron moderator, is produced by the similar method with some modifications. The impurities which have significant neutron absorption cross sections, such as boron, are excluded. Reactor grade graphite produced by this method from petroleum-coke has grain and pore structure, therefore its density, 1.5 to 1.8 g/cm^3 is less than the theoretical value. Each grain is a polycrystalline unit, as shown in Figure 1-5, and the grain does not only contain the crystalline graphite, but also some binder carbons. This complex structure is difficult to model to study its material properties, and the graphite sample with this structure will bring some difficulties to measurements, which will be discussed later.

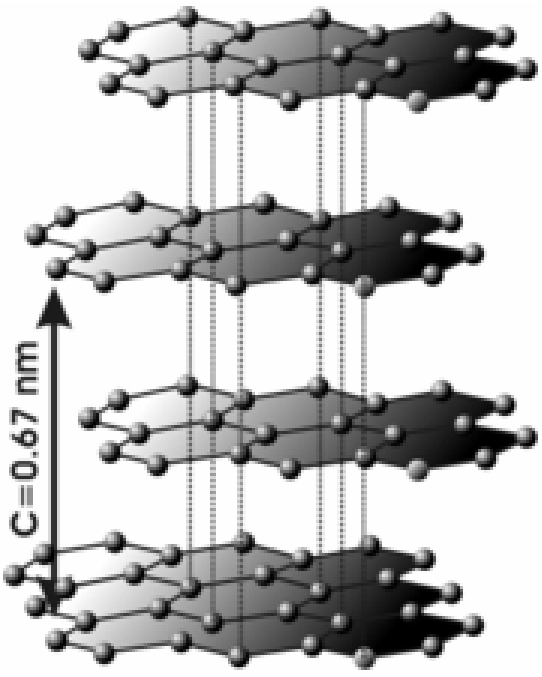

Figure 1-4. Graphite hexagonal crystal structure.

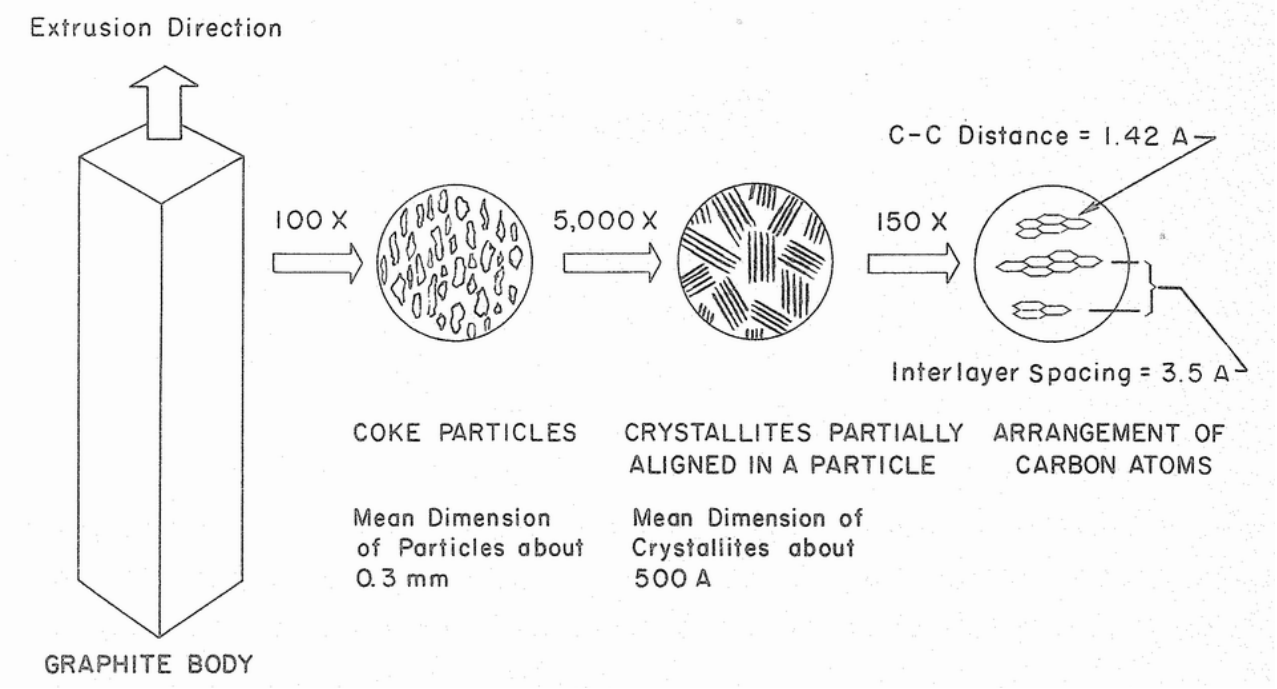

Figure 1-5. Artificial graphite structure [9].

1.2.2 Neutron cross section of graphite

For a thermal nuclear reactor, the thermal neutron density becomes critical for the safety and the optimization of the design. The thermal neutron density can be predicted by solving the neutron transport equation [8]:

$$\frac{1}{v}\frac{\partial \varphi}{\partial t}+\hat{\Omega}\cdot\nabla\varphi+\Sigma_t(\mathbf{r},E)\varphi(\mathbf{r},E,\hat{\Omega},t)=\int_{4\pi}d\hat{\Omega}'\int_0^{\infty}dE'\Sigma_s(E'\to E,\hat{\Omega}'\to\hat{\Omega})\varphi(\mathbf{r},E',\hat{\Omega}',t)+s(\mathbf{r},E,\hat{\Omega},t) \quad (1.1)$$

In which, $\Sigma_s(E'\to E,\hat{\Omega}'\to\hat{\Omega})$ is the neutron scattering double differential cross section of the moderator. In the VHTR at thermal energy, this term becomes the graphite thermal neutron scattering cross section, which is studied in this paper.

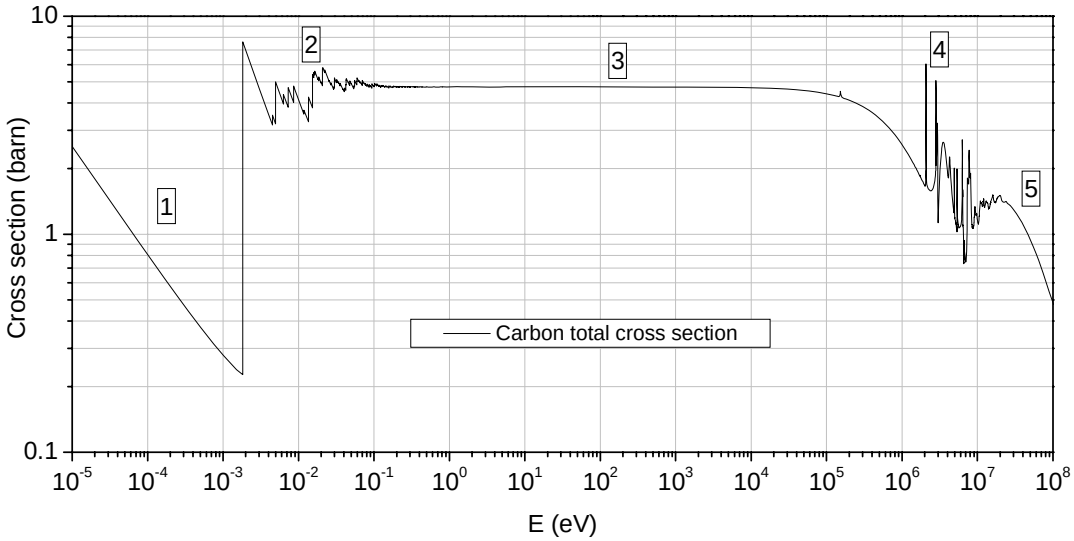

Figure 1-6. The total cross section of C [13].

When a neutron has a collision with a nucleus, a variety of nuclear reactions will happen depending on the neutron energy and the atomic mass of the nucleus. For example, Figure 1-6 shows the total neutron cross section of graphite (Carbon), which is combined by the free atom cross-section of natural carbon (above 4eV in Figure 1-6) and the thermal neutron cross-section of graphite material (below 4eV in Figure 1-6). There are 5 different energy regions labeled from 1 to 5 in Figure 1-6 [8]. The type of nuclear reaction depends on which region the interaction occurs in and therefore the behavior of the total neutron cross-section varies from region to region. Due to the neutrons extremely small wavelength above 20 MeV (region 5), the cross-section exhibits a large decrease as neutron energy goes up. This region has little relevance to the nuclear reactor because the emitting neutrons from the fission chain reaction barely exceed 10MeV. The spike behavior within the energy range 1 MeV to 20 MeV (region 4) is associated with the resonance reaction mechanisms and those peaks correspond to the nuclear energy levels in the

compound nucleus $^{13}_{6}C$. Such resonance structure will appear at the lower energy in the heavier nuclei since the nuclear energy levels in the heavy nucleus are lower than the light nucleus. In the energy region from 1 eV up to 0.1 MeV (region 3), potential scattering dominates. The cross-section has little variation and the incident neutrons are simply scattered elastically by nuclei just like billiard balls. The high-energy neutrons emitted from the fission chain reaction are slow down primarily by potential scattering. The jagged structure (region 2) below 1 eV until the sudden drop (the so-called Bragg cut-off energy, 0.2meV for the graphite) is also related to the wavelength of the neutron. When the neutron energy is sufficiently low so that the wavelength is comparable to the spacing of atoms in matter, neutrons will interact with an aggregate of nuclei instead of a single nucleus. For material with a regular crystalline structure (for example graphite), the neutrons will be diffracted when the neutron wavelength satisfies the Bragg condition:

$$\frac{\lambda}{\mathrm{N}} = 2\mathrm{d}\sin\theta \tag{1.2}$$

Where d is the space between various crystal lattice planes. This type of reaction is called Bragg elastic scattering. When the neutron energy is below the Bragg cut-off energy (region 1) the wavelength becomes so large that the Bragg condition can not be satisfied for any set of crystal lattice planes. Therefore in this region the coherent elastic scattering (i.e. Bragg scattering) will not be possible and only inelastic scattering can happen (the neutron absorption cross section is extremely low in this region), which behaves as 1/V. In addition, when the energy of the neutron is comparable to the chemical binding energy of atoms (~1eV), the incident neutrons can be down scattered (lose energy) or up scattered (gain energy) inelastically with an aggregate of nuclei and excite or relax the internal modes of the sample. In a crystalline material this represents the creation or absorption of phonons (i.e. lattice vibration). In a reactor, neutrons with energy lower

than 4eV are thermalized by inelastic collision because elastic collision does not allow energy transfer.

Conventionally neutrons are categorized into 3 groups depending on the energy of the neutrons. Fast neutrons range from 0.1 MeV to 20 MeV, epithermal neutrons from 1 eV to 0.1 MeV and slow neutrons below 1 eV. For slow neutrons (region 1 and 2), the thermal motion of the nuclei becomes comparable to the neutron motion and must be taken into account when studying interaction. The nuclei in thermal equilibrium at the temperature T can be essentially characterized by the thermal energy kT, and critically the neutrons with this thermal energy are called thermal neutrons. At room temperature (T=295K) the thermal energy is 0.025eV, while at the VHTR working temperature (T~1200K) the thermal energy is 0.1eV.

1.2.3 Status of graphite cross-section libraries

However, the majority of current thermal neutron scattering cross section libraries of graphite (ENDF/B-VI) and other moderator materials are based on the models and data which were developed in the 1950s and 60s [14]. In many circumstances the observed inconsistencies between the experimental measurement and the computational prediction remain unsolved. In case of graphite, disagreements between the experimental measurement and calculation based on ENDF/B-VI libraries were observed in reactor k-eff benchmarks [15] and a graphite Slowing-Down-Time experiment [16]. Additionally, Figure 1-7 and 1-8 show that the discrepancy in the graphite total thermal neutron cross section between some experimental data and the latest ENDF/B-VI library can be greater than 100%.

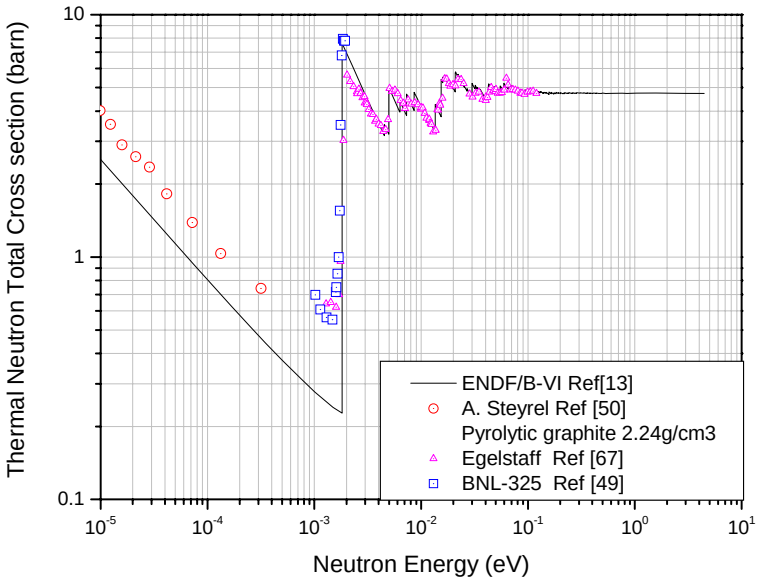

Figure 1-7. The measured total thermal neutron cross section of graphite and MCNP5 standard library at room temperature.

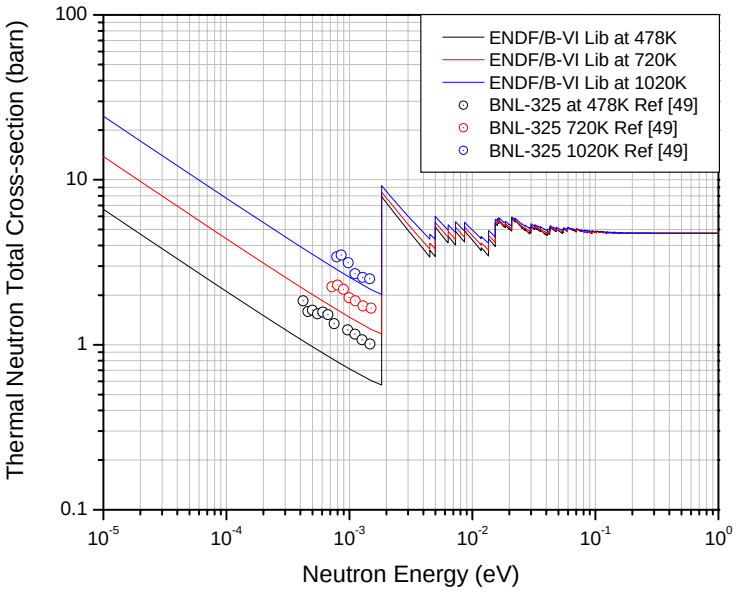

Figure 1-8. The measured total thermal neutron cross section of graphite and MCNP5 standard library at high temperatures.

The theoretical basis and fundamental data, on which the thermal neutron scattering libraries are based, are being critically evaluated and improved at North Carolina State University [7]. New thermal neutron cross-section libraries were generated for graphite and other moderator materials.

1.3 Experimentation

In this work, two experiments within different neutron energy regions (above and below the Bragg cut-off energy -- 2meV) were designed and performed. The experimental data were used to benchmark and evaluate the graphite thermal neutron scattering cross section libraries from ENDF/B-VI and ones generated by NCSU [7].

1.3.1 Slowing-Down-Time benchmark method

The Slowing-Down-Time (SDT) method was introduced by Bergman et al. in 1955 [17], which basically utilize the time and the neutron energy behavior of injecting a burst of neutrons into a moderating pile. Initially, the SDT method was applied to the "lead slowing down time spectrometer" (LSDTS) which was utilized to measure the neutron capture and fission cross section of samples inside a lead pile [17]. Later on, LSDTS was also used as a tool for the nondestructive assay of nuclear materials [18-21]. In addition, F. Maekawa and Y. Oyama in 1995 applied the SDT method to the shielding material stainless steel to perform a neutron spectrum measurement in the energy region around eV, which could be used to benchmark the neutron transport codes and data libraries [22, 23]. In 1999, a graphite Slowing-Down-Time spectrometer was built by A. Hawari, B. Wehring, H Radulescu, and N. Abdurrahman and utilized in the nondestructive assay of nuclear materials [16].

In this work, we explored the utilization of an accelerator-based pulsed neutron source (ORELA facility) to perform a Slowing-Down-Time experiment for studying the slowing down and thermalization of neutrons in graphite at temperatures extending from room temperature up to 1200 K, which is the core temperature of the Very High Temperature Gas Cool reactor. The measured neutron spectra were compared to the theoretical calculation based on the ENDF libraries and the thermal scattering cross section libraries generated by NCSU [7]. To study the sensitivity of the measured neutron slowing-down-time to the thermal scattering cross section library, the MCNP5 code has been modified and utilized to calculate the perturbations at the different temperatures with different setups. The design and set up of this experiment at the ORELA facility has been completed. Measurements at room temperature have been performed and measured data are presented and discussed. However, the execution of this experiment at high temperature awaits the completion of maintenance operations that are currently on going at ORELA.

Traditionally, the Time-Of-Flight method was utilized for measurement of thermal neutron spectra in graphite at different temperatures. For instant, in 1962 Parks el at measured thermal neutron steady-state energy spectra in a graphite pile at several temperatures by using time-of-flight techniques and the measured spectra were compared with theoretical predictions [26]. However, the measured energy range was thermal energy and the integral of the measured spectra were used to normalize the calculation. Therefore, only the shape of the measured spectra can be compared with calculation but not amplitude. Furthermore, the measured time-of-flight spectra need to be translated into energy spectra. On the other hand, by utilizing the Slowing-Down-Time technique, the evolution (in time) of the neutron energy spectrum in the moderator from the source energy

down to the thermal energy range can be monitored. The basic data collected during this experiment can be directly compared to computational predictions without the need for extensive processing that can introduce undesirable uncertainties. In addition, the fast neutron region in a measured time spectrum can be used to normalize computational predictions. That's because the fast neutron cross section of graphite is considered well known, calculations of fast neutron region in time spectrum are believable. The comparison between measurements and normalized calculations will give an indication about the thermal neutron scattering cross section library which is used in the calculations.

1.3.2 Transmission measurement

In the SDT experiment the source neutron can be slow down by the graphite pile to the range of several eV to 10 meV. While the other experiment, which is a 0.89 nm neutron transmission measurement, will provide the experimental data below the graphite Bragg cutoff energy 2 meV. In this energy region, the neutron coherent elastic collision is not possible, therefore the inelastic cross section is equal to the total cross section (ignore the absorption cross section), which can be calculated directly from the measured transmission. A number of measurement data are available in this energy region, and show a clear discrepancy from the ENDF library, as seen in the Figure 1-7 and 1-8. Nevertheless, some of these data are not accompanied by clear information of the sample, such as the type of the graphite and density, on which the cross-section highly depends upon. Consequently, the neutron monochromator in the cold neutron beam was utilized at the NIST Center for Neutron Research (NCNR) reactor to measure 0.89 nm neutron transmissions of different types of graphite samples, including reactor grade graphite and pyrolytic graphite.

Chapter 2 ORELA Slowing Down Time Experiment

2.1 Slowing-Down-Time theory

The idea of Slowing-Down-Time method can be illustrated by solving the neutron transport equation (equation 1.1) for the time-dependent neutron slowing down process in a moderator [24]. A pulse of fast neutrons injected into a moderator pile such as lead [17] or graphite [16], will begin to slow down by inelastic (if energetically allowed) and elastic scattering. Assuming the moderator pile is infinite and leakage is negligible, equation (1.1) can be integrated over $\mathbf{r}$ and $\hat{\mathbf{\Omega}}$ to get

$$\frac{1}{v}\frac{\partial \varphi}{\partial t} + \Sigma_t(E)\varphi(E,t) = \int_0^\infty dE' \Sigma_s(E' \to E)\varphi(E',t) + s(E,t) \tag{2.1}$$

For fast neutrons, the moderator atoms can be treated as free and at rest. Since inelastic collision only happens in very narrow neutron energy bands and fast neutrons slow down by elastic collision mainly, inelastic scattering can be neglected. Considering an elastic collision between a neutron of mass 1 and energy E' and a free moderator atom of mass A which is at rest initially, the neutron energy E can be calculated from energy and momentum conservation as:

$$E = \frac{1}{2}\left[(1+\alpha) + (1-\alpha)\cdot\cos\psi\right]\cdot E' \tag{2.2}$$

Where $\alpha = \left(\frac{A-1}{A+1}\right)^2$ and ψ is the angle between the initial direction of the incident neutron and the direction after the collision in center-of-mass frame of reference. For most moderators, the elastic scattering in center-of-mass system is isotropic below 1MeV (in case of graphite 1.4MeV) [24]. Therefore the probability density function of $\cos\psi$ is equal to 1/2. One can calculate the

elastic differential cross section as:

$$\Sigma_s(E' \to E) = \begin{cases} \dfrac{\Sigma_s(E')}{(1-\alpha)E'}, & E' < E < \alpha E' \\ 0, & otherwise \end{cases} \tag{2.3}$$

Since the elastic cross section of a moderator can be constant in a wide energy range, which is the case for graphite from 0.1MeV down to 1eV, by substituting equation (2.3) into equation (2.1), one can get,

$$\frac{1}{\mathrm{v}}\frac{\partial \varphi}{\partial \mathrm{t}} + \Sigma_{\mathrm{t}}(\mathrm{E})\varphi(\mathrm{E},\mathrm{t}) = \int_{\mathrm{E}}^{\mathrm{E}/\alpha} \mathrm{dE}' \frac{\Sigma_{\mathrm{s}}}{(1-\alpha)\mathrm{E}'}\varphi(\mathrm{E}',\mathrm{t}) + \mathrm{s}(\mathrm{E},\mathrm{t}) \tag{2.4}$$

Rewriting equation (2.4) in terms of neutron density $n(v,t) = \dfrac{\varphi(E,t)}{v}$ instead of flux φ(E,t),

$$\frac{\partial n(v,t)}{\partial t} = -v\Sigma_t(E)n(v,t) + \frac{2v\Sigma_s}{(1-\alpha)}\int_{v}^{v/\alpha} n(v',t)\frac{dv'}{v'} + s(v,t) \tag{2.5}$$

Assuming the source neutrons are fast neutron with energy in MeV range and are inject into the moderator pile as a very short pulse, the source term s(v,t) in equation (2.5) can be omitted and an asymptotic solution can be obtained which is valid for the neutron velocities much smaller than those of the source neutrons and slowing-down-time much later than the moment the source neutrons injected. Additionally, the neutron absorption cross sections of most moderators are very small. To simplify the equation, the absorption cross section is neglected and $\Sigma_t(E)$ is replaced by Σ_s. Let's introduce a new variable $x = v\Sigma_s t$ into equation (2.5),

$$\frac{d}{dx}[xn(x)] = -xn(x) + \frac{2x}{1-\alpha}\int_{x}^{x\sqrt{\alpha}} n(x')\frac{dx'}{x'} \tag{2.6}$$

Define the moments of n(x) by

$$M_l = \int_0^{\infty} x^l n(x)dx \tag{2.7}$$

Multiply equation (2.6) by x^{l-1} and integrate, one can get,

$$M_l = M_{l-1}\left[\frac{l-1}{1-\frac{2}{l+1}\cdot\frac{1-\alpha^{\frac{l+1}{2}}}{1-\alpha}}\right] \tag{2.8}$$

As normalization, $M_0 = \int_0^\infty n(x)dx$ is set to be equal to 1. Thus one can calculate,

$$\begin{aligned} M_1 &= \frac{2}{\xi} \\ M_2 &= A(A+2) \\ M_3 &= A^2(A+4) \\ M_4 &= A^3(A+20/3) \end{aligned} \tag{2.9}$$

Where ξ is defined as the average lethargy loss of every elastic collision between neutrons and moderator atoms.

$$\xi = \ln E' - \overline{\ln E} = \overline{\ln\left(\frac{E'}{E}\right)} = \int_{\alpha E'}^{E'} \ln\left(\frac{E'}{E}\right)\frac{dE}{(1-\alpha)E'} = 1+\frac{\alpha}{1-\alpha}\ln\alpha \tag{2.10}$$

Therefore, one can calculate the average quantity of velocities at a fixed time based on the moments of n(x) as:

$$\bar{v}(t) = \frac{\int_0^\infty x\cdot n(x)dx}{\Sigma_s t} = \frac{M_1}{\Sigma_s t} = \frac{2}{\xi\Sigma_s t} \tag{2.11}$$

$$\overline{v^2}(t) = \frac{M_2}{(\Sigma_s t)^2} \tag{2.12}$$

$$\overline{v^4}(t) = \frac{M_4}{(\Sigma_s t)^4} \tag{2.13}$$

Thus, at a fixed time, the average energy is given by,

$$\bar{E} = \frac{m\overline{v^2}}{2} = \frac{m \cdot M_2}{2(\Sigma_s t)^2} = \frac{m \cdot A(A+2)}{2(\Sigma_s t)^2} = \frac{constant}{t^2} \tag{2.14}$$

And its dispersion is given by,

$$\overline{\left(\frac{\Delta E}{E}\right)^2} = \frac{\overline{E^2} - \bar{E}^2}{\bar{E}^2} = \frac{8A-12}{3(A+2)^2} \tag{2.15}$$

When A>>1,

$$\overline{\left(\frac{\Delta E}{E}\right)^2} = \frac{8}{3A} \tag{2.16}$$

Equation (2.14) and (2.16) show that the average energy of neutrons in a slowing-down process is inversely proportional to the square of the slowing-down time and the energy spectrum at every time moment is distributed around Ē. For lead (A=204) $\sqrt{\overline{(\Delta E / E)^2}} \approx 11.4\%$, and for graphite (A=12) $\sqrt{\overline{(\Delta E / E)^2}} \approx 37.8\%$. Considering the above, if the neutron absorption cross section is negligible and the elastic scattering cross section is constant within certain energy region (such as graphite, region 3 in Figure 1-6), the neutrons with higher velocity will lose more energy by elastic scattering than the slower neutrons. Therefore an energy focusing effect will take place around Ē energies after a pulse [17].

Once the neutrons reach thermal energies, their interaction in a given moderator is described by a scattering law that contains the structural and dynamical information of the moderator. For a detector that is placed in the vicinity of the moderator pile, the time dependent reaction rate per atom is given by

$$R(t) = \int_E \sigma(E) \cdot \phi(E,t) dE \tag{2.17}$$

Where σ(E) is the microscopic cross section for the detection reaction, and φ(E, t) is the time and energy dependent neutron flux at the detector location. In addition to the time dependent response, this experiment can also yield information on the development of the energy spectrum as a function of the slowing-down-time. Using computational simulations, it is possible to determine the average energy of the neutrons during the slowing down process as

$$\overline{E}(t) = \int_E E \cdot \Psi(E,t) dE \tag{2.18}$$

where ψ(E,t) is the time-dependent neutron energy spectrum normalized to unity. Using the above expression, the time-energy correlation can be developed computationally and used as a guide in the benchmarking process. [25]

The objective of the benchmark experiment is to measure an integral quantity, i.e. a neutron time spectrum, which can be compared to the theoretical predictions based on certain thermal neutron scattering cross section libraries.

2.2 ORELA facility

The Oak Ridge Electron Linear Accelerator facility (ORELA, shown in Figure 2-1) is the proposed neutron source for this experiment. In the past, ORELA has been utilized extensively to measure the neutron total and capture cross-sections of numbers of samples by using the Time-Of-Flight method [27, 28, 29]. This facility, located in the Physics Division of Oak Ridge National Laboratory, consists of a 180-MeV electron accelerator, neutron producing targets, and buried and evacuated flight tubes up to 200 m long leading to underground detector locations. The neutrons are produced using the bremsstrahlung photons that are generated by the interaction of the 180 MeV electron beam with a tantalum target. It has a maximum neutron source strength

of ~$5x10^{18}$ n/s (at the target) and a maximum frequency of 1000 Hz. It produces intense nanosecond bursts of neutrons, each burst containing neutrons with energies from 10^{-3} to 10^{8} eV [30]. Figure 2-1 illustrates the basement of ORELA facility and the location of our experiment setup.

Furthermore, upon analyzing the ORELA energy spectrum it was found that despite its spread, it is in effect, a fast neutron spectrum peaking around 600 keV [31]. This only becomes apparent if the spectrum is expressed as $\varphi(\ln(E))$ vs. E as opposed to the usual $\varphi(E)$ vs. E, as shown in the Figure 2-2. However, as it can be seen in the Figure 2-2, small but significant high energy ($\geq$ 10 MeV) and low energy ($\leq$ 0.1 eV) components remain evident in the spectrum.

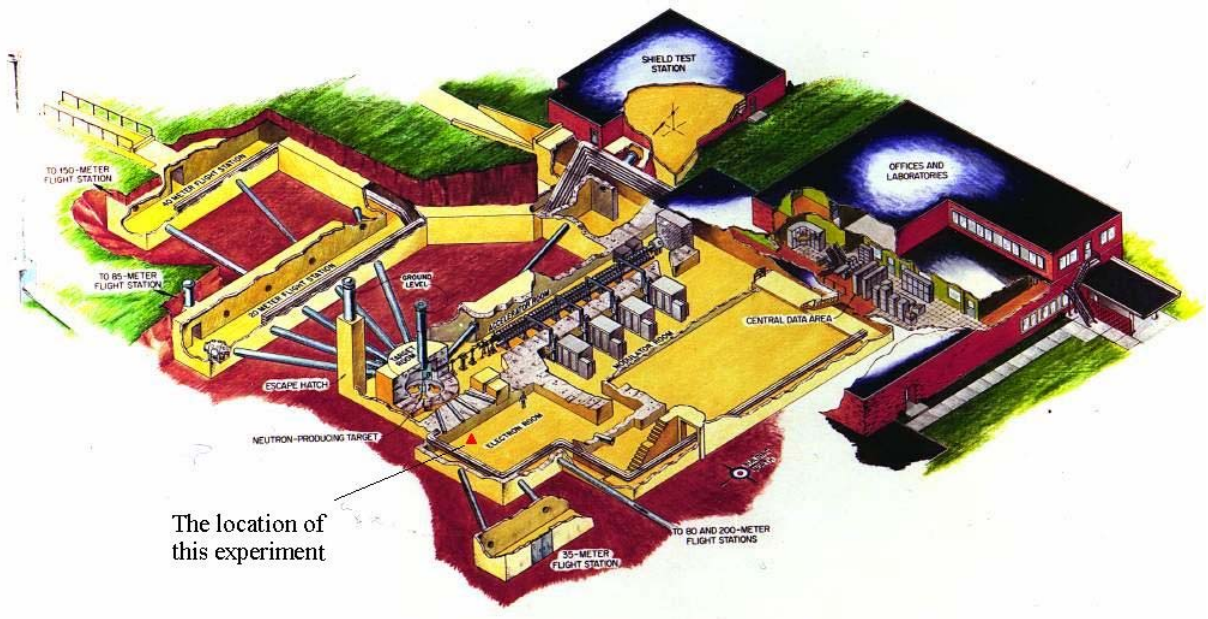

Figure 2-1. The ORELA facility.

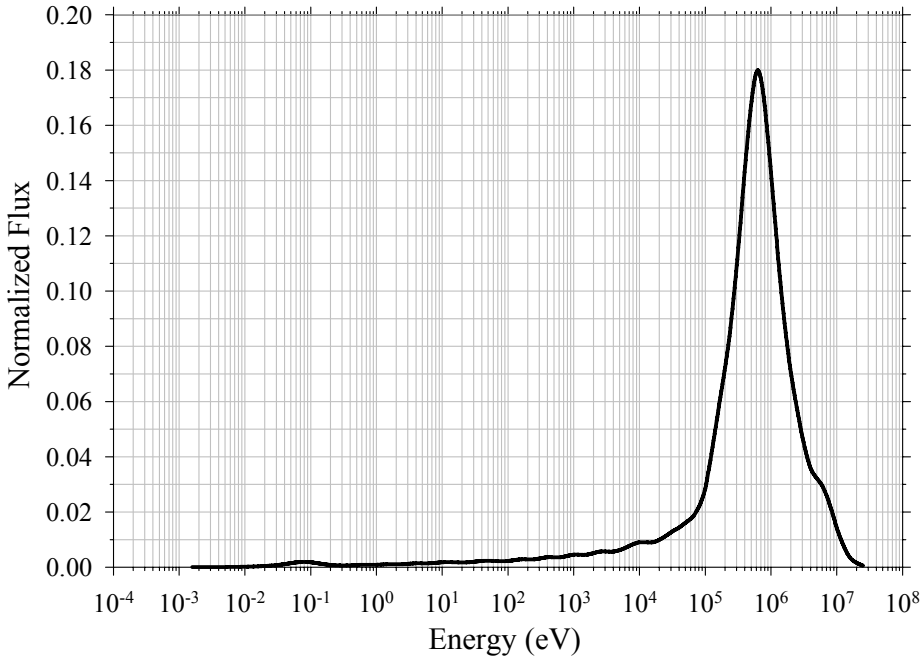

Figure 2-2. The ORELA neutron energy spectrum expressed as flux per unit ln(E).

2.3 MCNP simulation

The Monte Carlo code MCNP (Monte Carlo N-Particles) version 5 and its ENDF/B-VI-based cross-section libraries were used in this experiment to perform neutron transport calculations in order to study the slowing down of neutrons in a graphite moderator. MCNP is a 3-D transport code that utilizes combinatorial geometry and continuous-energy cross-section libraries [32]. At the starting point of this work, a simplified MCNP5 model was designed to simulate the experiment. The model was based on introducing a neutron pulse at the surface of a cubical graphite assembly[1] and monitoring the energy-time dependent neutron flux in a detector. A detector could be placed outside the assembly at a distance of about 46 cm from the surface

[1] In this work 1 x 1 x 1 m, 70 x 70 x 70 cm, and 50 x 50 x 50 cm graphite assemblies have been studied. The effect of assembly size will be discussed later in this report.

opposite to the source (back detector) or from the top surface of the assembly (top detector). In addition, there are three types of neutron detectors available; a Pu-239 fission chamber, a U-235 fission chamber and two Li-6 scintillators. At this stage, the Pu-239 fission chamber placed on the back will be discussed. At various time intervals after the neutron source pulse, the neutron flux was folded with the fission cross sections of Pu-239 to produce the integral time-dependent reaction rate per atom. Since the energy spectrum is a function of the slowing-down time, the time-dependent reaction rate per atom for a given fission detector will reflect the energy dependence of its fission cross section, as described in section 2.1.

In MCNP, the point detector, known as "next-event estimator", is a deterministic estimate of the flux at a point. Contributions to the point detector tally are made from every source or collision event. Therefore, the point detector tally can yield much better statistics than the track length tally with the same number of histories. In addition, most of the neutron collisions in this experiment happened inside the graphite assembly, while the detector is outside the assembly and away from the collision and the source points. As a result, the point detector tally was utilized in this experiment.

To create a realistic model, it was assumed that the graphite assembly would be located at the end of one of ORELA's beam tubes. Therefore, to ensure maximum source intensity, the shortest beam tube, which is 10 m long, was chosen. In addition, a pulsed neutron source was chosen with a 20-nanosecond pulse width and a 130 Hz frequency. Under such conditions, the source strength at the surface of the assembly is expected to be approximately 5×10^7 n/s. Figure 2-3 shows a schematic of the MCNP simulation model described above.

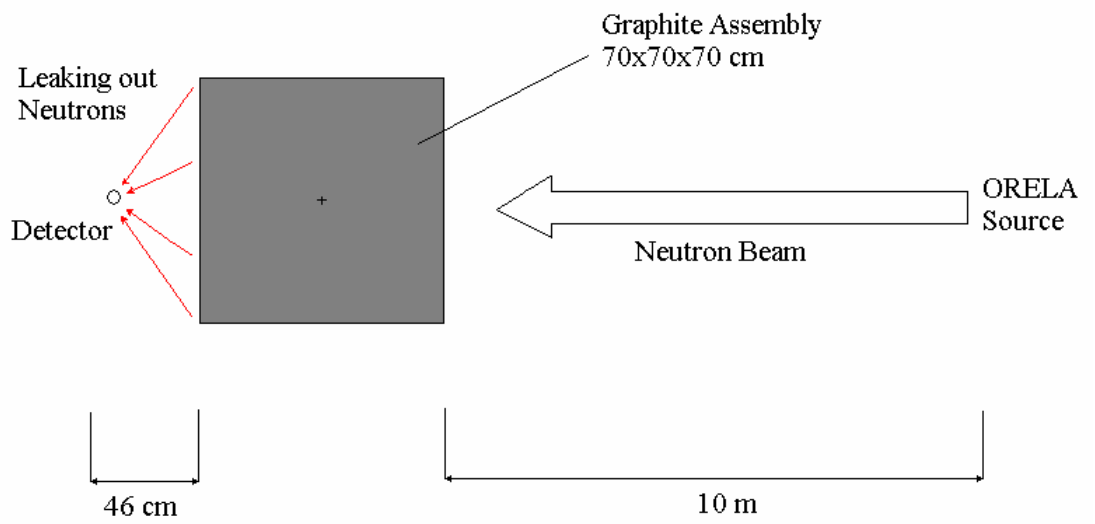

Figure 2-3. A schematic of the MCNP model.

Figure 2-4 shows the time dependent reaction rate in the Pu-239 back detector (i.e., the time spectrum). The general features of the time spectrum are dictated by the time dependent neutron energy spectrum that is leaking from the assembly and the energy dependent fission cross-section of Pu-239. The close coupling of the leakage energy spectrum to the time after the neutron pulse can be predicted based on the principals of time dependent neutron slowing down theory discussed earlier. Figure 2-5 gives a 3-dimentional map of the temporal evolution of the neutron energy spectrum as the neutrons slow down in the graphite moderator. As it can be seen in Figure 2-5, at early times the neutrons have a wide energy distribution. However, as time progresses, the spectrum becomes narrow due to a "focusing effect" that takes place if the moderator has a negligible absorption cross-section and a near constant elastic scattering cross-section [17]. For graphite the focusing effect is clear in the range extending from around 10 keV to 1 eV.

To quantify the slowing down process, equation (2.18) was used to calculate the average energy of the neutrons at the detector location for various times after the pulse. A code written in Visual Basic Application (VBA) was developed to calculate the average neutron energies at every

moment, which is attached in Appendix D. Figure 2-6 gives the results of this analysis. It can be seen that in the time period between 0.3 – 0.4 μs, the average energy of the neutron spectrum is in the range of 5 – 7 MeV, which corresponds to peak 1 in the spectrum of Figure 2-4. This observation is consistent with the source spectrum of ORELA (shown in Figure 2-2), which has a visible component at such high energies.

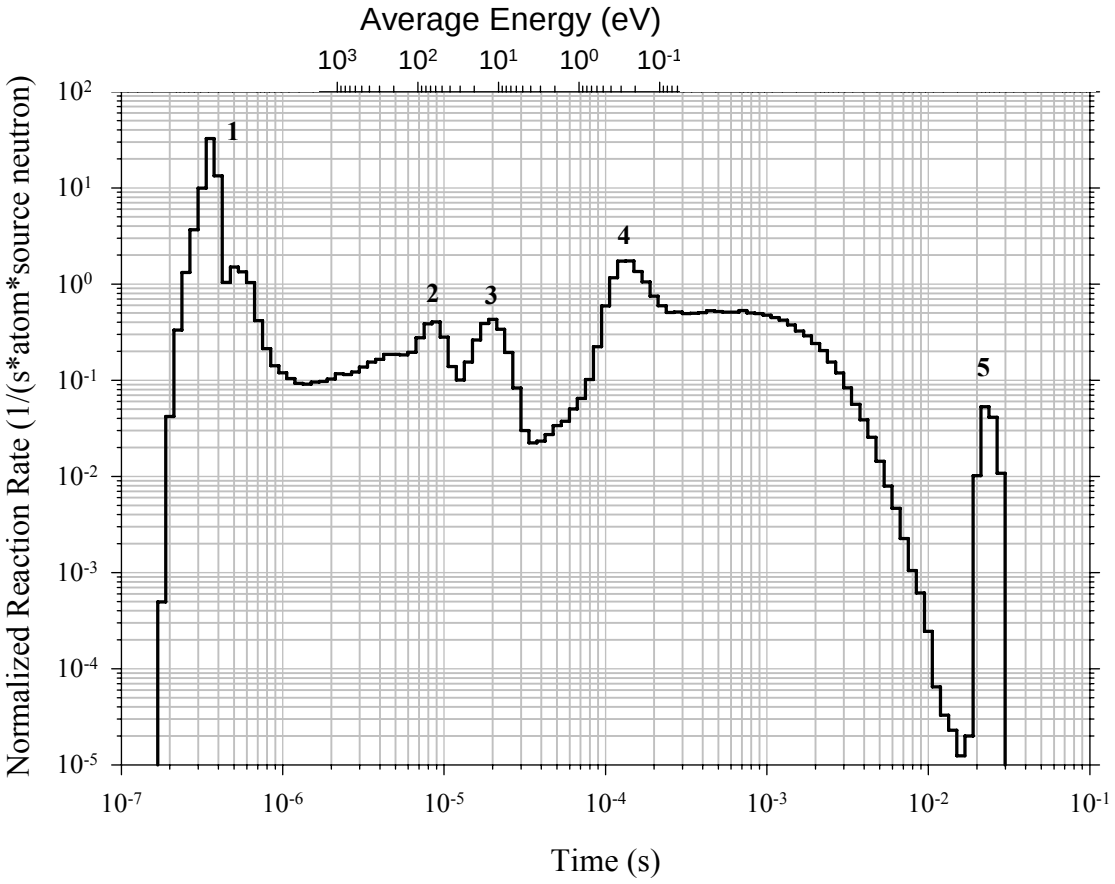

Figure 2-4. The calculated time dependent reaction rate for a Pu-239 detector located at 46 cm from the surface of the assembly opposite to the neutron source. The peak labeled 1 is a source peak with energy 5 to 7MeV. The peaks labeled 2, 3, and 4 correspond to resonance groups and/or resonances in the Pu-239 fission cross-section at approximately 40-300 eV, 8-30 eV, and 0.3 eV respectively. Peak 5 is also a source peak with energy below the Bragg cutoff of graphite, 1-2meV.

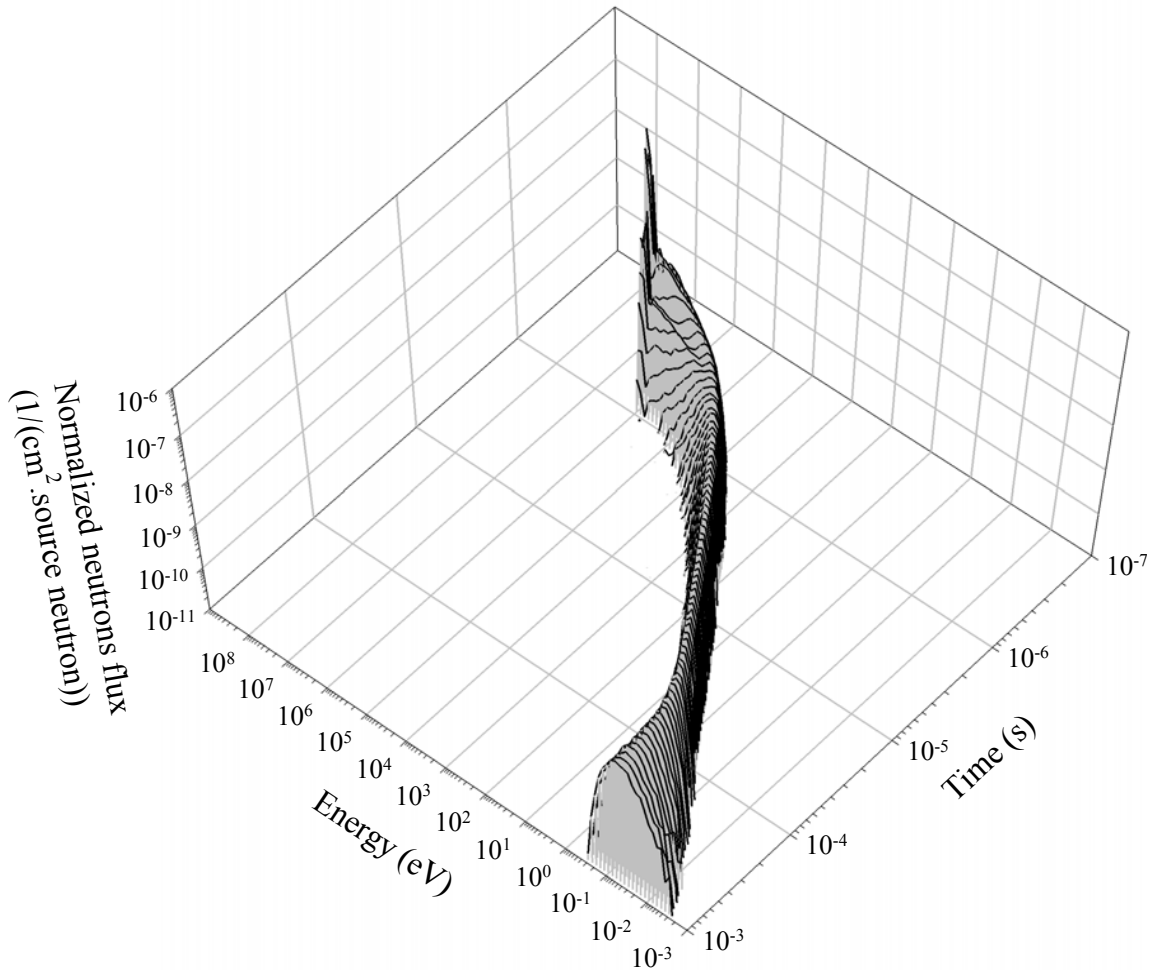

Figure 2-5. The time-energy behavior of neutrons slowing down in graphite. A focusing effect can be observed in the energy range between 10 keV and 1 eV.

In addition, peaks 2, 3, and 4 in Figure 2-4, which are observed at 8×10^{-6} s, 2×10^{-5} s and 1.3×10^{-4} s after the pulse, correspond to resonance groups and/or resonances in the Pu-239 fission cross-section at approximately 40 – 300 eV, 8 – 30 eV, and 0.3 eV respectively. On the other hand, Peak 5 in Figure 2-4 is found to also be a source peak. This can be explained by observing that the neutrons appearing at this point in time are shown by Figure 2-6 to have an average energy in the range of 1 - 2 meV, which is below the Bragg cutoff of graphite. In this case, source neutrons with such energy are expected to pass through the assembly uncollided but separated in time from peak 1 neutrons by the difference in their time of flight from the source to the detector. However this peak may not be easy to observe experimentally. Figure 2-6 also shows that after 10^{-3} s the average energy of the neutrons leaking from the assembly reaches a plateau at a value of approximately 0.05 eV. This can be shown to be the average energy of the neutrons in a Maxwellian flux ($\varphi(E)$) spectrum at room temperature, which implies that neutrons have reached thermal equilibrium.

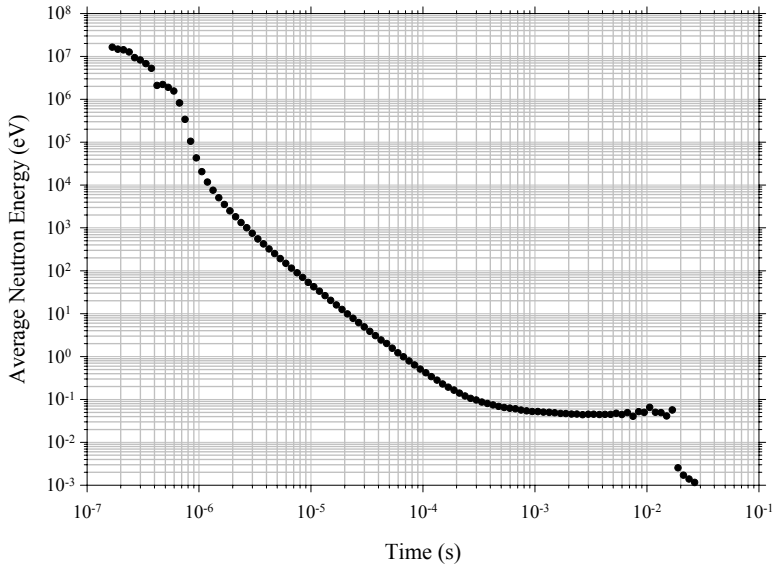

Figure 2-6. The relation between the time after the source pulse and the average energy of the neutron spectrum at the detector.

Finally, an observation that can be made by examining these results is that a Pu-239 fission detector is well suited for such experiments due to the shape of its fission cross section, which is expected to provide easy to observe time-energy calibration points in the measured time spectrum. Therefore, it was used to design and analyze this experiment.

2.4 MCNP5 perturbation simulations

2.4.1 Motivation

In order to benchmark the thermal neutron cross-section libraries, MCNP simulations of the experiment based on the cross-section libraries will be performed and compared to the measured data. To access the sensitivity of the experimental model to the cross-section libraries, a sensitivity analysis must be performed based on which the experimental setup could be optimized. To evaluate the sensitivity of a system to a certain data set (like a cross section data library), one can calculate the change of the system due to a change in the data set (i.e. a perturbation). The change of the system can be calculated directly by getting the difference between two calculations. One calculation is with the original data set and the other is with the perturbed data set. However in the Monte Carlo method, this direct method can be cumbersome. As a result, the differential operator perturbation method was introduced, which is to calculate the change of a system for a perturbed data set by calculating its Taylor series expansion coefficient. This method was developed by Hall in 1981, and is widely used in Monte Carlo method to perform sensitivity analysis in terms of the cross section library [33]. In 1984 McKinney implemented this method into a local MCNP code [34]. Later on, it became a standard feature in the MCNP code beginning with version 4b.

Unfortunately, the perturbation feature in the latest MCNP code is only compatible with the track length estimator (Tally 4), but not DXTRAN, point detector (Tally 5) and pulse height tallies. The point detector tally is heavily applied in the ORELA Slowing-Down-Time experiment simulation because the point detector tally can shorten the simulation time dramatically compared to the track length tallies.

In 1995, Hall's differential operator method was extended by Perel to point-detector-type problems, and a local MCNP code was also developed [35]. However, Perel's code only calculates the first order Taylor series coefficient but not the second order. In addition, by introducing this approach to MCNP5, several of its features can be used such as ability to specify an energy range or a type of reaction.

In this work, the perturbation of the graphite total and inelastic scattering cross section need to be calculated within different thermal neutron energy ranges. Nonetheless, the perturbation of the inelastic or elastic scattering cross section in the $S(\alpha, \beta)$ library is not provided by the latest MCNP code.

Therefore the purposes of this work is to derive the first and second order differential operators for the point detector that is consistent with the latest MCNP5 version, implement them into the MCNP5 code and modify the code to support the perturbed inelastic scattering cross section only in the $S(\alpha, \beta)$ library. After that, the modified MCNP5 code will be utilized to study the sensitivity of the simulation to the graphite thermal neutron library.

2.4.2 MCNP5 perturbation card

The MCNP5 perturbation card allows the introduction of a perturbation in the material density, composition or a certain type of reaction cross-section data. By using the differential operator method mentioned above, the perturbation estimates are made without changing the input material specification. When perturbation cards are used with track length tally, the entire tally output will be repeated for each perturbation card, in which the estimated differential changes in the tally are given, or the changes will be added to the unperturbed tally as required. When perturbation cards are used with point detector tally, the MCNP5 code will not calculate the perturbation. The entire tally output will also be repeated but set equal to zero.

A typical perturbation card is shown below:

pert1:n cell=1 rho=-1.7325 erg 1e-11 4.46e-6 rxn=1

The number "1" in "pert1:n" is the index of the perturbation card, there can be more than one perturbation card in the same input file. The "n" in the "pert1:n" means that the particle type is neutron. The perturbed cell is the number one cell when "cell=1". The perturbed material density is given by "rho=-1.7325". A negative entry indicates the units are g/cm^3. If the original density is 1.65 g/cm3, this gives a +5% perturbation on the material density, i.e. the neutron cross-section. That is because MCNP5 code uses the macroscopic cross-section Σ in the code, which is the multiplication of the density N and the microscopic cross-section σ. The perturbation on the material density and the microscopic cross-section will be equivalent. The perturbed neutron energy region is given by "erg 1e-11 4.46e-6". The option "rxn=1"indicates that the type of reaction, which will be perturbed, is the total cross-section

In order to modify the MCNP5 code to provide the perturbation calculation for the point detector tally, the input and output of the code can be left untouched. The method to calculate the differential changes will be developed and implemented into the MCNP5 code. The calculated differential changes, instead of zeros, will be sent to the output deck.

2.4.3 Derivation of the differential operator method for the point detector

Assuming C is a Monte Carlo response, a change in C due to changes in a related data set ν (e.g. a set of cross section) can be derived by its Taylor series expansion [32]:

$$\Delta C = \frac{dC}{d\nu}\Delta\nu + \frac{1}{2!}\frac{d^2C}{d\nu^2}\Delta^2\nu + \cdots + \frac{1}{n!}\frac{d^nC}{d\nu^n}\Delta^n\nu + \cdots \tag{2.19}$$

Define u_n as the n^{th} order coefficient,

$$u_n = \frac{1}{n!}\frac{d^nC}{d\nu^n} \tag{2.20}$$

For the data set $x_b(h)$, $b \in B, h \in H$, where B represents a set of macroscopic cross section and H represents a set of energies, u_n can be written as,

$$u_n = \frac{1}{n!}\sum_{b\in B}\sum_{h\in H} x_b^n(h)\left(\frac{\partial^n C}{\partial\, x_b^n(h)}\right) \tag{2.21}$$

The point detector (next event estimator) response C can be written as,

$$< C >= \frac{1}{N}\sum_i C_i = \frac{1}{N}\sum_i \bar{r}_i P_i \tag{2.22}$$

Where, N is the number of history, $\bar{r}_i$ is the detector response of the i^{th} history and P_i is its probability. Since the contributions to the point detector are made at the source or collision events throughout the random walk in each history, one can write,

$$C_i = \sum_{j=1}^{J_i} C_{ij} = \sum_{j=0}^{J_i} \bar{r}_{ij} \prod_{k=0}^{j-1} P_{ik} \tag{2.23}$$

$$< C >= \frac{1}{N}\sum_{i} C_i = \frac{1}{N}\sum_{i}\left[\sum_{j=0}^{J_i}\left(\bar{r}_{ij}\prod_{k=0}^{j-1} P_{ik}\right)\right] \tag{2.24}$$

Where, $\bar{r}_{ij}$ is the contribution to the detector tally at the j^{th} collision (or at the source if j=0) in the i^{th} history and P_{ik} is the probability that the particle has the k^{th} collision (or from the source if k=0) and is scattered into a certain direction for a certain distance until next collision or leakage in the i^{th} history. $\bar{r}_{ij}$ can be written explicitly as [35]

$$\bar{r}_{ij}(E_d) = \frac{1}{\lambda_d^2} S_{x_{j-1}}(E_d \leftarrow E_{j-1}, \Omega_d \leftarrow \Omega_{j-1}) \cdot e^{-\sum_z \Sigma_{tot,z}(E_d)\cdot\lambda_{d,z}} \tag{2.25}$$

Where λ_d is equal to the distance from the collision location to the point detector.

$S_{x_{j-1}}(E_d \leftarrow E_{j-1}, \Omega_d \leftarrow \Omega_{j-1})$ is equal to the probability for a neutron with energy E_{j-1} and direction Ω_{j-1} emerging into the detector. E_d is the energy of the neutron arriving at the detector and Ω_d is the direction from the collision to the detector. Note that the term of $e^{-\sum_z \Sigma_{tot,z}(E_d)\cdot\lambda_{d,z}}$ is the attenuation for the neutron which travels from the collision point to the detector. And the term of $\frac{1}{\lambda_d^2}$ is the solid angle that a unit area at the detector subtends at the collision point. P_{ik} can be written as [35]

$$P_{ik} = S_{x_{k-1}}(E_k \leftarrow E_{k-1}, \Omega_k \leftarrow \Omega_{k-1}) \cdot e^{-\sum_z \Sigma_{tot,z}(E_k)\cdot\lambda_{k,z}} \cdot \Sigma_{x_k}(E_k) dE_k d\Omega_k d\lambda_k \tag{2.26}$$

Where the term $S_{x_{k-1}}(E_k \leftarrow E_{k-1}, \Omega_k \leftarrow \Omega_{k-1}) dE_k d\Omega_k$ is the probability for a neutron scattered from the $(k-1)^{th}$ collision point (with energy E_{k-1} and direction Ω_{k-1}) into the k^{th} collision point (with energy in the interval dE_k about E_k and direction into the solid angle $d\Omega_k$ about Ω_k).

The term $e^{-\sum_z \Sigma_{tot,z}(E_k)\cdot\lambda_{k,z}}$ is the probability for a neutron which will not collide from the $(k-1)^{th}$

collision point to the kth collision point. And the term $\Sigma_{x_k}(E_k)d\lambda_k$ is the probability of the kth collision. Then one can get the nth order differential operator coefficient of the detector response C_i to the cross section data set $\Sigma_b(h)$ in the ith history,

$$u_{ni} = \frac{1}{n!}\sum_{b\in B}\sum_{h\in H}\Sigma_b^n(h)\left(\frac{\partial^n C_i}{\partial\Sigma_b^n(h)}\right) \tag{2.27}$$

And the expected value of u_n will be,

$$< u_n >= \frac{1}{N}\sum_{i}^{N} u_{ni} \tag{2.28}$$

2.4.3.1 First order

The expected value of the first order of differential operator coefficient $<u_1>$ can be calculated from equations (2.28) and (2.27) by setting n=1. From equation (2.27), the first order coefficient in the ith history u_{1i} can be written as

$$u_{1i} = \sum_{b\in B}\sum_{h\in H}\Sigma_b(h)\left(\frac{\partial C_i}{\partial\Sigma_b(h)}\right) \tag{2.29}$$

Substitute C_i from equation (2.13), we have

$$u_{1i} = \sum_{b\in B}\sum_{h\in H}\left[\Sigma_b(h)\frac{\partial}{\partial\Sigma_b(h)}\left(\sum_{j=1}^{J_i}\bar{r}_{ij}\prod_{k=0}^{j-1}P_{ik}\right)\right] \tag{2.30}$$

Rewrite equation (2.30)

$$u_{1i} = \sum_{j}^{J_i}\sum_{b\in B}\sum_{h\in H}\Sigma_b(h)\cdot\left[\frac{\partial}{\partial\Sigma_b(h)}\left(\bar{r}_{ij}\prod_{k=0}^{j-1}P_{ik}\right)\right] \tag{2.31}$$

Multiply the right hand side differential term by $\frac{1}{\bar{r}_{ij}\prod_{k=0}^{j-1}P_{ik}}\cdot\bar{r}_{ij}\prod_{k=0}^{j-1}P_{ik}$, we have

$$u_{1i} = \sum_{j}^{J_i} \sum_{b\in B} \sum_{h\in H} \Sigma_b(h) \cdot \left[\frac{\partial}{\partial \Sigma_b(h)} (\bar{r}_{ij} \prod_{k=0}^{j-1} P_{ik}) \right] \cdot \frac{1}{\bar{r}_{ij} \prod_{k=0}^{j-1} P_{ik}} \cdot \bar{r}_{ij} \prod_{k=0}^{j-1} P_{ik} \tag{2.32}$$

Notice that $\frac{df}{dx} \cdot \frac{1}{f} = \frac{d}{dx} \ln f$, then equation (2.32) becomes

$$u_{1i} = \sum_{j}^{J_i} \sum_{b\in B} \sum_{h\in H} \Sigma_b(h) \cdot \left[\frac{\partial}{\partial \Sigma_b(h)} \ln(\bar{r}_{ij} \prod_{k=0}^{j-1} P_{ik}) \right] \cdot \bar{r}_{ij} \prod_{k=0}^{j-1} P_{ik} \tag{2.33}$$

$$u_{1i} = \sum_{j}^{J_i} \sum_{b\in B} \sum_{h\in H} \Sigma_b(h) \cdot \left[\frac{\partial}{\partial \Sigma_b(h)} \left(\ln \bar{r}_{ij} + \sum_{k=0}^{j-1} \ln P_{ik} \right) \right] \cdot \bar{r}_{ij} \prod_{k=0}^{j-1} P_{ik} \tag{2.34}$$

From equation (2.25) one can get

$$\Sigma_b(h) \cdot \frac{\partial}{\partial \Sigma_b(h)} \ln \bar{r}_{ij} = -\delta(E_h - E_d) \cdot \sum_{z} \left[\Sigma_{b,z}(E_d) \cdot \lambda_{d,z} \right] \tag{2.35}$$

From equation (2.26) one can get

$$\Sigma_b(h) \cdot \frac{\partial}{\partial \Sigma_b(h)} (\ln P_{ik}) = \delta(E_h - E_d) \cdot \left[\delta_{b,x_k} - \sum_{z} \left(\Sigma_{b,z}(E_k) \cdot \lambda_{k,z} \right) \right] \tag{2.36}$$

Substitute equation (2.35) and (2.36) to equation (2.34),

$$u_{1i} = \sum_{j}^{J_i} \sum_{b\in B} \sum_{h\in H} \left\{ -\delta(E_h - E_d) \cdot \sum_{z} \left[\Sigma_{b,z}(E_h) \cdot \lambda_{d,z} \right] + \sum_{k}^{j-1} \delta(E_h - E_k) \cdot \left[\delta_{b,x_k} - \sum_{z} \left(\Sigma_{b,z}(E_h) \cdot \lambda_{k,z} \right) \right] \right\} \cdot \bar{r}_{ij} \prod_{k=0}^{j-1} P_{ik} \tag{2.37}$$

Rewrite equation (2.37),

$$u_{1i} = \sum_{j}^{J_i} \left\{ \left[-\sum_{z} \sum_{b\in B} \left(\Sigma_{b,z}(E_d) \cdot \lambda_{d,z} \right) + \sum_{k}^{j-1} \left(\sum_{b\in B} \delta_{b,x_k} - \sum_{z} \sum_{b\in B} \left(\Sigma_{b,z}(E_k) \cdot \lambda_{k,z} \right) \right) \right] \cdot \bar{r}_{ij} \prod_{k=0}^{j-1} P_{ik} \right\} \tag{2.38}$$

Define

$$a_1 = -\sum_{z} \sum_{b\in B} \left(\Sigma_{b,z}(E_d) \cdot \lambda_{d,z} \right) \tag{2.39}$$

$$a_2 = \sum_{k}^{j-1}\left(\sum_{b\in B}\delta_{b,x_k}\right) \tag{2.40}$$

$$a_3 = -\sum_{k}^{j-1}\left(\sum_{z}\sum_{b\in B}\left(\Sigma_{b,z}(E_k)\cdot\lambda_{k,z}\right)\right) \tag{2.41}$$

Figure 2-7 illustrates the physical meaning of the coefficients a_1, a_2 and a_3. As it can be seen, a_1 is the contribution of the attenuation from the collision point to the detector. When the cross-section of the interested material is increasing, the attenuation will be increasing and the contribution of one history will be decreasing. Therefore a_1 is a negative value as shown in equation (2.39). The contribution from the collision itself is represented by the parameter a_2. When the cross-section of the interested material is increasing, the probability of collision will be increasing. Therefore a_2 is a positive value as shown in equation (2.40). The contribution of the attenuation up to the collision point is given by a_3. Similar to a_1, a_3 is also a negative value as shown in equation (2.41).

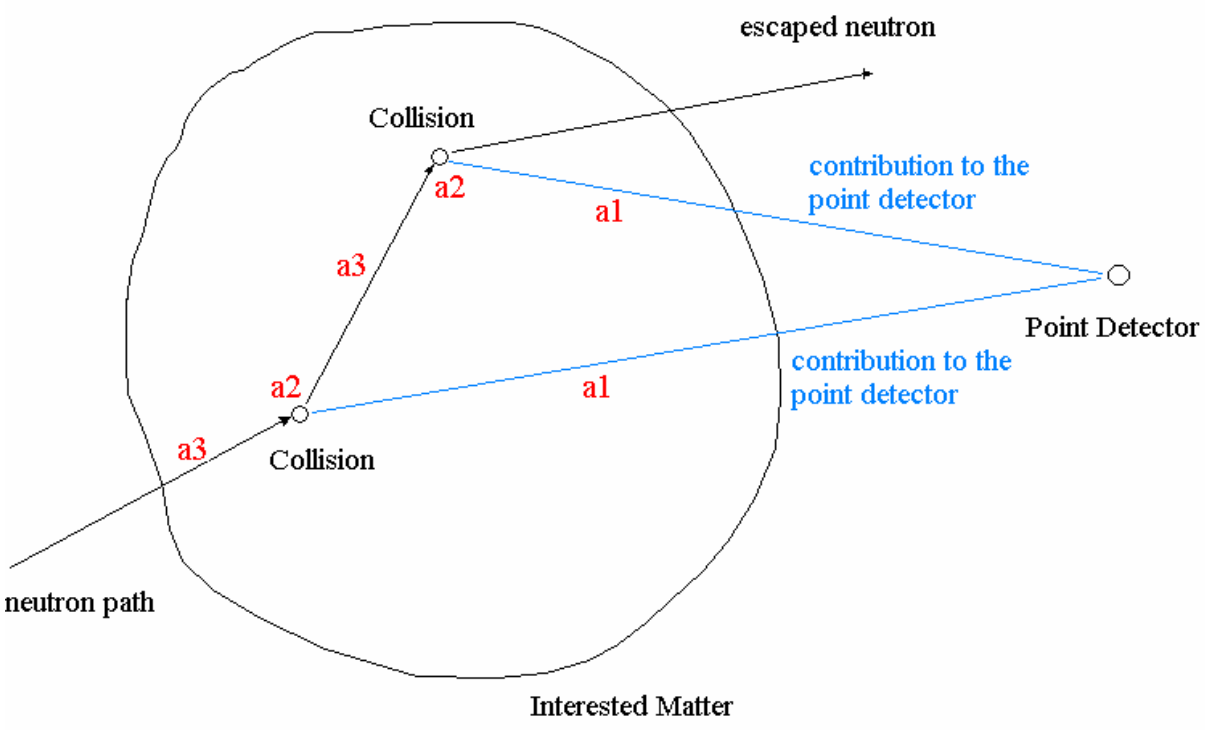

Figure 2-7. Perturbation coefficients.

In addition, one can get

$$C_{ij} = \bar{r}_{ij} \prod_{k=0}^{j-1} P_{ik} \tag{2.42}$$

Where C_{ij} is calculated by original MCNP5 code. Therefore the first order perturbation coefficient in the i^{th} history can be written as:

$$u_{1i} = \sum_{j}^{J_i} \left[(a_1 + a_2 + a_3) \cdot C_{ij} \right] \tag{2.43}$$

2.4.3.2 Second order

Similar to the first order coefficient, from equation (2.27), the second order coefficient in the i^{th} history u_{2i} can be written as

$$u_{2i} = \frac{1}{2} \sum_{b \in B} \sum_{h \in H} \Sigma_b^2(h) \left(\frac{\partial^2 C_i}{\partial \Sigma_b^2(h)} \right) \tag{2.44}$$

Substitute equation (2.23) to (2.44),

$$u_{2i} = \frac{1}{2} \sum_{b \in B} \sum_{h \in H} \Sigma_b^2(h) \cdot \frac{\partial^2}{\partial \Sigma_b^2(h)} \left(\sum_{j=1}^{J_i} \bar{r}_{ij} \prod_{k=0}^{j-1} P_{ik} \right) \tag{2.45}$$

$$u_{2i} = \frac{1}{2} \sum_{j=1}^{J_i} \sum_{b \in B} \sum_{h \in H} \Sigma_b^2(h) \cdot \frac{\partial}{\partial \Sigma_b(h)} \left[\frac{\partial}{\partial \Sigma_b(h)} \left(\bar{r}_{ij} \prod_{k=0}^{j-1} P_{ik} \right) \right] \tag{2.46}$$

From equation (2.34) and (2.37), one can get

$$\begin{aligned} &\Sigma_b(h) \cdot \frac{\partial}{\partial \Sigma_b(h)} \left(\bar{r}_{ij} \prod_{k=0}^{j-1} P_{ik} \right) = \\ &\left\{ -\delta(E_h - E_d) \cdot \sum_z \left[\Sigma_{b,z}(E_h) \cdot \lambda_{d,z} \right] + \sum_k^{j-1} \delta(E_h - E_k) \cdot \left[\delta_{b,x_k} - \sum_z \left(\Sigma_{b,z}(E_h) \cdot \lambda_{k,z} \right) \right] \right\} \cdot \bar{r}_{ij} \prod_{k=0}^{j-1} P_{ik} \end{aligned} \tag{2.47}$$

Define

$$T = -\delta(E_h - E_d)\cdot\sum_z\left[\Sigma_{b,z}(E_h)\cdot\lambda_{d,z}\right]+\sum_k^{j-1}\delta(E_h-E_k)\cdot\left[\delta_{b,x_k}-\sum_z\left(\Sigma_{b,z}(E_h)\cdot\lambda_{k,z}\right)\right] \quad (2.48)$$

Then one can get

$$\frac{\partial}{\partial\Sigma_{\mathrm{b}}(\mathrm{h})}\left(\bar{\mathrm{r}}_{\mathrm{ij}}\prod_{\mathrm{k}=0}^{\mathrm{j}-1}\mathrm{P}_{\mathrm{ik}}\right)=\frac{1}{\Sigma_{\mathrm{b}}(\mathrm{h})}\cdot\mathrm{T}\cdot\bar{\mathrm{r}}_{\mathrm{ij}}\prod_{\mathrm{k}=0}^{\mathrm{j}-1}\mathrm{P}_{\mathrm{ik}} \quad (2.49)$$

Substitute equation (2.49) into (2.46)

$$u_{2i}=\frac{1}{2}\sum_{j=1}^{J_i}\sum_{b\in B}\sum_{h\in H}\Sigma_b^2(h)\cdot\frac{\partial}{\partial\Sigma_b(h)}\left[\frac{T}{\Sigma_b(h)}\cdot\bar{r}_{ij}\prod_{k=0}^{j-1}P_{ik}\right] \quad (2.50)$$

$$u_{2i}=\frac{1}{2}\sum_{j=1}^{J_i}\sum_{b\in B}\sum_{h\in H}\Sigma_b^2(h)\cdot\left[\frac{\partial}{\partial\Sigma_b(h)}\left(\frac{T}{\Sigma_b(h)}\right)\cdot\bar{r}_{ij}\prod_{k=0}^{j-1}P_{ik}+\frac{T}{\Sigma_b(h)}\cdot\frac{\partial}{\partial\Sigma_b(h)}\left(\bar{r}_{ij}\prod_{k=0}^{j-1}P_{ik}\right)\right] \quad (2.51)$$

Substitute equation (2.48) and (2.49) into (2.51),

$$u_{2i}=\frac{1}{2}\sum_{j=1}^{J_i}\sum_{b\in B}\sum_{h\in H}\Sigma_b^2(h)\cdot\left[-\frac{\sum_{k=0}^{j-1}\delta(E_h-E_d)\delta_{b,x_k}}{\Sigma_b^2(h)}\cdot\bar{r}_{ij}\prod_{k=0}^{j-1}P_{ik}+\frac{T^2}{\Sigma_b^2(h)}\cdot\left(\bar{r}_{ij}\prod_{k=0}^{j-1}P_{ik}\right)\right] \quad (2.52)$$

$$u_{2i}=\frac{1}{2}\sum_{j=1}^{J_i}\left\{\left[-\sum_{k=0}^{j-1}\left(\sum_{h\in H}\delta(E_h-E_d)\cdot\sum_{b\in B}\delta_{b,x_k}\right)+\sum_{b\in B}\sum_{h\in H}T^2\right]\cdot C_{ij}\right\} \quad (2.53)$$

Where

$$\sum_{b\in B}\sum_{h\in H}T^2=\sum_{b\in B}\sum_{h\in H}\left\{-\delta(E_h-E_d)\cdot\sum_z\left[\Sigma_{b,z}(E_h)\cdot\lambda_{d,z}\right]+\sum_k^{j-1}\delta(E_h-E_k)\cdot\left[\delta_{b,x_k}-\sum_z\left(\Sigma_{b,z}(E_h)\cdot\lambda_{k,z}\right)\right]\right\}^2 \quad (2.54)$$

Rewrite equation (2.54)

$$\sum_{b\in B}\sum_{h\in H}T^2=\sum_{b\in B}\left\{-\sum_z\left[\Sigma_{b,z}(E_d)\cdot\lambda_{d,z}\right]+\sum_k^{j-1}\left[\delta_{b,x_k}-\sum_z\left(\Sigma_{b,z}(E_k)\cdot\lambda_{k,z}\right)\right]\right\}^2 \quad (2.55)$$

Since in the MCNP input file, each perturbation card can only specify one type of cross section, the parameter b in equation (2.55) is fixed and the summation for b can be omitted.

$$\sum_{b\in B}\sum_{h\in H}T^2=\left\{-\sum_z\left[\Sigma_{b,z}(E_d)\cdot\lambda_{d,z}\right]+\sum_k^{j-1}\left[\delta_{b,x_k}-\sum_z\left(\Sigma_{b,z}(E_k)\cdot\lambda_{k,z}\right)\right]\right\}^2 \tag{2.56}$$

Substitute equation (2.39), (2.40) and (2.41) into equation (2.56), one can get

$$\sum_{b\in B}\sum_{h\in H}T^2=\left(a_1+a_2+a_3\right)^2 \tag{2.57}$$

Substitute equation (2.57) into equation (2.53)

$$u_{2i}=\frac{1}{2}\sum_{j=1}^{J_i}\left\{\left[-\sum_{k=0}^{j-1}\left(\sum_{h\in H}\delta(E_h-E_d)\cdot\sum_{b\in B}\delta_{b,x_k}\right)+\left(a_1+a_2+a_3\right)^2\right]\cdot C_{ij}\right\} \tag{2.58}$$

In this way, the second order perturbation coefficient can be calculated.

2.4.4 Implementation

Figure 2-8 illustrates the simplified flow chart and the corresponding major subroutines of the MCNP5 code. Execution of the MCNP5 code proceeds in the following way; at the beginning the subroutine IMCN will be called to read the user input file and initiate all the arrays, secondly the subroutine PLOT will be called to plot the geometry if necessary, and then the cross section of all the involving materials will be input into the cross section arrays, finally the particle transport code will be called for every particle history and print output until the maximum history number is reached. For more details, refer to the MCNP5 manual Volume III[32].

When one uses the perturbation card with the track length tally, the code will initiate the input file, read the parameters from the perturbation card, calculate the perturbation and dump them into the output file. While when one uses the perturbation card with the point detector tally, the original MCNP5 code will still read the input. However, instead of calculating the perturbation, the code will do nothing and dump all zeroes into the output file. Therefore, the input and output part can

be left untouched. The majority of the work done by the program will be to calculate the perturbation coefficients and accumulate them at the end.

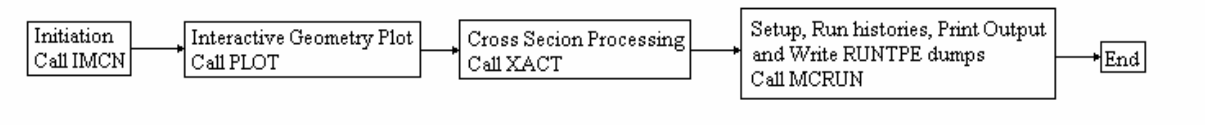

Figure 2-8. Simplified flow chart of the MCNP code.

The subroutine HSTORY is the heart of the MCNP code dealing with particle transport, which is called in the subroutine TRNSPT (called by MCRUN). It is the place where the perturbation coefficients are calculated. The flow chart of the subroutine HSTORY after the modification is shown in Figure 2-9. As it can be seen, there are two new subroutines, PERTPC1 and PERTPC3, which calculate the coefficients a1, a2 and a3 in equation (2.43). Whenever a particle starts from the source or a collision happens, the subroutine TALLYD will be called to calculate the contribution to the detector from the source or the collision event. Consequently the subroutine PERTPC3 will be called by the TALLYD to calculate the perturbation due to the collision (the coefficient a2) and the perturbation due to the attenuation from the source or collision point to the detector (the coefficients a3). Whenever a particle travels through a region of interest, the subroutine PERTPC1 will be called to calculate the perturbation due to the attenuation of this region (the coefficient a1). After each history, the first and second order perturbation tally will be calculated and accumulated based on the coefficients a1, a2 and a3 as well as the original tally. At the end, the result will be written into the output file. In addition, when one perturbs the inelastic or elastic cross-section only in the $S(\alpha, \beta)$, the modified MCNP code will read the proper cross-section value from the $S(\alpha, \beta)$ library and calculate the perturbation.

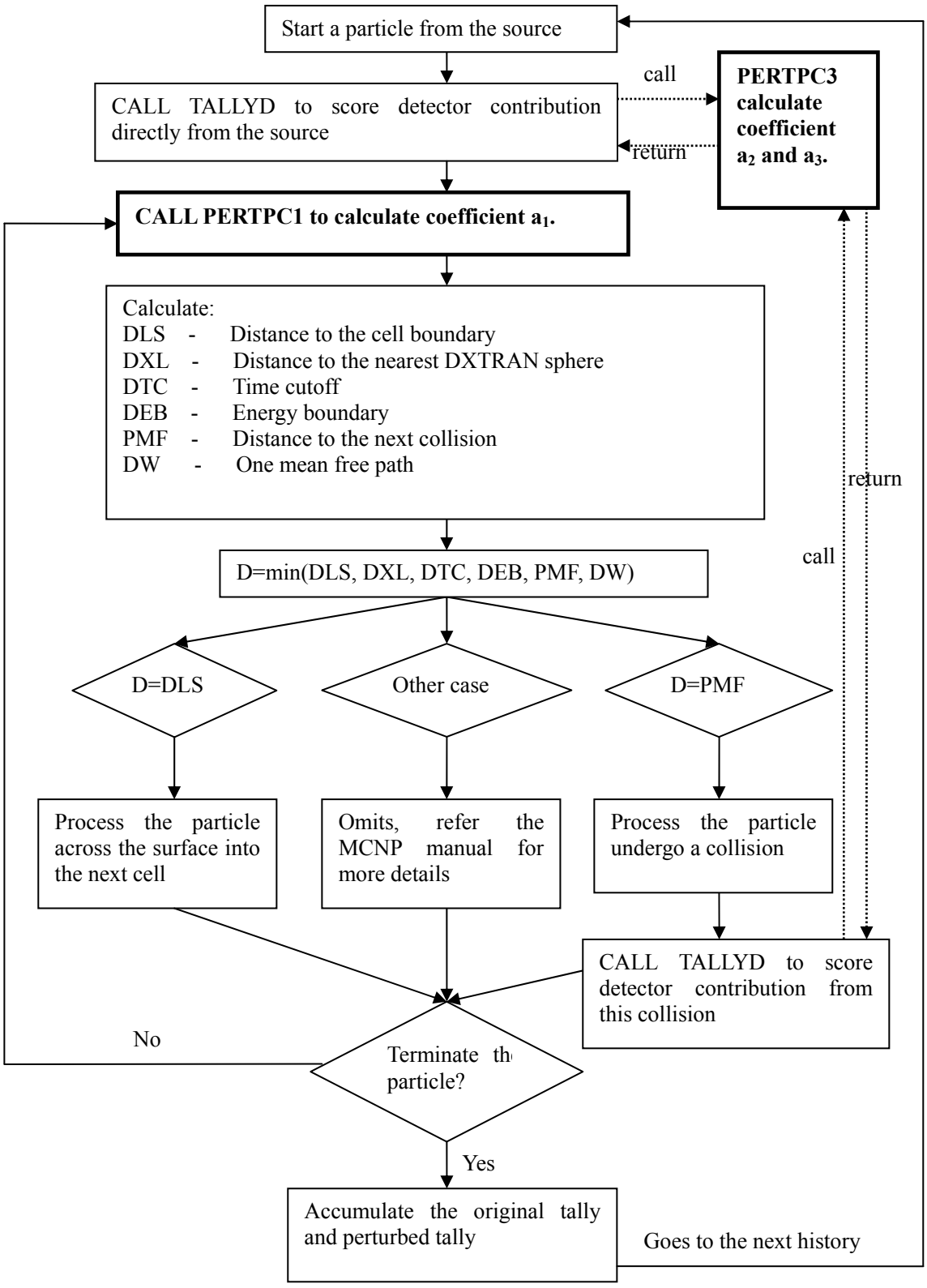

Figure 2-9. Modified flow chart of the subroutine HSTORY.

2.4.5 Testing the modified MCNP5 code

After the theory discussed above was implemented into the MCNP5 1.30 source code (latest version at that time), the ability of MCNP5 is extended to calculate the perturbation for the next event detector (point detector tally 5) as well as the track length detector. At the same time all the features for the track length estimator perturbation remains and works well with the point detector perturbation as well.

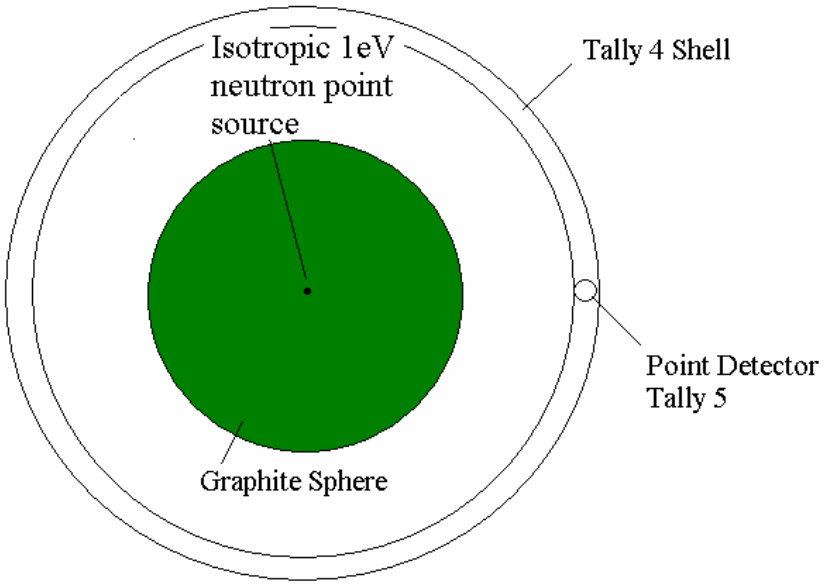

Figure 2-10. Sketch of the testing model.

A MCNP model was designed to test the modified perturbation code. The perturbation for the point detector is calculated and compared to the track length detector perturbation result. Additionally the perturbation is also calculated directly by performing two separated runs, one with original data and one with perturbed data. Figure 2-10 illustrates the sketch of the model. A monoenergetic isotropic (1eV) point neutron source is placed at the center of a graphite sphere. A thin shell encloses the graphite sphere. The neutron flux will be tallied in this shell by using F4

tally. Due to the symmetry, the neutron flux at each point in the shell is approximately equivalent. Therefore the F4 cell tally of the whole shell will be equivalent to a point detector in the shell. Furthermore, almost all neutrons will contribute to the F4 cell tally (ignore the absorbed neutrons) due to the geometry. As a result, the F4 cell tally will gain enough statistics to be compatible to the point detector tally and the testing run can be finished within a reasonably short time.

As it can be seen in Figure 2-11, the neutron energy spectra calculated by the modified MCNP5 code of the F4 cell tally and the F5 point detector tally are consistent. Consequently the two tallies are equivalent regardless of different geometries and the perturbations of the two tallies should be equivalent also. After perturbing the graphite total cross-section by 3%, the perturbations of the two tallies are calculated by the modified MCNP5 code and are consistent as seen in Figure 2-12. Since the perturbation of the F4 cell tally is a standard feature in the MCNP5 code and has been tested, one can claim that the point detector perturbation calculated by the modified MCNP5 code is reasonable. Furthermore, two calculations are performed directly with the original graphite total cross-section and the perturbed cross-section (multiplied by 103%). The differential neutron energy spectrum between the two calculations is compared to the F5 point detector tally calculated by the modified MCNP5 code shown in Figure 2-13. Since the two direct calculations have the same number of histories as the F5 perturbation calculation, the difference between them has larger statistical errors (shown in Figure 2-13). After increasing number of histories by 10 times, the statistical errors are reduced and the differential neutron spectrum of the two direct calculations agrees with the F5 perturbation calculation shown in Figure 2-14. As a result, the modification of the MCNP5 code is successful and the calculation results are reasonable.

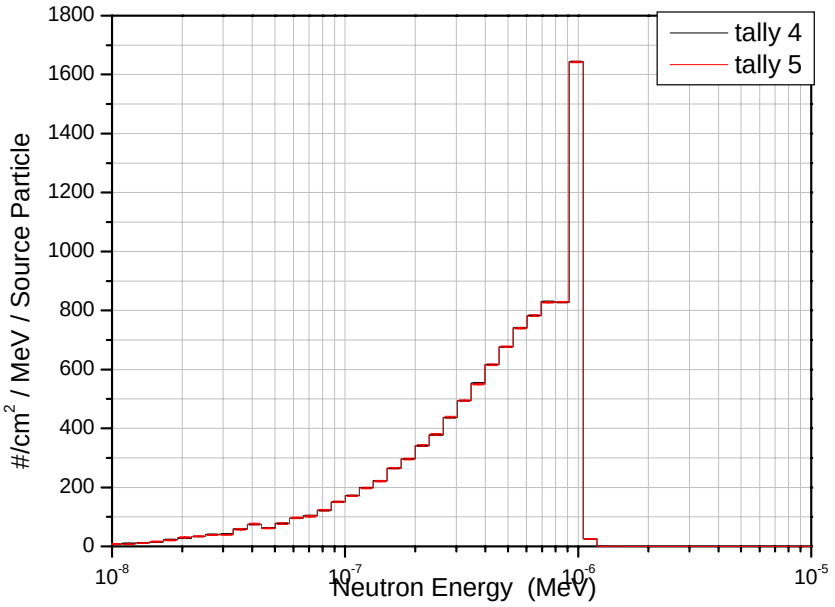

Figure 2-11. Energy spectra of Tally 4 and Tally 5.

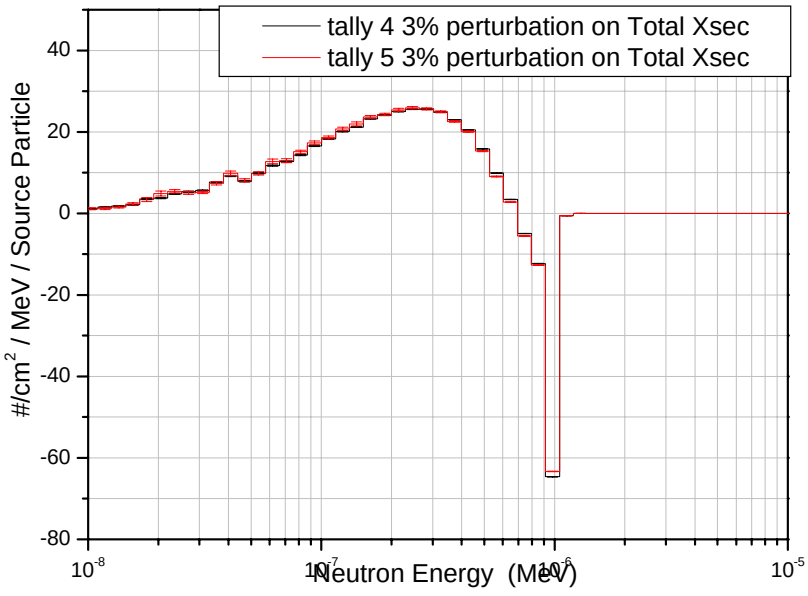

Figure 2-12. Perturbation calculations of Tally 4 and Tally 5.

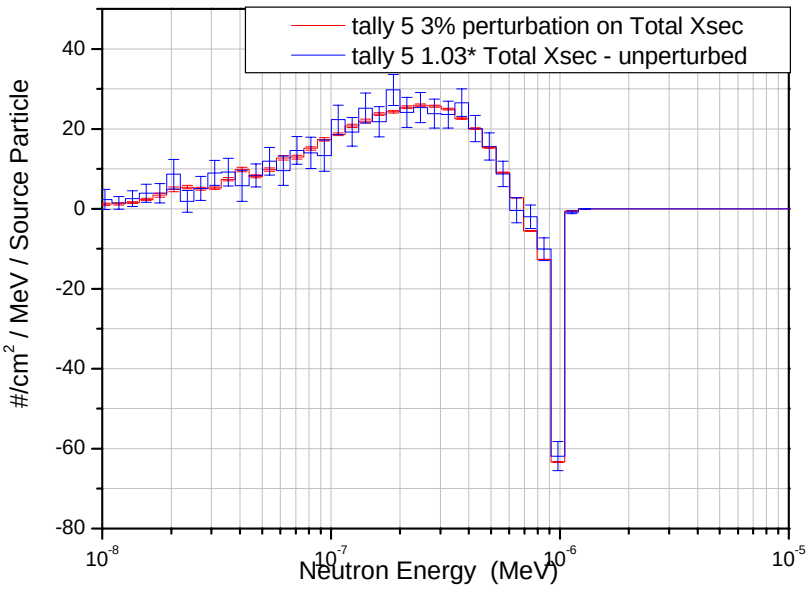

Figure 2-13. Perturbation calculations of Tally 5 and direct method.

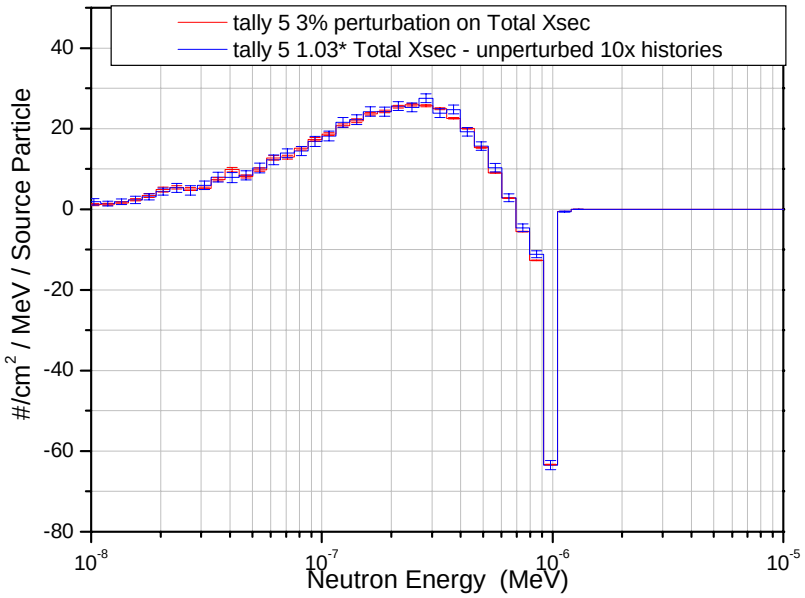

Figure 2-14. Perturbation calculations of Tally 5 and direct method with 10 times histories.

2.5 Experiment design

2.5.1 Size of the graphite assembly

The size of the graphite assembly is a key parameter in this experiment. Designing the assembly appropriately can facilitate the experiment, while ensuring that statistically valid measurements are performed within acceptable measurement time. Moreover, at the high temperature the heating system will be introduced and its dimensions will depend on the size of the graphite assembly.

Using the model discussed previously, the time spectra for neutrons leaking from 50x50x50 cm, 70x70x70 cm, and 1x1x1 m graphite assemblies at room temperature were calculated and shown in Figure 2-15. Notice that all the time spectra are almost identical in shape but differ in the intensity of the signal before $1x10^{-4}$s. Furthermore, it can be seen that in the time period less than 10^{-4} s the 50x50x50 cm assembly results in a higher response. However, in the important time period after 10^{-4} s (i.e., the time after which the neutrons have been thermalized according to Figure 2-6), the 70x70x70 cm get close to the 50 cm model and give the higher response after $4x10^{-4}$s. And in the time period after $2x10^{-3}$, the 1x1x1 m assemblies give the higher response. This can be explained by the fact that neutrons are escaping from the 50x50x50 cm assembly before reaching thermal energies, while the neutrons in the 1x1x1 m assembly have more collisions so that more neutrons will reach thermal equilibrium.

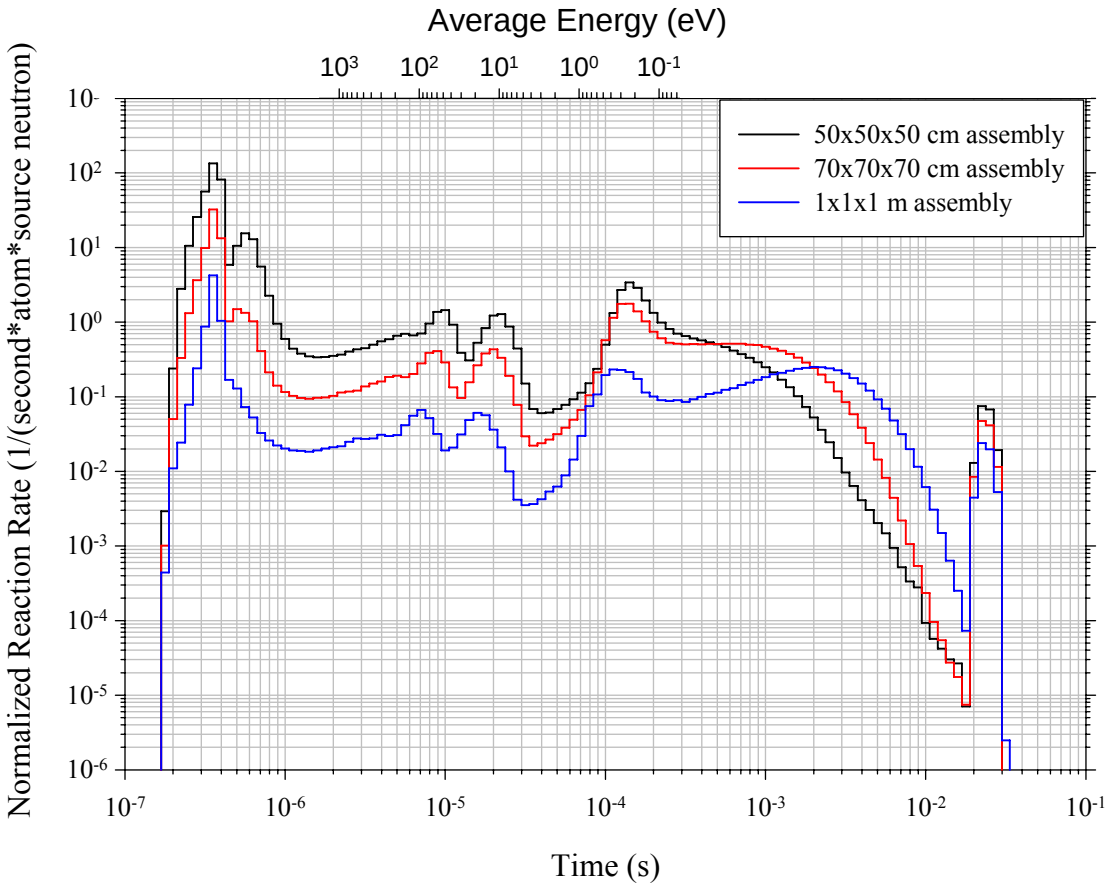

Figure 2-15. The calculated time dependent reaction rates for a Pu-239 detector using 50x50x50 cm, 70x70x70 cm and 1x1x1 m graphite assemblies.

By using the modified MCNP5 code mentioned in the previous section, the graphite neutron total cross-section were perturbed by +3% in the thermal energy region (4.45eV to 10^{-5}eV). The percentage differences on the time spectra due to the perturbed cross-section were calculated and shown in Figure 2-16 for the three graphite assemblies with different size. As it can be seen in Figure 2-16, the same perturbation on the graphite total thermal neutron cross-section had the largest effect on the 1x1x1 m assembly and smallest effect on the 50x50x50 cm assembly. That can be explained by the fact that one neutron on average will have larger number of collisions in a larger assembly.

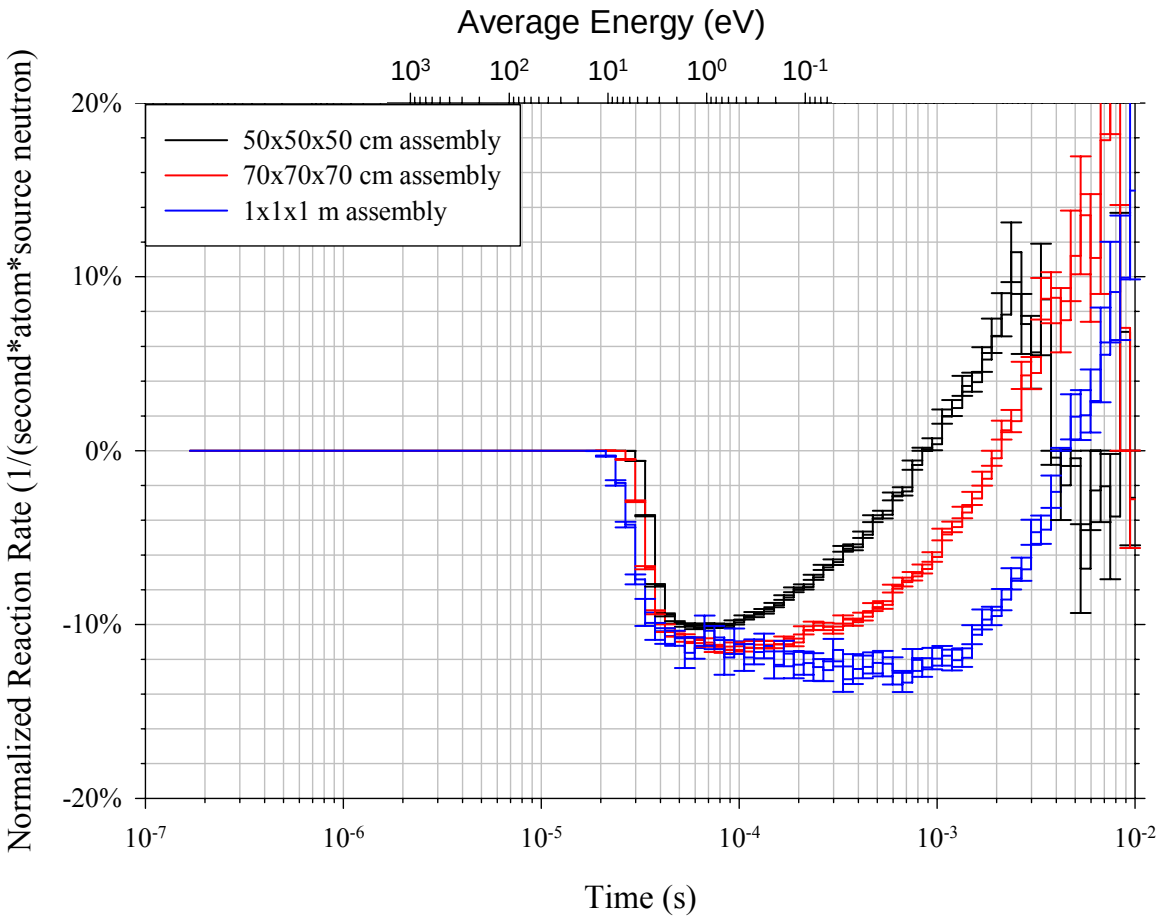

Figure 2-16. Perturbation on the time spectra of the three different size graphite assemblies after increasing the total neutron cross-section by 3% in the thermal energy region.

The ORELA accelerator will mostly work at the frequency 525 pulses/sec, and sometimes at a frequency 130 pulses/sec. The corresponding cutoff time will be around 1.9×10^{-3} second and 7.7×10^{-3} second respectively. Before the cutoff time 1.9×10^{-3} second, the 1x1x1 m assembly gave the lowest counting rate as well as the largest volume and mass. Therefore, despite the fact that the model with larger assembly is more sensitive to the graphite thermal neutron cross-section, the 1x1x1 m assembly should be eliminated. In the time period corresponding to thermal energies (after 10^{-4} s), the 50x50x50 cm assembly does not have a big advantage over 70x70x70 cm assembly before 4×10^{-4}s, while after 4×10^{-4}s it has much less response. In addition, the model

with 70x70x70 cm assembly is more sensitive to the graphite thermal neutron cross-section. Therefore, at this stage it is concluded that the 70x70x70 cm assembly would be the most appropriate one, for which the heating system should be designed and made. However, at room temperature the heating system will be removed and the measurements with these three size graphite assemblies are still feasible.

2.5.2 Heating system design

As stated earlier, the objective of this experiment is to study neutron thermalization in reactor grade graphite as a function of temperature. Therefore, a heating system was required to allow uniform heating of the graphite assembly for temperatures beginning with room temperature and reaching approximately 1200 K. The heating system was designed for the 70x70x70 cm graphite assembly. It consists of a furnace, a gas regulation system and a temperature monitoring system.

2.5.2.1 Furnace

The AutoCad model of the furnace is shown in Figure 2-17 and 2-18. The basic function of the furnace is to uniformly heat the graphite assembly up to 1200K and hold the temperature as constant as possible for periods reaching up to 24 hours. Depending on which detector is used (detector selection will be discussed later), the measurement time varies from 1 hour to 24 hours. To ensure that the graphite does not catch fire at high temperature, the furnace has to be sealed and filled with Nitrogen gas at a small over pressure.

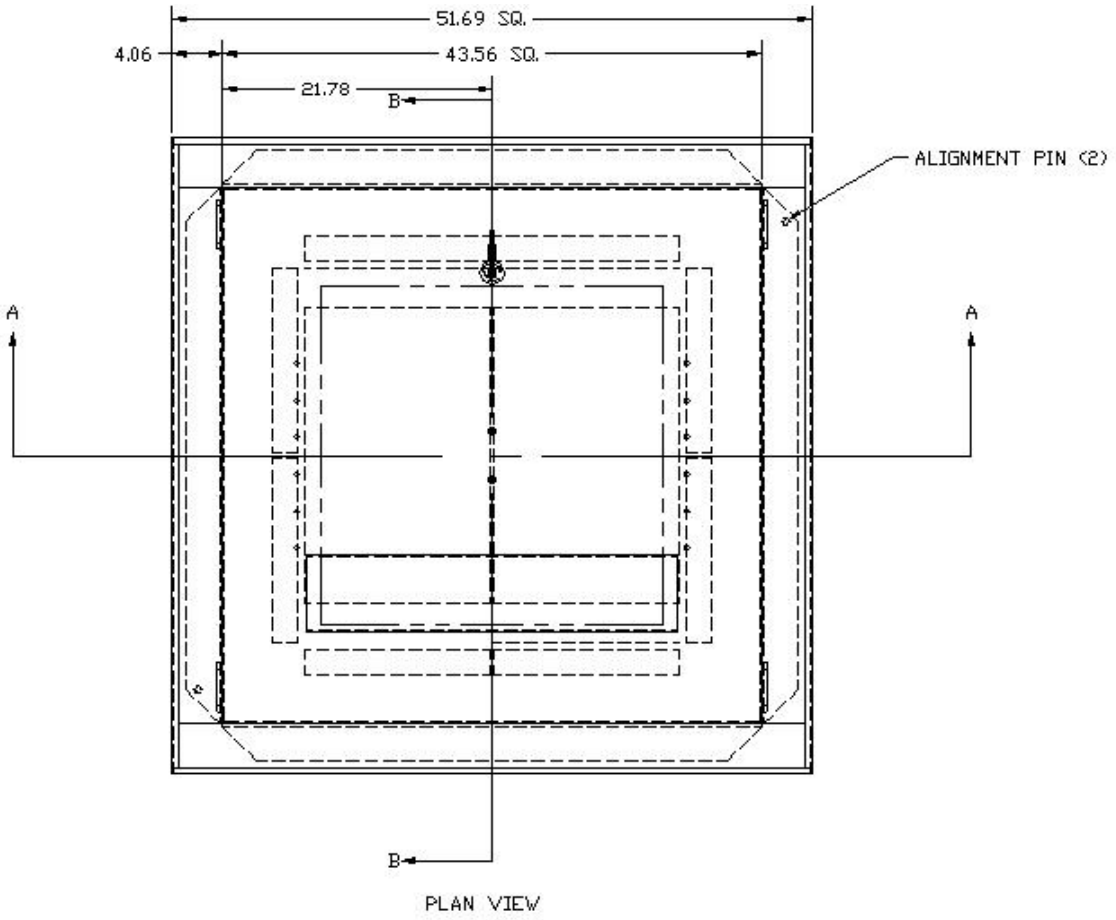

Figure 2-17. The top view of the Furnace.

At room temperature, it's possible to make the measurement without the furnace to reduce neutron attenuation. Therefore the furnace was made into two separable parts: the furnace bell and the furnace table. The furnace table sits on the ground to provide support for the graphite assembly and the furnace bell, it also has the ability to adjust the height to keep the center of the graphite assemblies with different sizes aligned with the neutron beam. The furnace table contains the bottom heater and insulation, while the furnace bell contains the heater and insulation for the other five surfaces. Because the furnace bell will face the neutron beams, construction materials that have a low density and neutron cross section are preferred.

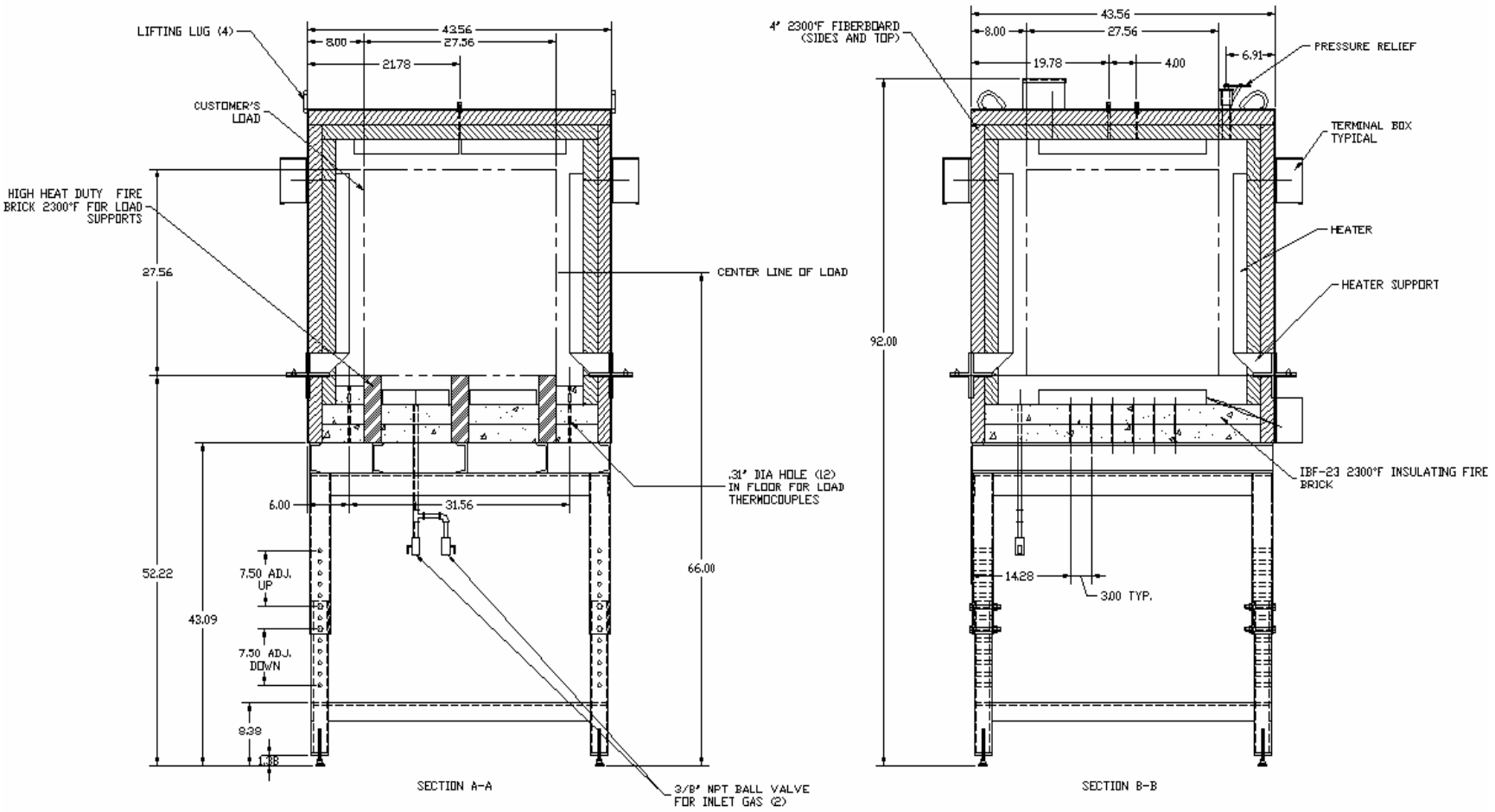

Figure 2-18. Section A-A and B-B view of the furnace.

The configuration illustrated in Figure 2-18 was converted into an MCNP model to perform simulations that study the effect of the heating system on the signal of interest (i.e., the time spectrum), shown in Figure 2-19. In this case, the Pu-239 detector was placed 25 cm away from the surface of the heating box (i.e., 46cm away from the surface of the 70x70x70cm graphite assembly). This distance is chosen to ensure that the temperature of the heating assembly does not affect the detector. The insulation contained in the heating system is composed of low-density (~ 0.5 g/cm^3) silicides and/or aluminides with trace amounts of hydrogen. The heater plates and support bricks are made of the same material as the insulator but have a higher density (~ 1.6 g/cm^3). An important parameter of the design was the void space between the graphite assembly and the boundaries of the heating system. The size of the void separation (5 cm) was tuned to ensure a minimal effect on the measured signal.

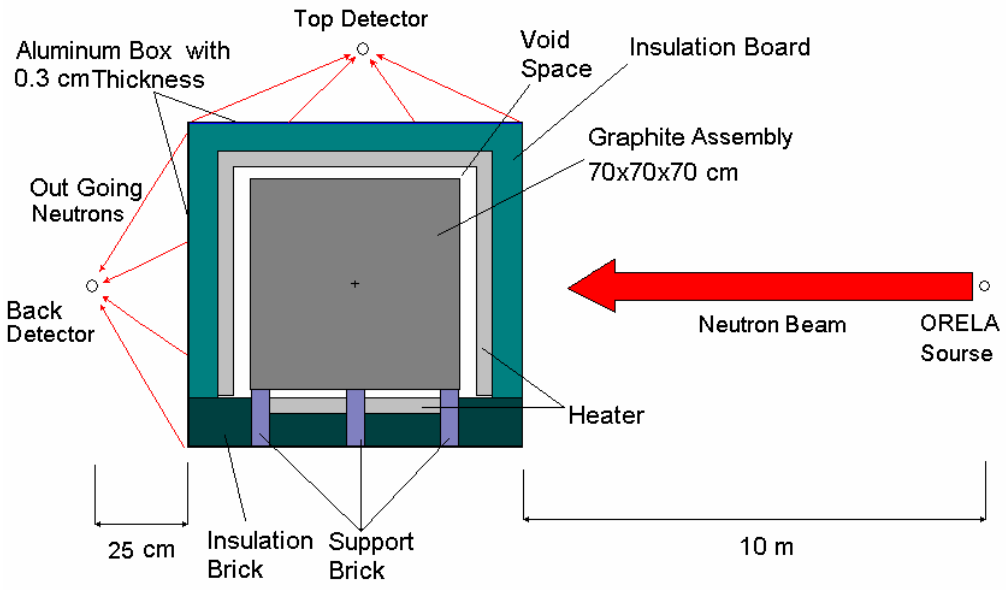

Figure 2-19. A schematic of the MCNP model of the experiment including the furnace.

In Figures 2-20 and 2-21, the comparisons between the time spectrum with and without the furnace

are shown for the back Pu-239 detector and the top Pu-239 detector. As it can be seen, despite the alteration introduced by the furnace (including an attenuation in the signal within the thermal neutron region), the measured time spectrum contains all the important features that are characteristic of the unperturbed spectrum.

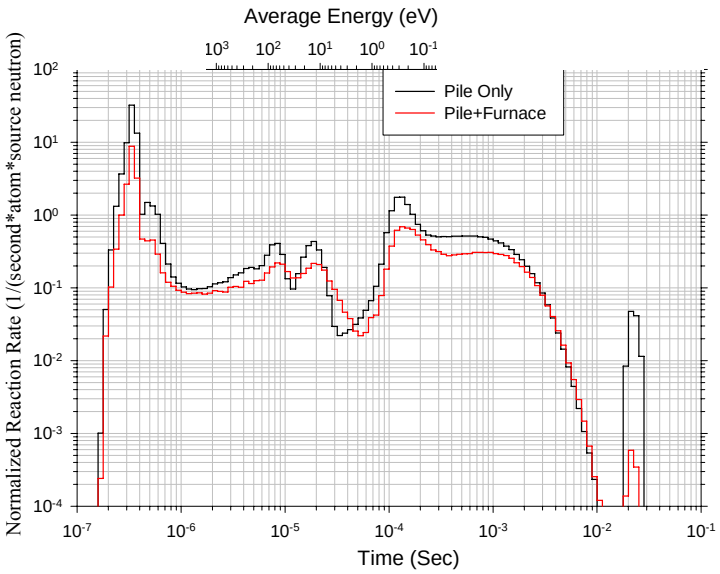

Figure 2-20. Back detector comparison of the time spectra of a Pu-239 detector with and without the furnace.

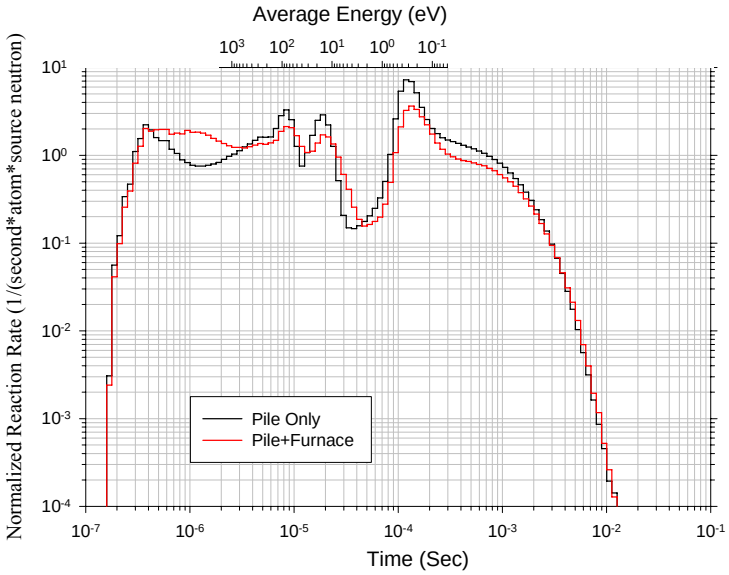

Figure 2-21. Top detector comparison of the time spectrum of a Pu-239 detector with and without the furnace.

Figure 2-22 and 2-23 show the perturbation effect on the time spectra due to the +3% increasing on the graphite total neutron cross-section in the thermal energy region for the back and top detectors. As it can be seen, introducing the furnace will make the time spectrum little less sensitive to the neutron total cross-section. However the model with furnace still can give as large as 10% difference on the time spectrum for the 3% increase in total thermal neutron cross-section.

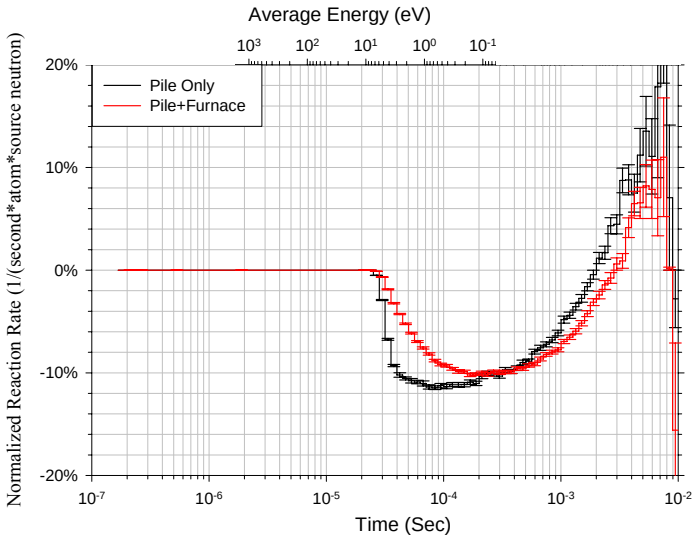

Figure 2-22. The perturbation calculation on the time spectra due to the +3% increase in the graphite total thermal neutron cross-section for the back detector at room temperature.

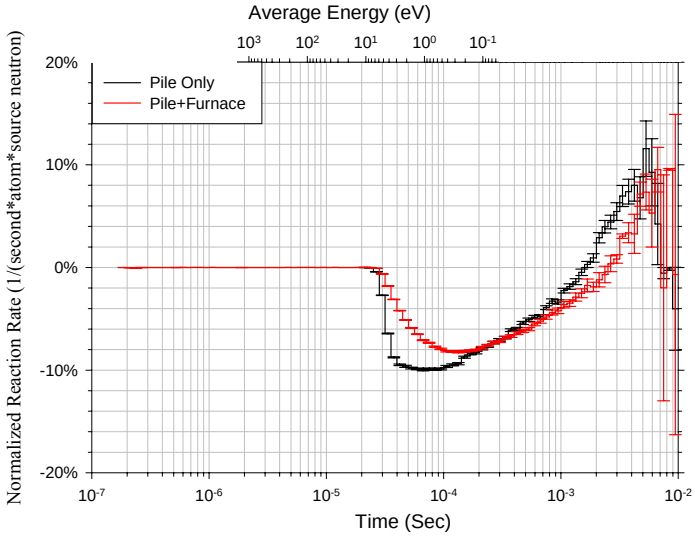

Figure 2-23. The perturbation calculation on the time spectra due to the +3% increase in the graphite total thermal neutron cross-section for the top detector at room temperature.

2.5.2.2 Gas regulation system and temperature monitor system

For the high temperature measurements, the furnace will be loaded and the graphite assembly will be heated. There are 10 thermocouples distributed inside the graphite assembly to monitor the temperature, as shown in Figure 2-24. And there are two more thermocouples, one is on the top of the furnace to monitor the temperature outside the furnace, the other is under the furnace table to monitor the temperature of the polyethylene slab (part of the shielding system, will be discussed later), for which the melting point is about 90^{o}C.

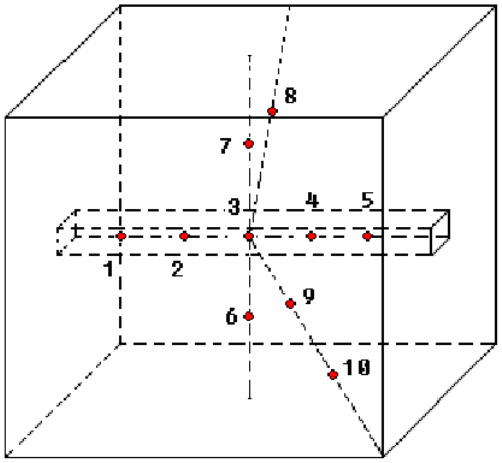

Figure 2-24. Thermocouples distribution in the 70x70x70 cm graphite assembly.

Those 12 thermocouples connect to the temperature monitor, MV100, which is made by YOKOGAWA [36]. The MV100 can record the temperatures of 12 channels and work as a web server with an Ethernet port equipped to instantly send the temperature data to the computer in the data acquisition room. Beside the web server, the MV100 also can provide the temperature inputs to the LabView [37] code and trigger the emergency cooling when the temperature of the graphite assembly goes to dangerous levels.

To reduce the probability of graphite to combust, nitrogen cover gas is introduced into the furnace to purge the oxygen and keep an over pressure in the furnace. The nitrogen gas can also work as a coolant when the system is over heated. To fulfill those functions, four gas cylinders, are used. The first will be to provide the nitrogen supply, the second will serve as a nitrogen backup, the third will provide the nitrogen coolant and the fourth will be an emergency coolant cylinder. The gas flow will be regulated by 8 valves installed in the furnace as shown in Figure 2-25.

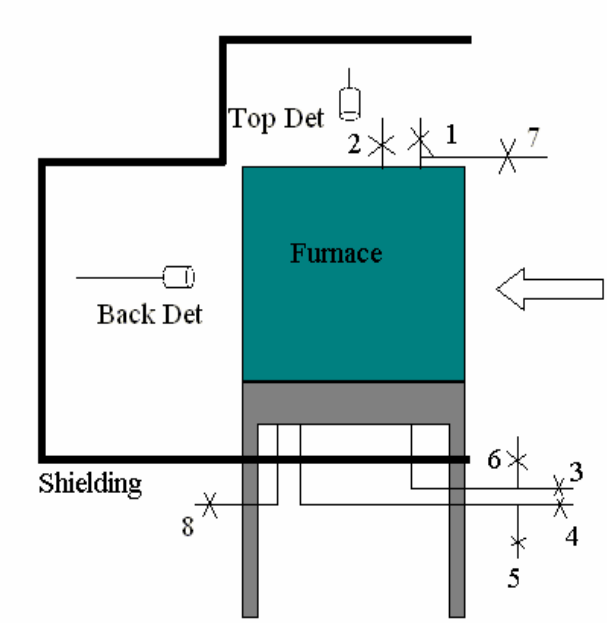

Figure 2-25. Nitrogen cover gas valves system.

- Valve 1: Pressure relief and cooling outlet, 3/8inch diameter, manual flapper
- Valve 2: Emergency outlet, 3/8inch diameter, (not being used currently)
- Valve 3: Nitrogen cooling inlet, 3/8inch diameter, manual control
- Valve 4: Nitrogen supply inlet, 1/4inch diameter, manual control
- Valve 5: Backup nitrogen supply inlet, 1/4inch diameter electronic control
- Valve 6: Air cooling inlet, 3/8inch diameter, manual control
- Valve 7: Nitrogen supply outlet, 1/8inch diameter, manual control
- Valve 8: Nitrogen emergency inlet, 3/8inch diameter, electronic control

Before turning on the heater, valve 4 and 7 are opened and nitrogen comes into the furnace until the oxygen is exhausted, valve 1 is to keep the overpressure of the system during the heating. If the temperature of the system is higher than the warning limit, valve 8 will be opened and a large mount of nitrogen gas will flow in and cool down the graphite. If the nitrogen supply cylinder is empty, the valve 5 will be opened. To cool down the graphite after experiment, valve 3 and 7 will be opened, after the temperature of graphite assembly is below 600^{o}C, valve 6 will be opened to speed up cooling.

Valve 5 and 8 are solenoid valve which can be controlled remotely. The Programmable Logic Controller, which is the FieldPoint module [38] made by National Instrument, provides the power and signal to open and close the valves. The two modules that are used in this case are FP-1601, which is a communicate module with an Ethernet port and FP-DO400, which is 8 channel Sourcing Digital Output Module. A code was written in LabView [37] and tested to fulfill the logical functions shown in Figure 2-26.

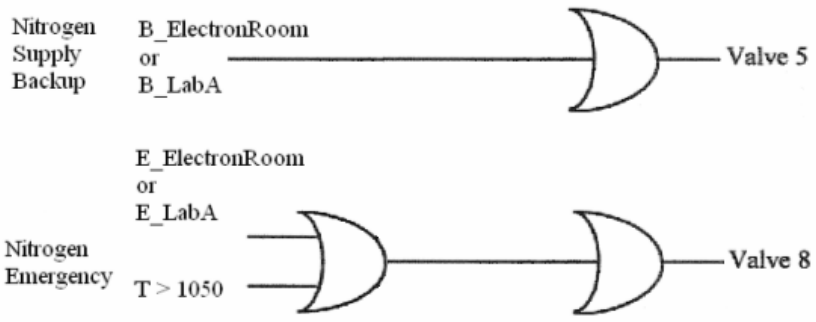

Figure 2-26. Logic diagram of the Programmable Logic Controller used for valve controlling.

The LabView [37] code can also communicate with the MV100, which provide temperature data of the graphite assembly. The T>1050 signal in Figure 2-26 will be coming from the MV100.

2.5.2.3 Heat transfer calculations

The objective of doing heat transfer calculations is to predict the heating time of the graphite assembly from room temperature to 1200K, and to calculate the temperature distribution over the whole system. The calculated temperature distribution of the graphite assembly helps to optimize the design of the furnace in order to provide uniform heating to the assembly.

Giving the initial condition and boundary condition of the system, the heating time and the temperature distribution can be calculated by solving the partial differential heat transport equation, which can be done by using Finite Element Analysis (FEA). FEA is a mathematics technique to find the approximate solution of partial differential equations as well as integral equations, which divide the system into substructure, called "finite elements". FEA was intensively utilized to solve the problem in mechanical engineering and civil engineering, and there are many commercial graphics-based FEA program packages available which are powerful and convenient. ANSYS [39] is one of them and was utilized to perform heat transfer calculations in this work. ANSYS is a general propose comprehensive 3D finite-element modeling program package. It can numerically solve a wide variety of mechanical problems, such as thermodynamic analysis (heat transfer, cooling analysis, temperature gradients, and thermal responses) and structural analysis (torsion computation, vibration, stress analysis on various substances, elasticity).

Figure 2-27 shows the center section of the 3D model in ANSYS based on the heating system design. It consists of the graphite assembly, heater, insulation, support bricks, a layer of air and the polyethylene shielding board. Their thermal properties are shown in the Table 2-1.

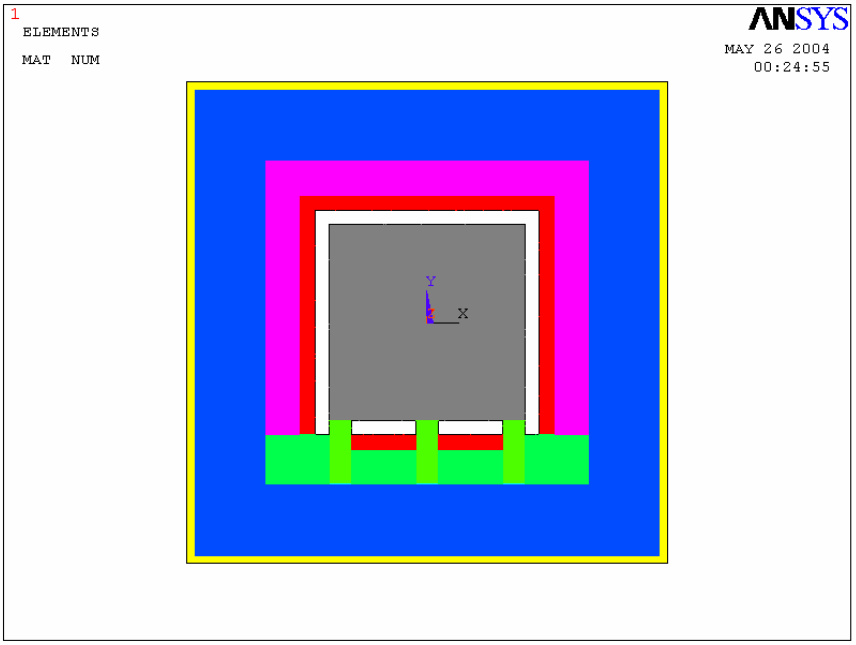

Figure 2-27. ANSYS 3D model of the system. The graphite assembly (gray) is surrounded by the heaters (red), bricks (green) and thermal insulation (pink), the outer (yellow) shell represents the shielding, between the shielding and the furnace, a layer of air (blue) is considered.

The initial state of our model is room temperature (300K). There are two steps. During the first step, the heat generation of the heaters was fixed to 45kw, considering 50kw is the maximum power we can get at the ORELA site; after the temperature of the heater reaches a preset value (e.g., 1200K) the temperature of the heater will be fixed to this value. The input file of the ANSYS model is attached in Appendix B. Figures 2-28 and 2-29 show the temperature evolution of the heater and the center of the graphite assembly, for different preset temperatures. The temperatures of the heater will reach the preset values at different time, but for the center of the assembly, it will always take ~12 hours to heat up to a certain temperature.

Table 2-1. Thermal properties of the furnace materials

Graphite	Temperature (K)	300	500	800	1400
	Density (g/cm^3)	1.7			
	Heat Capacity (J·kg^{-1}·K^{-1})	710	1250	1670	1880
	Thermal Conductivity (W·m^{-1}·K^{-1})	156	118	73	36
Supporting Brick	Temperature (K)	300			
	Density (g/cm^3)	2.179			
	Heat Capacity (J·kg^{-1}·K^{-1})	1047			
	Thermal Conductivity (W·m^{-1}·K^{-1})	0.72			
Aluminum	Temperature (K)	300			
	Density (g/cm^3)	2.7			
	Heat Capacity (J·kg^{-1}·K^{-1})	900			
	Thermal Conductivity (W·m^{-1}·K^{-1})	205			
Heater	Temperature (K)	300	533.15	1088.71	1644.26
	Density (g/cm^3)	2.27			
	Heat Capacity (J·kg^{-1}·K^{-1})	1047			
	Thermal Conductivity (W·m^{-1}·K^{-1})		1.125	1.082	1.139
Bottom Insulation	Temperature (K)	300			
	Density (g/cm^3)	0.49657			
	Heat Capacity (J·kg^{-1}·K^{-1})	1047			
	Temperature (K)	533.15	810.928	1088.71	1366.48
	Thermal Conductivity (W·m^{-1}·K^{-1})	0.13	0.17	0.21	0.25
Wall and Ceiling Insulation	Temperature (K)	300			
	Density (g/cm^3)	0.27231			
	Heat Capacity (J·kg^{-1}·K^{-1})	1047			
	Temperature (K)	533.15	810.928	1088.71	1366.48
	Thermal Conductivity (W·m^{-1}·K^{-1})	0.06	0.10	0.15	0.22
Air	Temperature (K)	300			
	Density (g/cm^3)	0.0012			
	Heat Capacity (J·kg^{-1}·K^{-1})	720			
	Thermal Conductivity (W·m^{-1}·K^{-1})	0.026			
Shielding Polyethylene	Temperature (K)	300			
	Density (g/cm^3)	0.95			
	Heat Capacity (J·kg^{-1}·K^{-1})	1850			
	Thermal Conductivity (W·m^{-1}·K^{-1})	1			

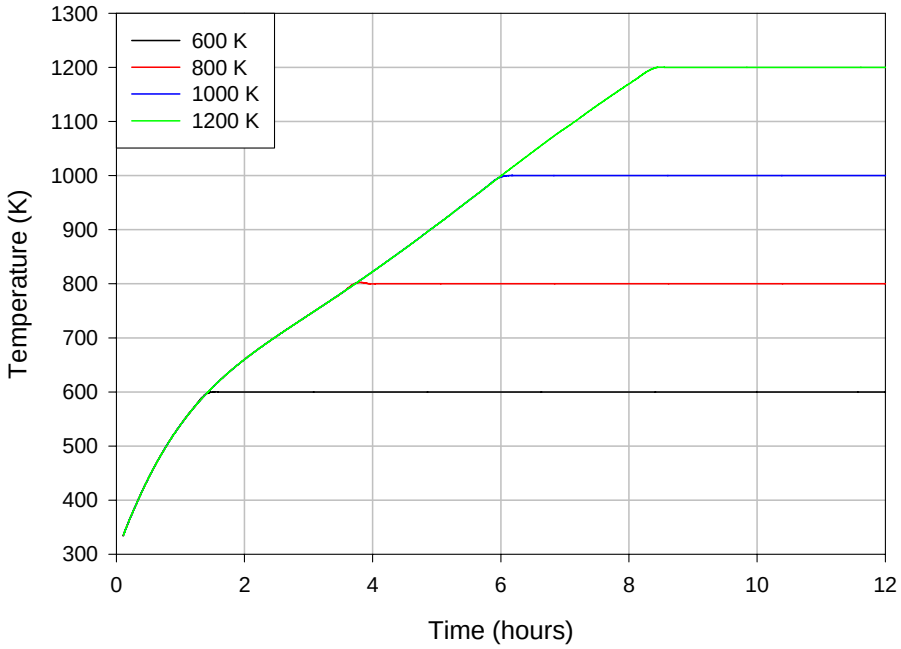

Figure 2-28. Temperature evolution of the heater.

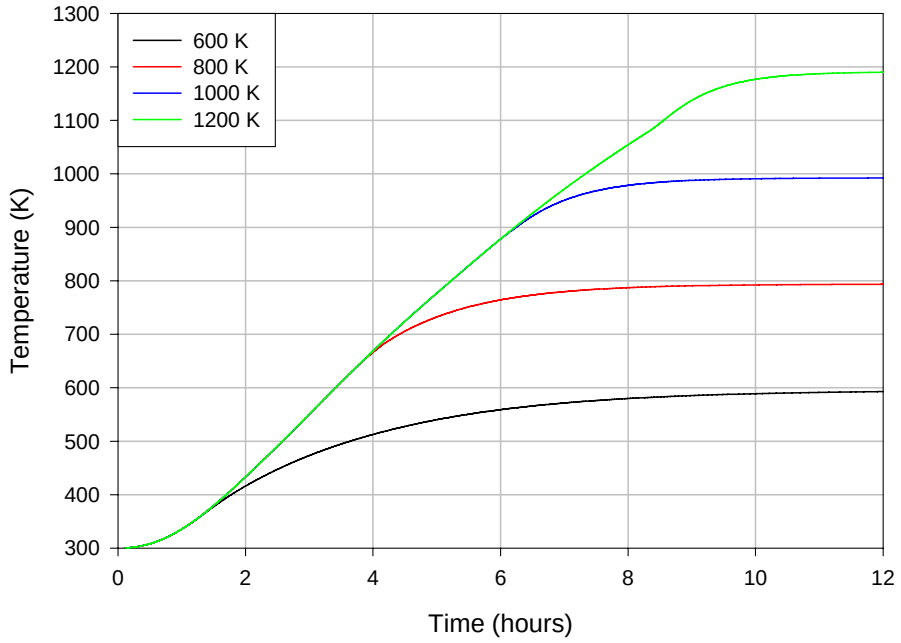

Figure 2-29. Temperature evolution of the center of the graphite assembly.

Figure 2-30 shows the temperature profile of the center cross section after 12 hours heating for a preset temperature of 1200K. As it can be seen, the temperature uniformity is very good, the gradient is less than 50K for the 1200K case. To verify whether the neutron transport response will vary when the graphite has ~40K temperature gradient, thermal neutron libraries at temperature 1160K, 1180K and 1200K were produced by NJOY99 code [40]. By using those libraries, a MCNP model was made to simulate the experiment at 1200K with ~40K temperature gradient in the graphite assembly. The result was compared with the homogenous model, shown in Figure 2-31. The discrepancy between the model with ~40K temperature gradient and the homogenous model are negligible.

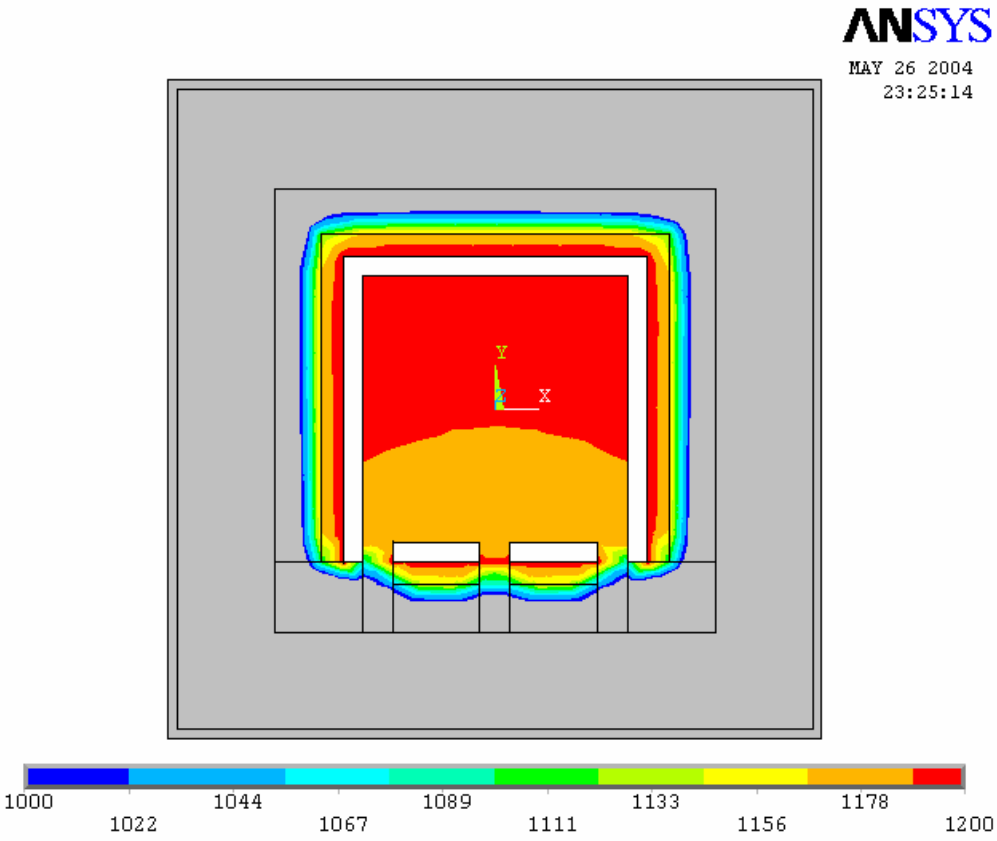

Figure 2-30. Temperature profile of the graphite assembly (center section) after 12 hours heating.

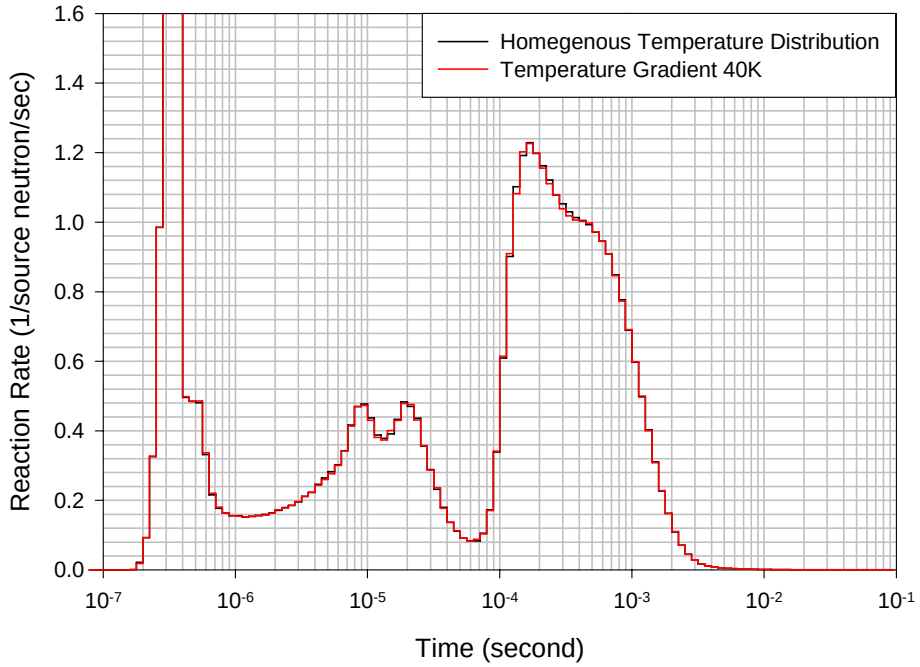

Figure 2-31. The spectrum calculated for a graphite assembly with a temperature gradient shown in Figure2-30 was compared to a spectrum leaking from a homogenous system.

2.5.3 Design of the shielding system

The graphite assembly was setup at the end of the 10m flight path, which is in the Electron Room, shown in Figure 2-1. The room, with dimension of 15m x 10m x 4.6m, is built underground and surrounded by 25cm thick concrete walls. There are 4 different flight paths in this room, some of which were used by other research groups. Neutrons coming from the accelerator will encounter the graphite assembly and be scattered into all the direction. Since the graphite absorbs almost no neutrons, a fairly large amount of neutrons will leak out of the assembly and expand into the whole room. The concrete wall, ground and ceiling does not only slow-down the neutrons and absorb them, but also reflect neutrons back into the room, the graphite assembly or even the detectors. The reflected thermal neutrons are not related to the graphite scattering kernel, therefore when they

are detected they will contaminate the signal. There maybe other potential reflector materials around the graphite assembly. The leakage neutrons also can produce large dose rates.

In order to reduce the room return neutrons and the dose rate around the graphite assembly, and to isolate the graphite assembly and the detectors, a shielding system has to be introduced. The shielding material is provided by Thermo Electron Corporation, which is 5% borated polyethylene with a density of 0.95g/cm^3, a thickness of 2.5cm and a maximum working temperature of 82.2 °C. The polyethylene will slow down the neutrons to the thermal region, in which boron has a very large probability to absorb neutrons. Figure 2-32 illustrates the graphite assembly, furnace, concrete room and the shielding. The shielding system includes two separable parts, the shielding bell and the shielding base, as shown in the Figure 2-33. The shielding bell encloses the top detector, while the shielding base encloses the back detector, furnace and graphite assembly.

Figure 2-34 and 2-35 illustrate the back and top detectors neutron time spectra for the cases of the graphite assembly with the furnace, the concrete room and the shielding system respectively. After introducing the concrete room into the MCNP model, the neutrons will be reflected back into the graphite assembly and detectors, they will contribute to the thermal neutron region (after 0.2msec), which is of most concern to our experiment. After introducing the shielding system, there will be fewer neutrons leaking out from the system so that the room-return effect is reduced from the thermal neutron region.

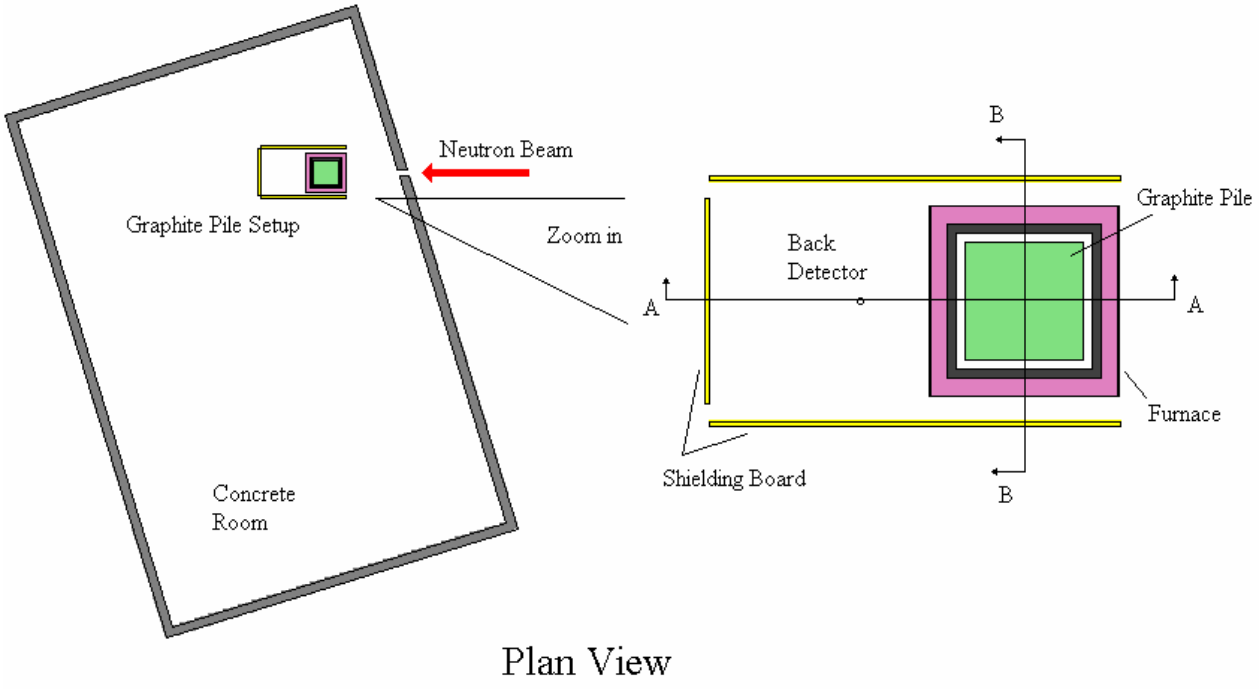

Figure 2-32. The plan view of the MCNP model.

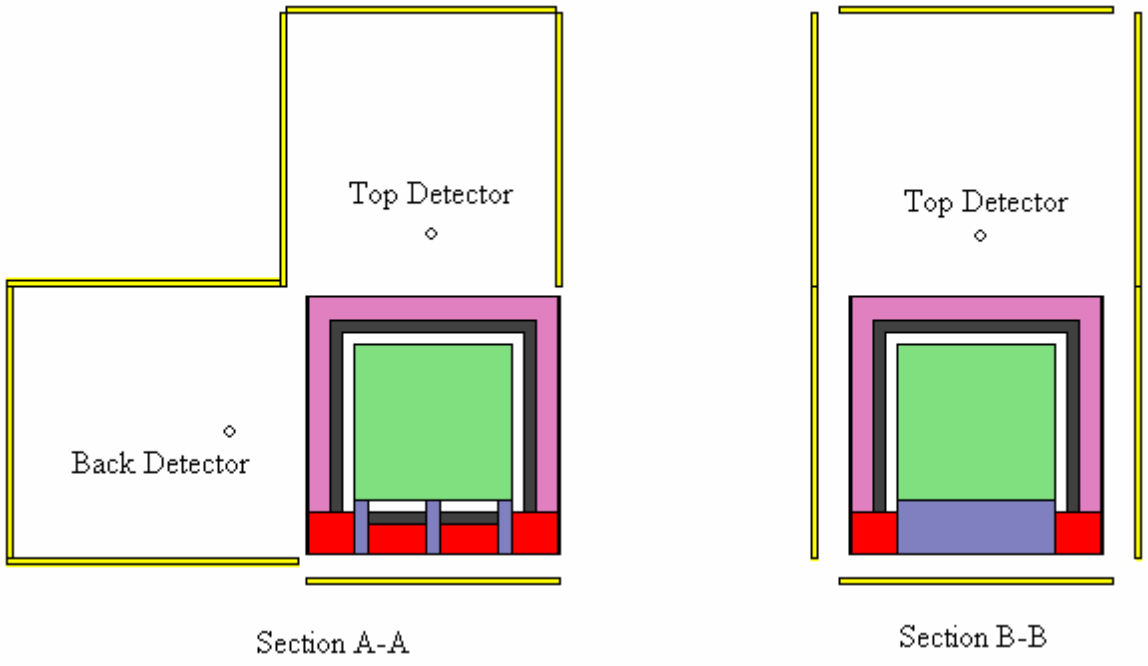

Figure 2-33. The section A-A and B-B views.

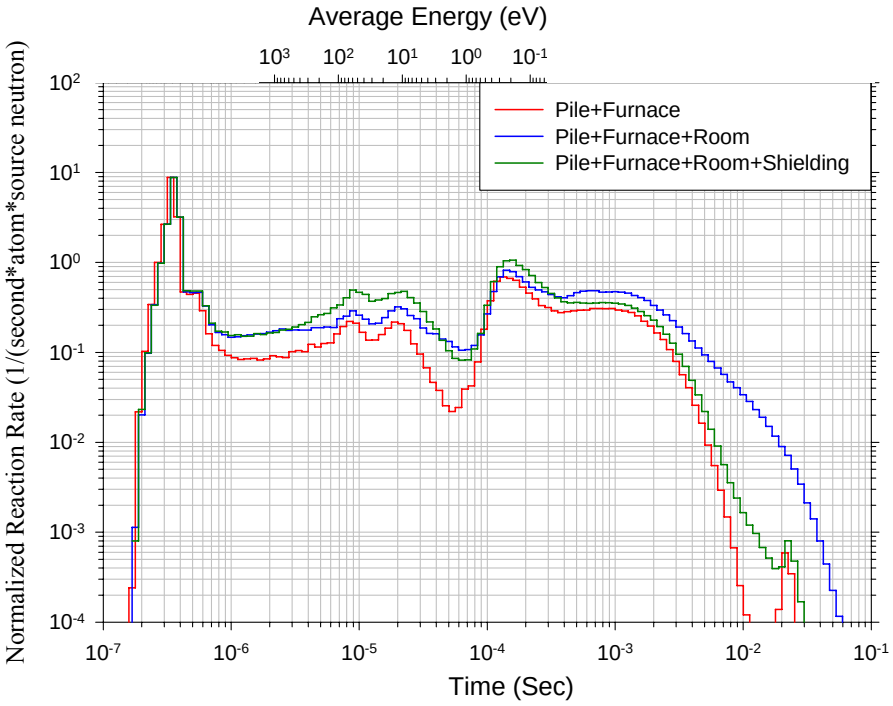

Figure 2-34. Time spectra of the shielding design for the back detector using 70x70x70 cm pile.

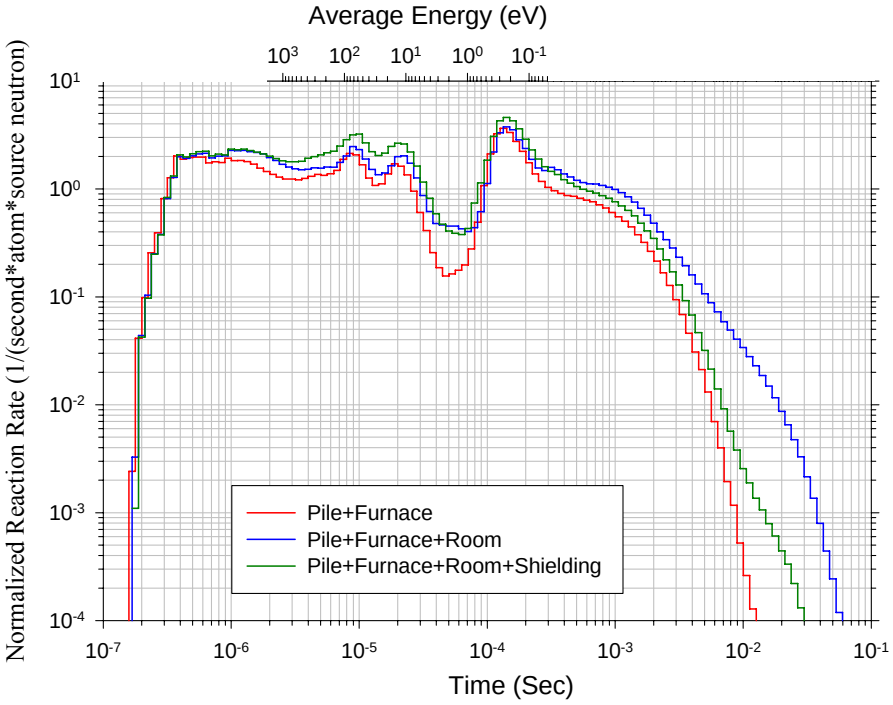

Figure 2-35. Time spectra of the shielding design for the top detector using 70x70x70 cm pile.

Figure 2-36 and 2-37 show the perturbation effect on the time spectra of back and top detectors due to the +3% increasing on the graphite total thermal neutron cross-section for the cases of the graphite assembly with the furnace, the concrete room and the shielding system. As it can be seen, introducing the concrete room into the MCNP model makes the time spectrum much less sensitive to the graphite total thermal neutron cross-section. This can be explained by the fact that the time spectrum is contaminated by neutrons leaking out from the graphite assembly and neutrons reflected by the concrete room, and the later one is not sensitive to the graphite thermal neutron cross-section at all. After introducing the shielding system, the contribution to the time spectrum from the reflecting neutrons is reduced. Therefore the sensitivity of the time spectrum to the thermal neutron cross-section is recovered.

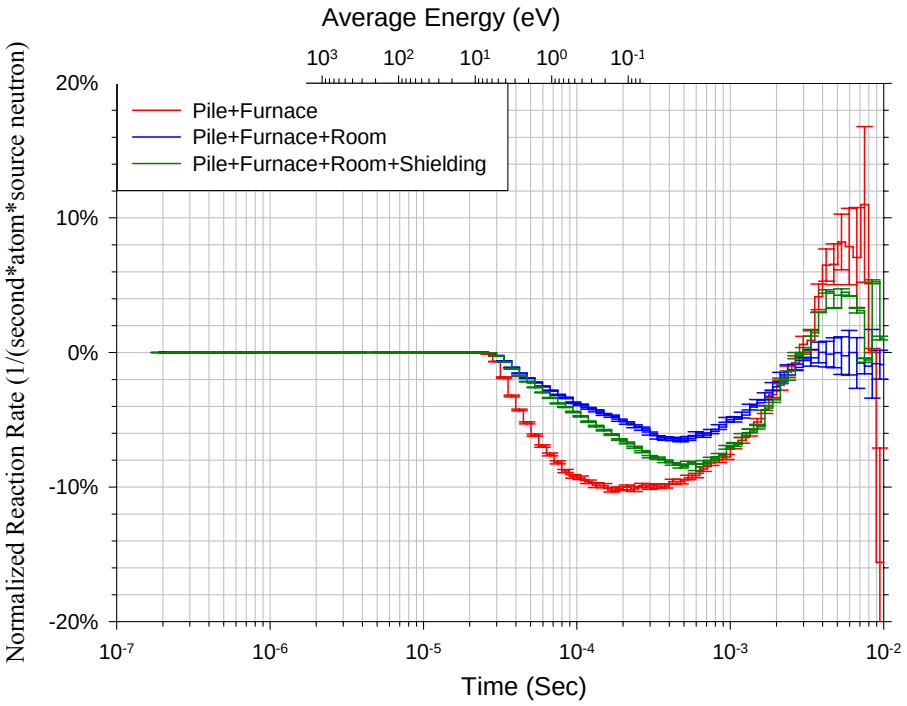

Figure 2-36. The perturbation calculations on the time spectra of the back detectors due to the +3% increasing on the graphite total thermal neutron cross-section for the cases of the 70x70x70 cm graphite assembly with the furnace, the concrete room and the shielding system.

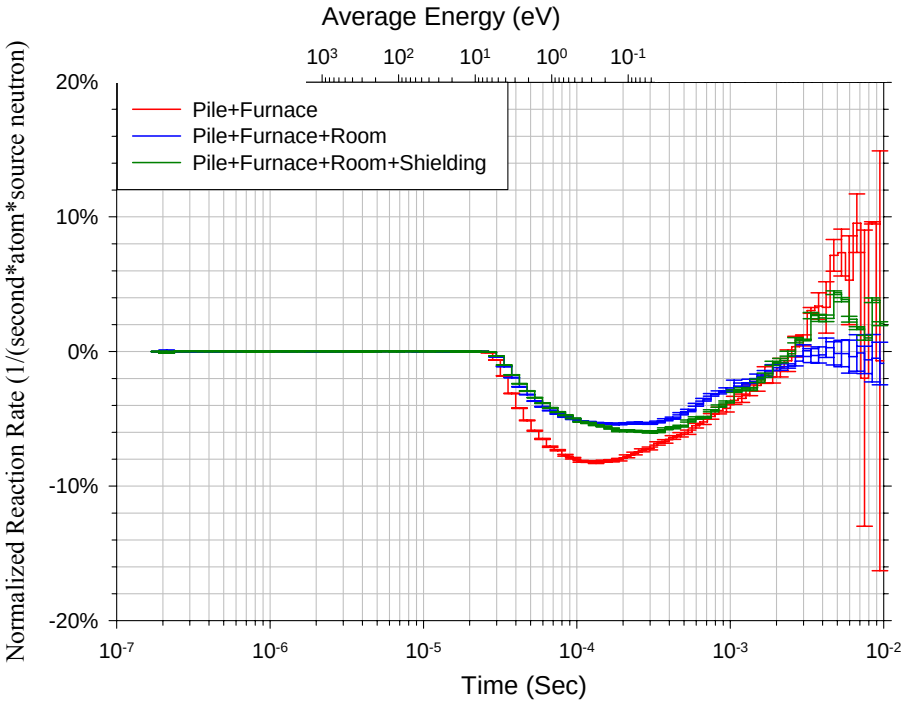

Figure 2-37. The perturbation calculation on the time spectra of the top detectors due to the +3% increasing on the graphite total thermal neutron cross-section for the cases of the 70x70x70 cm graphite assembly with the furnace, the concrete room and the shielding system.

2.5.4 Experimental equipment setup

The graphite assembly, heating system, shielding system and data acquisition system were setup at the 10m station in the Electron Room, shown in Figure 2-1. During the experiment, the operator will be in the data acquisition room, which is called Lab A. The temperature of the assembly and detector response will be monitored by the operator in Lab A over a local area computer network. In addition, there are 6 web cams in the Electron Room to provide several views and the valve system and heater controller can be remotely controlled by the person in Lab A.

2.5.4.1 Setup in Lab A

A laptop was setup in the data acquisition room Lab A to monitor the Electron Room, the temperature of the system, neutron spectrum, and to control the valve system, and the furnace controller. To perform these tasks, the laptop was connected to a hub in the Electron Room by using a BNC cable. In this way, the laptop can be in the same network with the equipment and computers in the Electron Room. The laptop and the computers in the Electron Room are running Windows XP system. By using the remote desktop connection, the operator in Lab A can login to the computers in the Electron Room through the laptop without physically being present in the Electron Room. As a result, the operator can get full control of the computers as well as the equipments connected to the computers in the Electron Room.

2.5.4.2 Setup in the electron room

2.5.4.2.1 Graphite

Originally, there are 90 150x10x10 cm graphite stringers. In order to build graphite assemblies with three different sizes, the original stringers have to be cut into small pieces. 25 units of the original pieces were cut into 50 pieces of 70x10x10 cm stringers; 45 units of the original pieces were cut into 45 pieces of 50x10x10 cm graphite stringers and 45 pieces of 100x10x10 cm graphite stringers.

There are 10 thermocouples that need to be installed inside the assembly to monitor the temperature of the 70 cm graphite assembly. To do so, 6 pieces of 70cm stringers, labeled from A to B respectively, were drilled. The placements of the holes for the thermocouples in each

stringer are shown in Figure 2-38. A slot on the surface of each stringer was also drilled for holding the thermocouple cables. The drilled stringers with other 70cm stringers are stacked in the order shown in Figure 2-39 to obtain the thermocouple distribution in Figure 2-24.

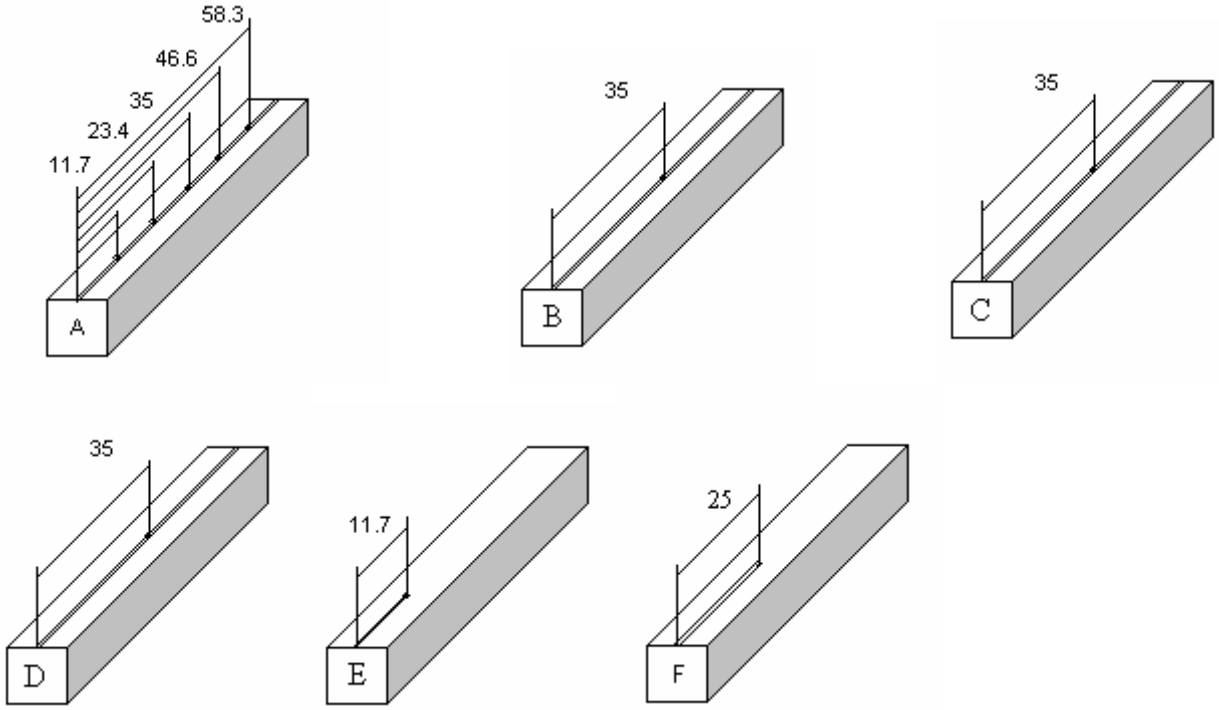

Figure 2-38. Drilling positions for thermocouples (unit : cm).

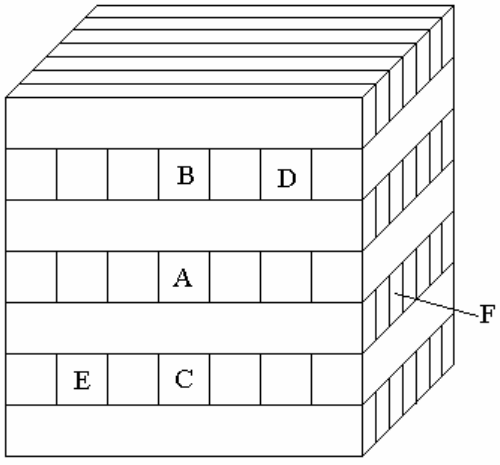

Figure 2-39. 70cm by 70cm by 70cm Graphite Assembly.

The 100x100x100cm and 50x50x50cm graphite assemblies are built by stringers stacked in the order shown in Figure 2-40. Figure 2-41 shows the pictures of the graphite assemblies with three sizes.

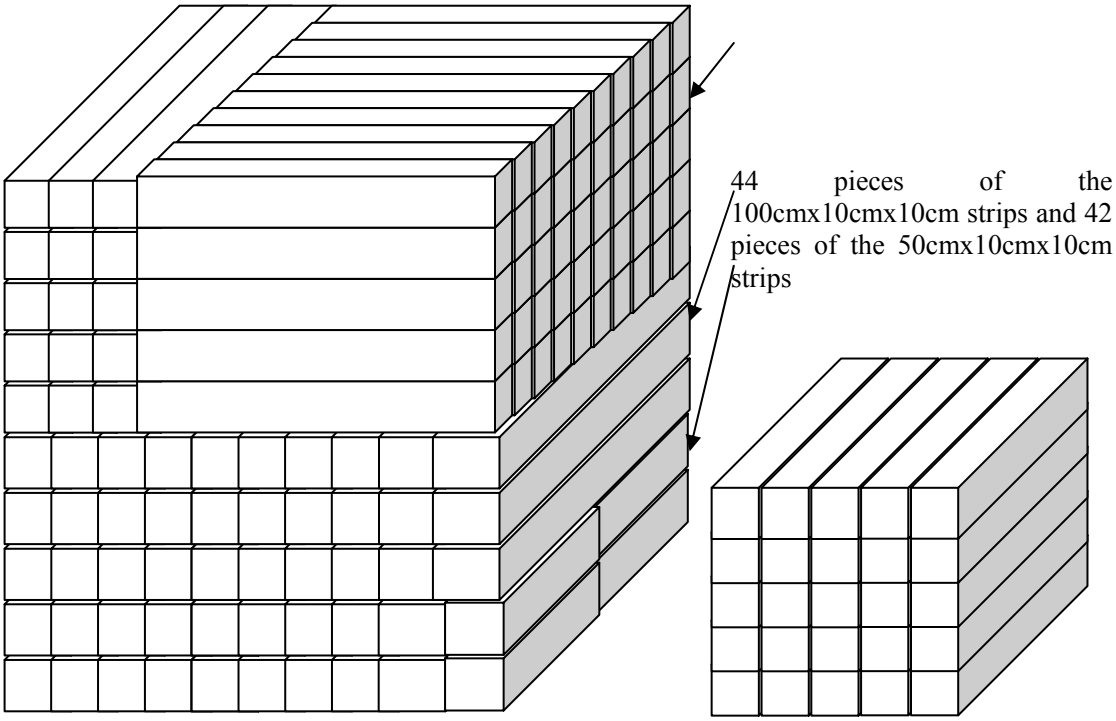

Figure 2-40. 100cm by 100cm by 100cm assembly and 50cm by 50cm by 50cm assembly.

Figure 2-41. Three graphite assemblies with different sizes.

2.5.4.2.2 Furnace and shielding

The furnace table was placed in order to make the graphite assembly perpendicular to the incoming neutron beam, the center of the graphite assembly aligned with the center of the beam, and the

distance from the center of the graphite assembly face to the wall is 2 meter. To get the neutron spectrum leaking out from the graphite assembly, one of the two detectors was setup on the top of the assembly, and the other on the back, 25cm away from the center of the furnace surface. In order to hold the slabs of the polyethylene shield and the detectors, a frame, which is made of 14-gauge medium duty slotted angle with dimension 2.6" x 1.75" x 0.102" x 12', was assembled around the furnace table and graphite assembly shown in Figure 2-42. The polyethylene slabs were cut into 48" x 48" x 1" pieces and mounted onto the frame with bolts and nuts. The frame includes two parts: the bell, which holds the polyethylene slab to shield the top detector; and the base, which encloses the graphite assembly and the back detector. Figure 2-43 shows the picture of the frame and the furnace table.

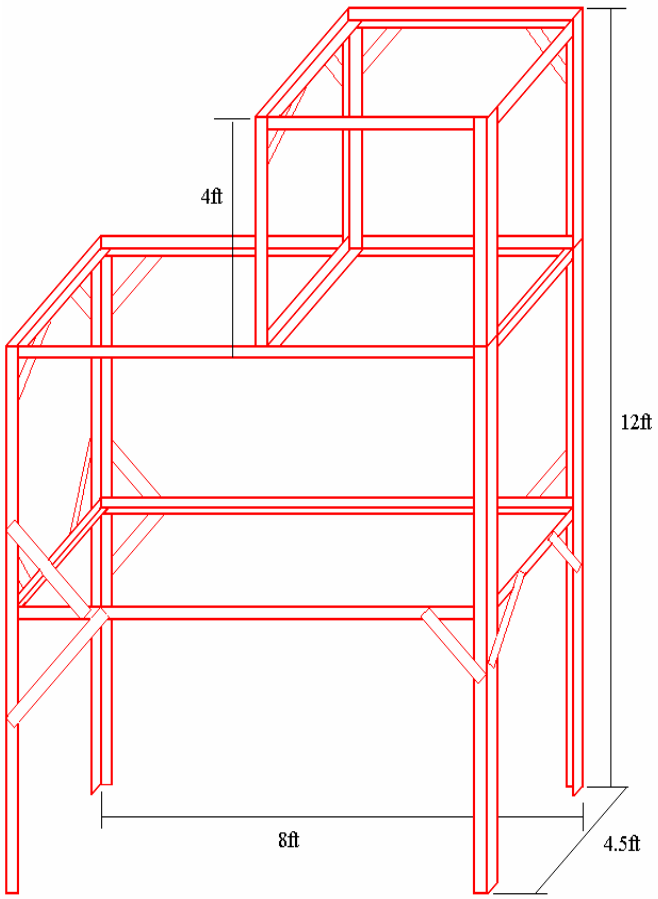

Figure 2-42. Structure of the frame.

Figure 2-43. The furnace table and frame.

For the room temperature measurement, the graphite assembly will be loaded on the furnace table while the furnace bell (shown in Figure 2-44) will not be loaded to reduce the neutron attenuation. The room temperature setup is shown in Figure 2-45, including the frame base, frame bell, polyethylene slabs, and furnace table. The two stairs in Figure 2-45 were used to help to mount the polyethylene slab, load and unload the frame bell. For high temperature measurements, the furnace bell will be loaded by the crane in the Electron Room onto the furnace table. Before the furnace bell is loaded, the polyethylene slabs have to be removed from the frame bell and the frame bell has to be moved from the top of the frame base. In this way the furnace bell can be loaded from the top into the frame base.

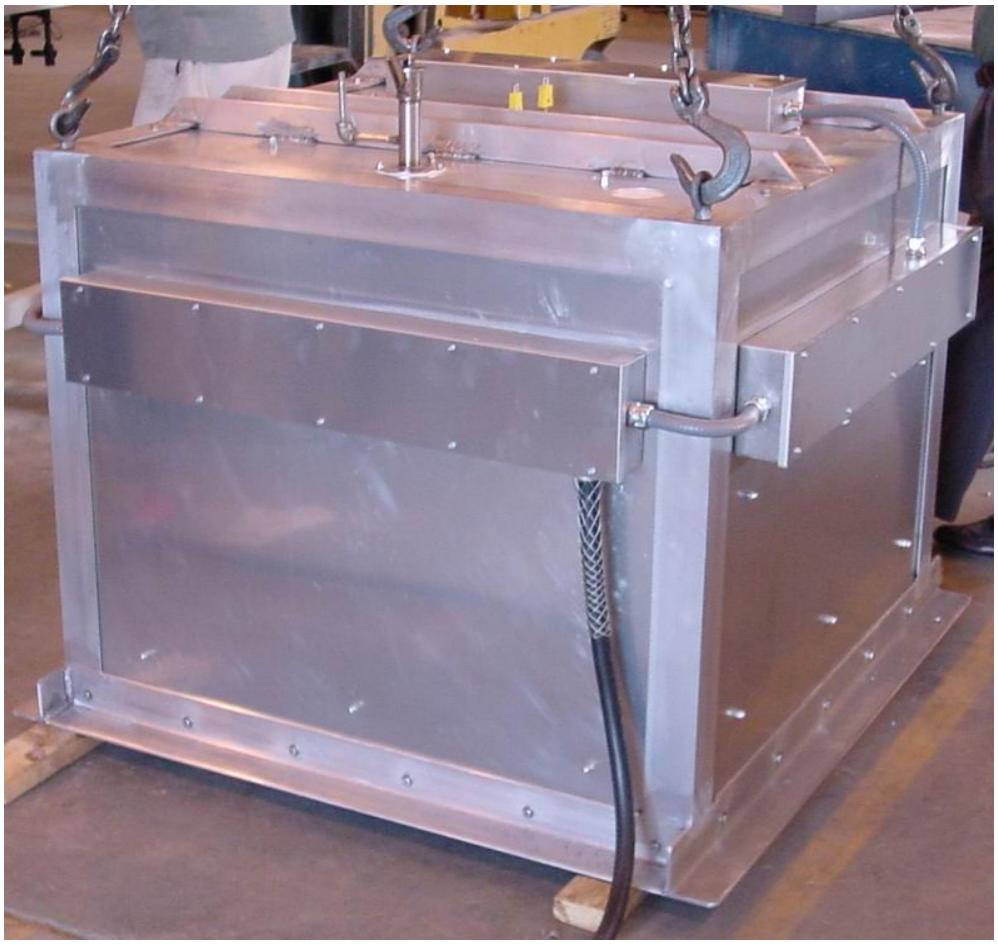

Figure 2-44. The furnace bell.

Figure 2-45. The assembly (include frame base, frame bell, polyethylene slabs, furnace table and two stairs).

2.5.4.2.3 Data acquisition system

The MCA (Multi Channel Analyzer) computer and MCS (Multi Channel Scaler) computer were setup in Electron Room. They are connected to a laptop in Lab A and the equipments (MV100 and FieldPoint PLC for the Valves system) through a network hub in Electron Room. There are 6 web cams connected to two computers through a USB hub, which can give a close view of Electron Room. What need to be monitored are the detectors, the furnace controller readout, the whole shielding frame, the regulator of the nitrogen gas cylinders, and the polyethylene slab under the furnace table (concern about melting).

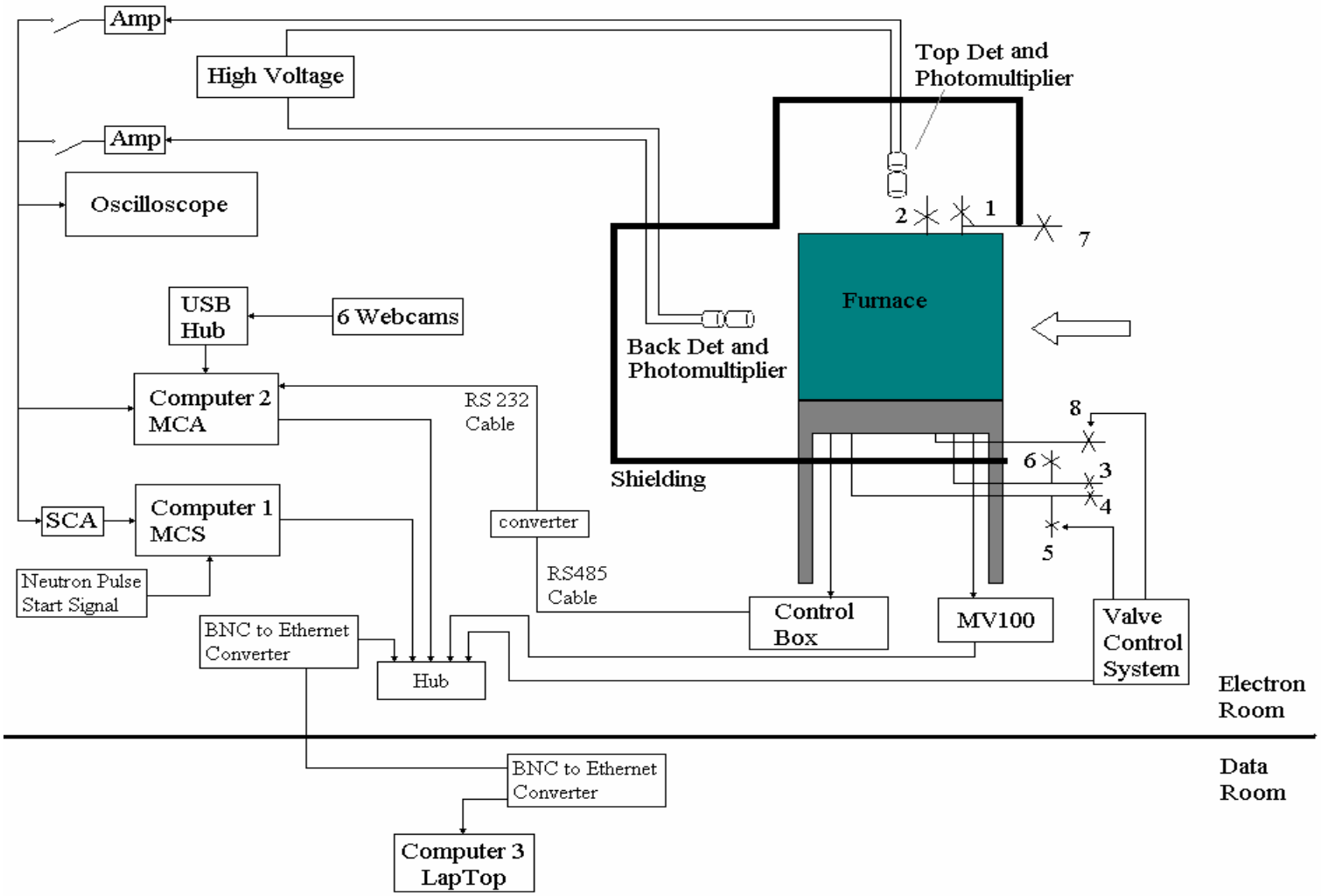

Figure 2-46. Connection diagram.

The two Timing single channel analyzers, two Amplifiers, two High Voltage modules and NIM bin, were setup in the Electron Room. Two Li-6 detectors, photomultipliers and preamps were connected and mounted in the detector holder on the top and back. The detector signals from the preamp were amplified by an amplifier. After that the signal was split into two signals by a T split, one of them went to the MCA and the other went to the MCS through a Timing Single Channel Analyzer, shown in Figure 2-46. The gamma background can be monitored by the MCA which was in the PHA mode and the time spectrum was measured by the MCS. At one time, the signal from only one detector, either back or top detector, can be measured by both MCA and MCS. Figure 2-46 illustrates the connection of all the electronics in both the Electron Room and Lab A.

2.5.5 Temperature effect

Using the MCNP model including the graphite assembly, furnace, concrete room and shielding system as described above, simulations were performed to investigate the variation in the Pu-239 detector response (i.e., the time spectrum) as a function of the graphite temperature. Figure 2-47 shows the calculated time spectra at temperatures of 300K, 800K and 1200 K. As it can be seen, the time spectra are identical up to approximately 1.3×10^{-4} s, which corresponds to an average energy of the neutron spectrum of 0.3 eV. After that point, the spectra deviate with a clear increase in the reaction rate at earlier times as the temperature increases. This can be explained by the shift of the thermal neutron spectrum to higher energies as the temperature of the graphite assembly is increased within the time period 10^{-4} to 10^{-2} s. This behavior can be verified by examining Figure 2-48.

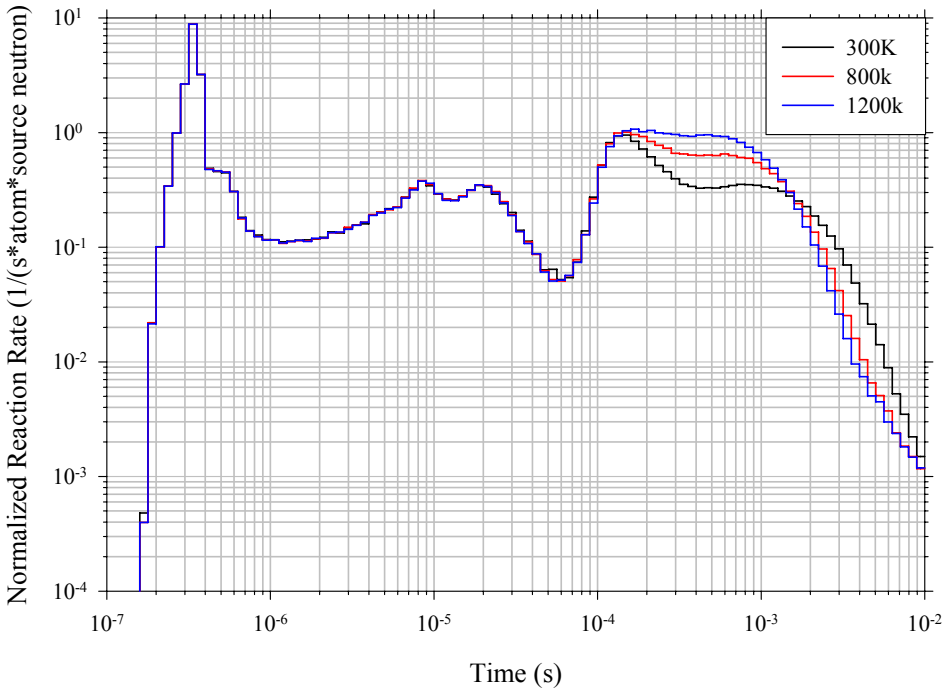

Figure 2-47. The temperature effect on the Pu-239 detector time spectrum.

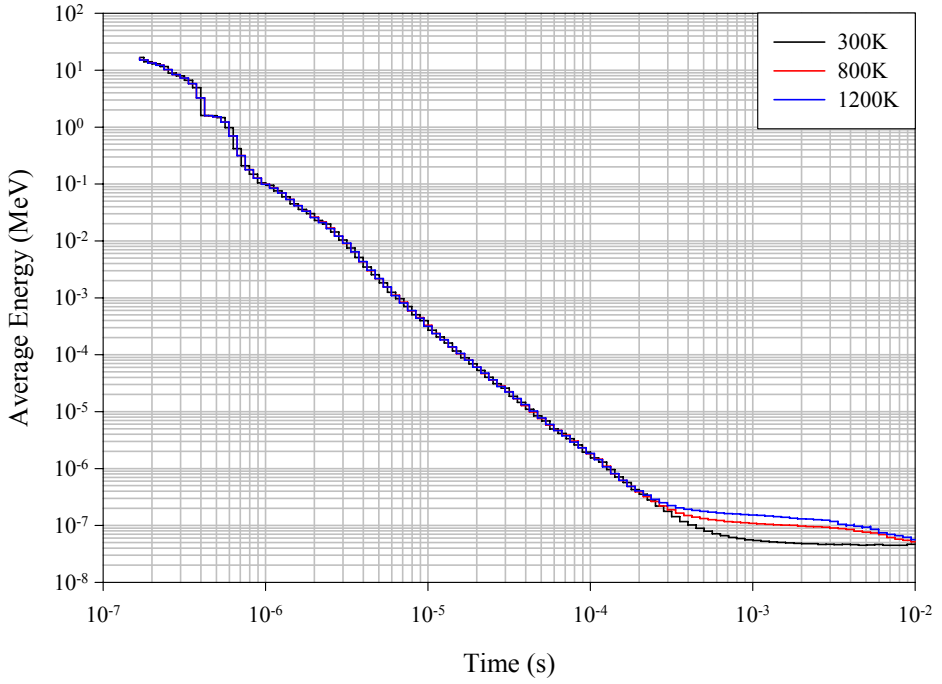

Figure 2-48. The variation of the neutron average energy with temperature.

2.5.6 Uncertainty analysis

2.5.6.1 Detector counting rate

ORELA has 10^{11} neutron/pulses running at a power of 50kw. The diameter of the collimator is 3inch, and the flight path is 10m length. Assume the experiment is running at the frequency 130 pulses/second, the neutron intensity at the surface of the graphite assembly is calculated to be $4.7\text{x}10^{7}$ n/second. There are four detectors available, Pu-239 fission chamber, U-235 fission chamber, Li-6 glass detector and Li-6 ZrS detector. The numbers of atoms in the detectors are$1.26\text{x}10^{-6}$ (Pu-239), $3.33\text{x}10^{-4}$ (U-235), 0.071(Li-6) and 0.084 (Li-6) atoms (cm^2/barn) respectively, which are calculate in equation 2.54 to 2.57. More details will be discussed in Chapter 4.

$$NA_{Pu239} = \frac{m}{M} \times N_A = \frac{0.5 \times 10^{-3}}{239} \times 0.6022 = 1.26 \times 10^{-6} atom(\frac{cm^2}{b}) \tag{2.54}$$

$$NA_{U235} = \frac{m}{M} \times N_A = \frac{0.12988}{235} \times 0.6022 = 3.33 \times 10^{-4} atom(\frac{cm^2}{b}) \tag{2.55}$$

$$NA_{Li6Glass} = \frac{m}{M} \times N_A = \frac{(\frac{3}{2} \times 2.54)^2 \pi \times 0.1 \times 2.5 \times 6.6\%}{6 \times 95\% + 7 \times 5\%} \times 95\% \times 0.6022 = 0.071 atom(\frac{cm^2}{b}) \tag{2.56}$$

$$NA_{Li6ZnS} = \frac{m}{M} \times N_A = \frac{(\frac{5}{2} \times 2.54)^2 \pi \times 0.635 \times 0.011}{6 \times 95\% + 7 \times 5\%} \times 95\% \times 0.6022 = 0.084 atoms\ (\frac{cm^2}{barn}) \tag{2.57}$$

Based on the time spectra from MCNP simulation by using four different detectors, the counting rate for each time bins in the time spectrum can be calculated by:

$$\text{CR} = \text{MCNP\_Tally}(\frac{\text{barn}}{\text{cm}^2} \cdot \frac{1}{\text{source} \cdot \text{neutron}}) \times \text{Neutron\_Intensity}(\frac{\text{neutron}}{\text{second}}) \times \text{No.\_atom}(\text{atoms} \cdot \frac{\text{cm}^2}{\text{barn}}) \tag{2.58}$$

The time spectra for the different detectors at the back and top are shown in Figure 2-49 and 2-50. The time-bin counting rates for different detectors are shown in Figure 2-51 and 2-52. As it can be seen, the counting rates for the same detector at the top are higher than at the back by a factor of 2 to 3 (depending on the time). The two Li-6 detectors have similar and relatively high counting rates, the U-235 fission chamber has a lower counting rate and the Pu-239 fission chamber has the lowest one. However, the Pu-239 detector can produce a time spectrum that has several features (including the peak corresponding to the Pu-239 0.3 eV), which can be used in time-energy calibration even for the other detectors. In this experiment, Li-6 detector will be used for most cases, and the Pu-239 fission chamber will be used for extended time measurement.

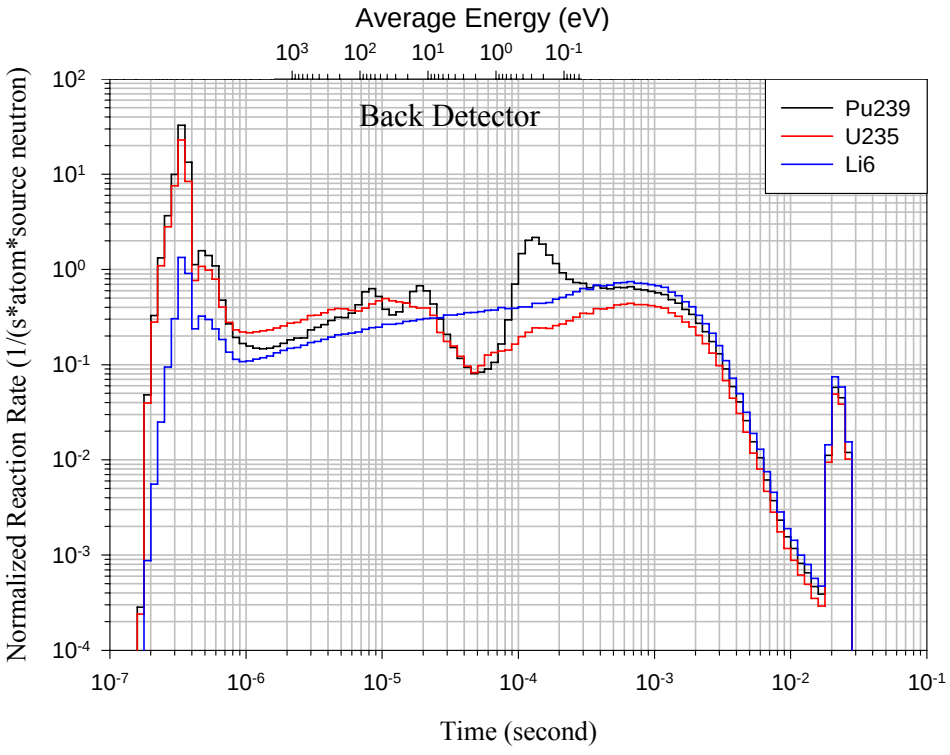

Figure 2-49. Time spectra for the Pu-239, U-235 fission chamber and Li-6 detector at the back.

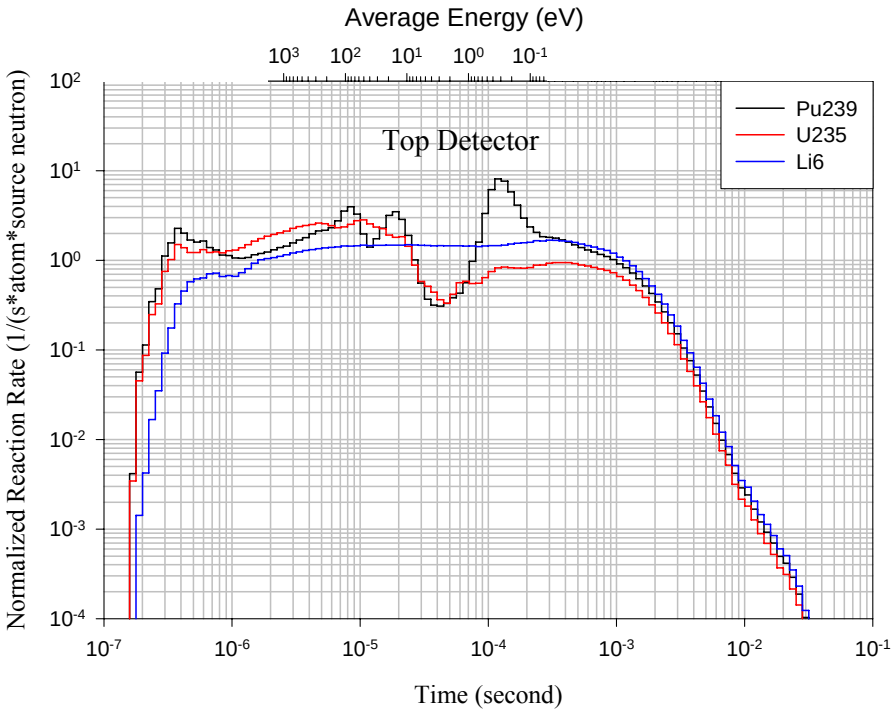

Figure 2-50. Time spectra for the Pu-239, U-235 fission chamber and Li-6 detector at the back.

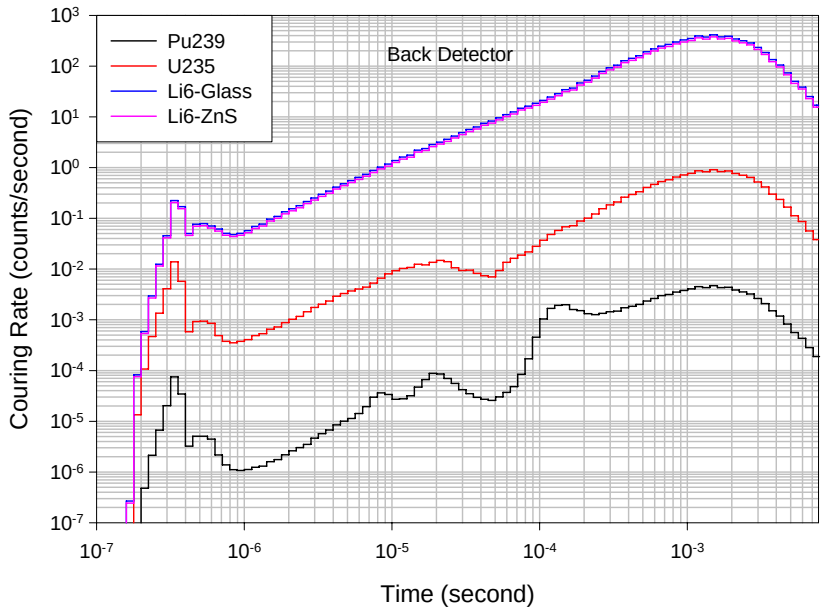

Figure 2-51. The counting rate of the four detector at the back.

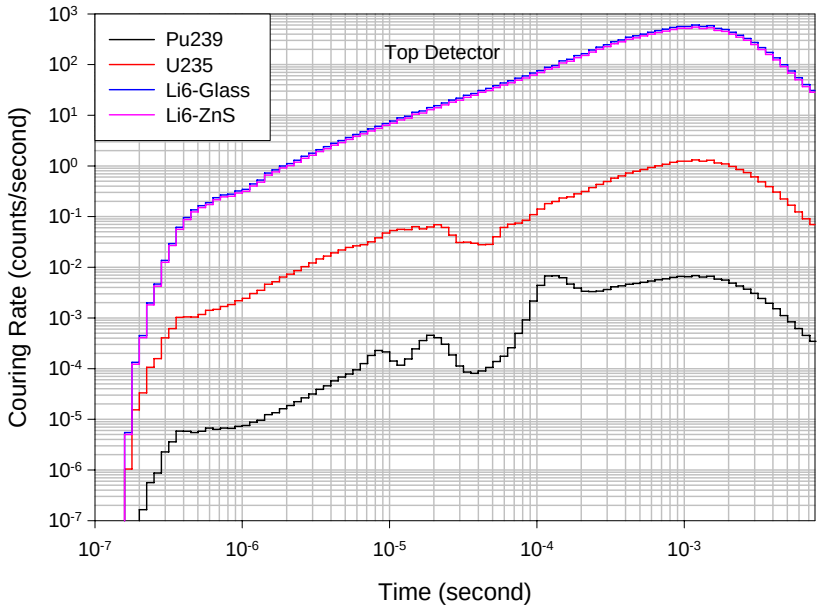

Figure 2-52. The counting rate for the four detectors at the top.

As it can be seen in Figure 2-52, in the time region 10^{-4} to 10^{-3} second after a neutron source pulse, the minimum counting rates within a time bin are 70 counts/sec, 0.1 counts/sec and 0.003 counts/sec respectively for Li-6 detector, U-235 detector and Pu-239 detector at the top. To distinguish 5% to 10% difference on the spectrum in this time region, the statistical error should be at least smaller than 1%. Assuming that the detector counting satisfies Poison statistics, $\frac{\sigma_N}{N} = \frac{1}{\sqrt{N}} = 1\%$, then N=10000. Therefore, the measurement time by using Li-6 detector should be longer than $\frac{10000}{70} \approx 143\,\text{secs} \approx 2.4\,\text{mins}$; the measurement time by using U-235 detector should be longer than $\frac{10000}{0.1} = 100000\,\text{secs} \approx 1667\,\text{mins} \approx 27.8\text{hrs}$; the measurement time by using Pu-239 detector should be longer than $\frac{10000}{0.003} = 3 \times 10^7\ \text{secs} \approx 8333 hrs$.

In the realistic case, the Li-6 detector will be utilized to measure the time spectrum with 1 hour measurement time. This can give a statistical error smaller than 0.2% on the time bins within 10^{-4} to 10^{-3} second after a neutron source pulse. The U-235 detector will be utilized for one case with a long measuring time to illustrate the coupling of the slowing down time and neutron average energy due to the resonance structure in U-235 fission cross-section. Calculation shows that the counting rate of detector in the center of graphite assembly is 2 orders of magnitude higher than the detector at the back. That makes it possible to use the Pu-239 detector in the center within a reasonable measurement time.

2.5.6.2 Optimizing the detector position

So far, the detector was placed 46.27cm away from the graphite assembly surface, i.e. 25 cm away from the furnace surface in all of the MCNP models discussed above. The time spectra of the detector at 27.5 cm and 37.5 cm away from the assembly were also calculated by MCNP5 code and shown in Figure 2-53 and 2-54 for the back and top detectors. As it can be seen, the source peaks in the time spectra for the three detectors are almost the same. That is because the neutron source is more than 10 m away from the detector so that the solid angles the detectors subtended are almost the same for the three positions and the flight time of source neutrons to the detector at different positions are same. It can also be seen in Figure 2-53 ad 2-54 that when the detector closer to the assembly, the time spectra of scattered neutrons are higher and the Pu-239 signature peak that happen at earlier time. That is because the graphite assembly will scatter neutrons into every direction so that the assembly can be treated as a neutron source. When moving the detector close to the assembly, the solid angle the detector subtended will increase and flight times of scattered neutrons decrease. Therefore the number of neutrons which can be detected will

increase and scattered neutron spectrum will move to earlier time. Figure 2-55 and 2-56 show the perturbation effect on the time spectra of back and top detectors due to the +3% increasing on the graphite total thermal neutron cross-section for the cases with different detector positions. As it can be seen, the sensitivities of the models remain the same when moving detector away or close to the graphite assembly.

By moving the back or top detector close to the graphite assembly, one can obtain a higher counting rate with the sensitivity to the graphite total thermal neutron cross-section remaining the same. However, for the high temperature measurement, the detector will be placed at 25 cm away from the furnace surface (i.e. 46.27cm away from the assembly surface) due to the high temperature on the furnace surface.

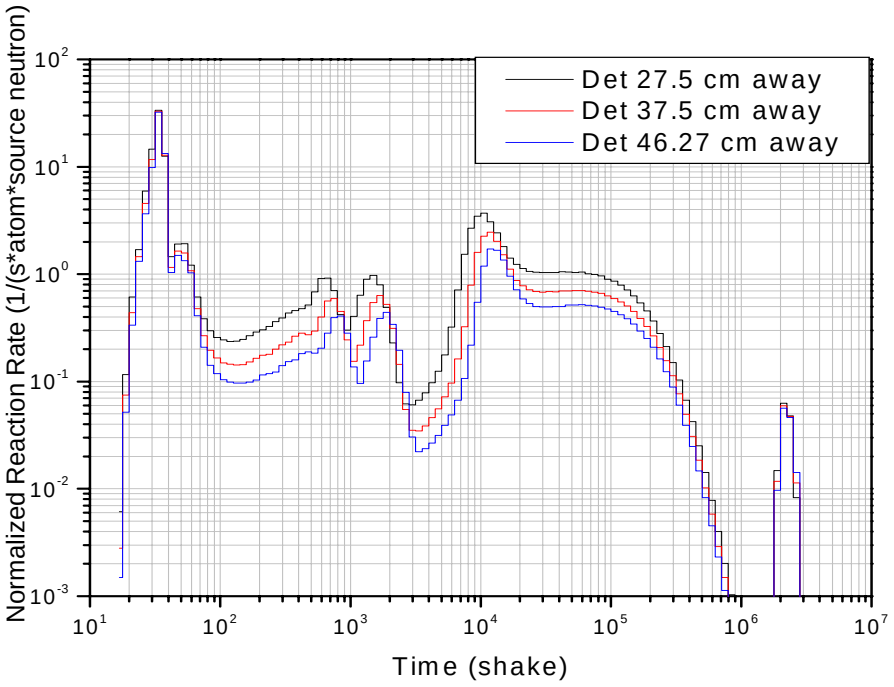

Figure 2-53. The time spectra of the back detector at different locations.

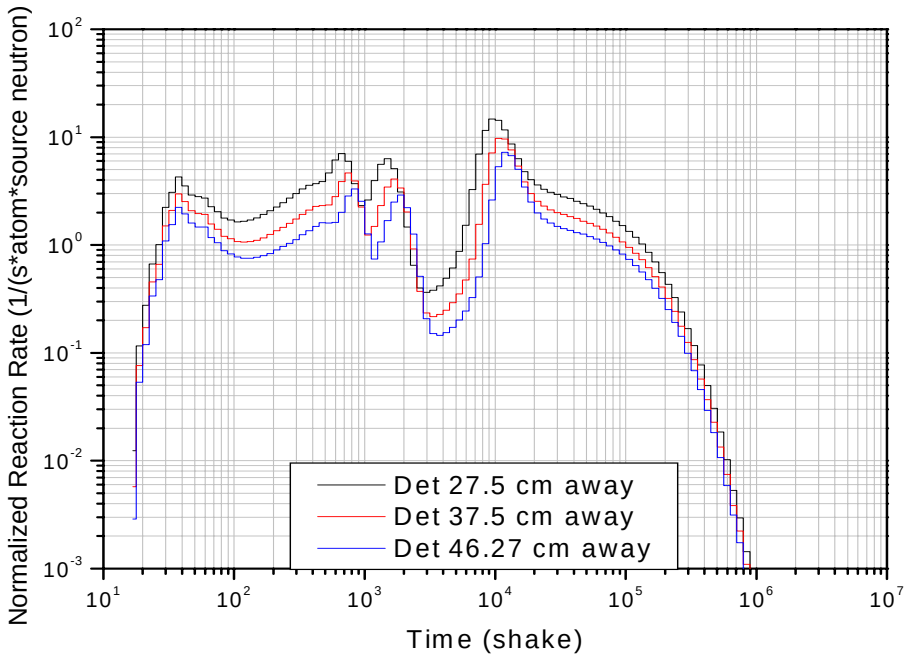

Figure 2-54. The time spectra of the top detector at different locations.

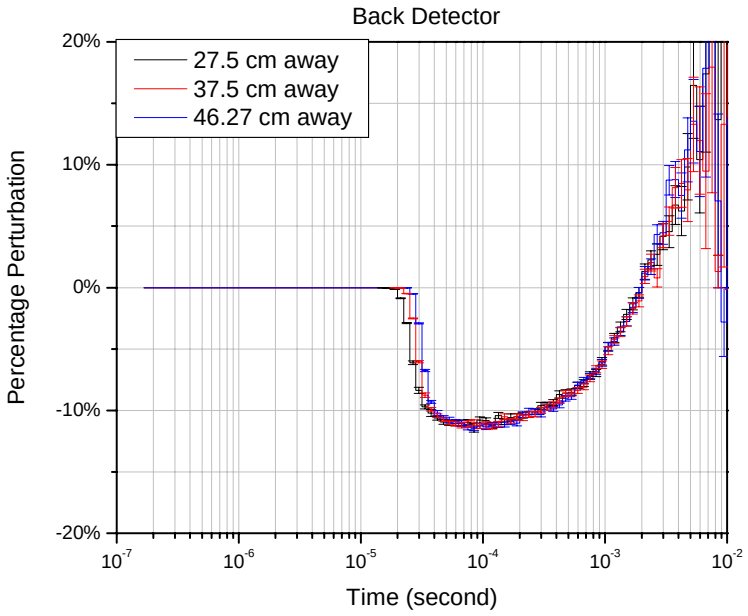

Figure 2-55. The perturbation calculation of the back detector at different locations due to the +3% increasing on the graphite total thermal neutron cross-section.

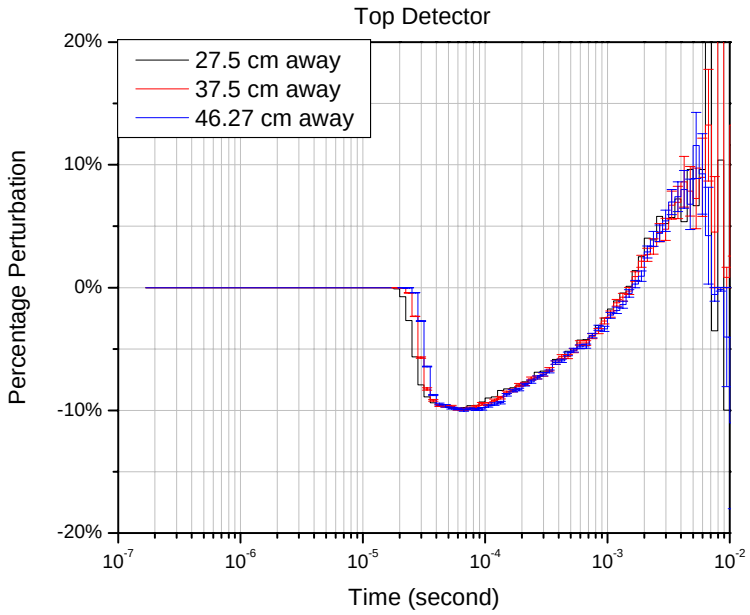

Figure 2-56. The perturbation calculation of the back detector at different locations due to the +3% increasing on the graphite total thermal neutron cross-section.

2.5.6.3 Pulse overlap effect

The ORELA facility is a pulsed neutron source and each pulse will produce one time spectrum in the MCS. After a certain time measurement, the time spectra produced by every pulse within this time period will be accumulated to become the final time spectrum in the MCS. The time spectrum of one source pulse spreads from $2x10^{-7}$ to 0.03 second after the pulse, shown in Figure 2-4. If the pulsed neutron source has a very high frequency, the coming neutron pulse can arrive before 0.03 second after the previous pulse. Since the time spectrum in the MCS corresponding to the previous pulse did not completely die away, a pulse overlap effect in the neutron time spectra will happen.

When the time spectrum is measured at a neutron pulse frequency of 1000 pulses/second, the

sweep time of the MCS need to be setup to 1/1000 second. Since the time spectrum for each neutron pulse can extend to 0.03 second after the pulse, the time spectrum for one neutron pulse can be affected by the thirty source pulses which appeared before the current neutron pulse. In order to study this pulse overlap effect and optimize the frequency of the pulse neutron source, the pulse overlap time spectra of Pu-239 detector were calculated (shown in Figure 2-57 and 2-58) based on the MCNP simulation at source frequencies of 525 and 130 pulses/second, which are the most likely frequencies at which ORELA will be operated. As it can be seen in Figure 2-57 and 2-58, the frequency of 525 pulses/second has a very large pulse overlap effect and a smaller cutoff time, which is 1/525 second. While the frequency of 130 pulses/second has a very small pulse overlap effect and a longer cutoff time 1/130 second. Clearly, the lower frequency is preferred. The percentage effect of pulse overlap at the frequency of 130 pulses/second is around 1% to 2% in the time period 10^{-4} to $3x10^{-3}$ second after a source neutron pulse, shown in Figure 2-59.

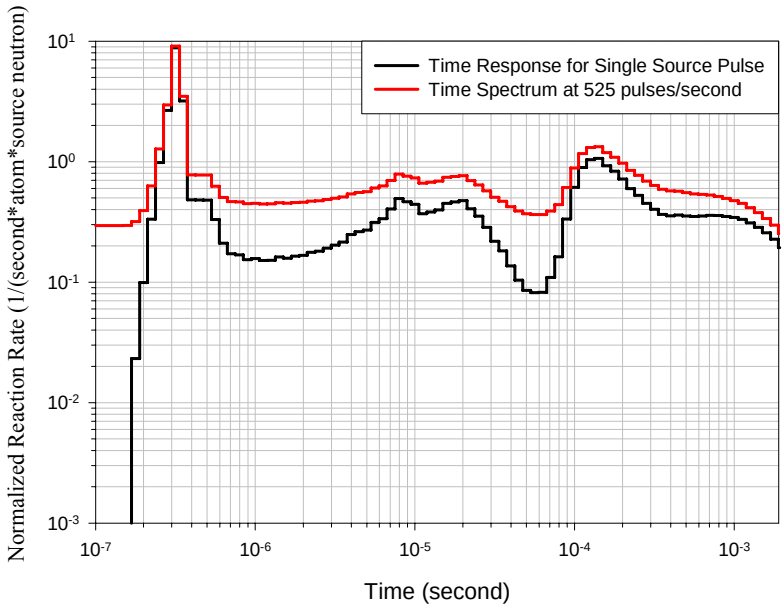

Figure 2-57. Pulse overlap effect at frequency 525 pulses/second on the Pu-239 time spectrum.

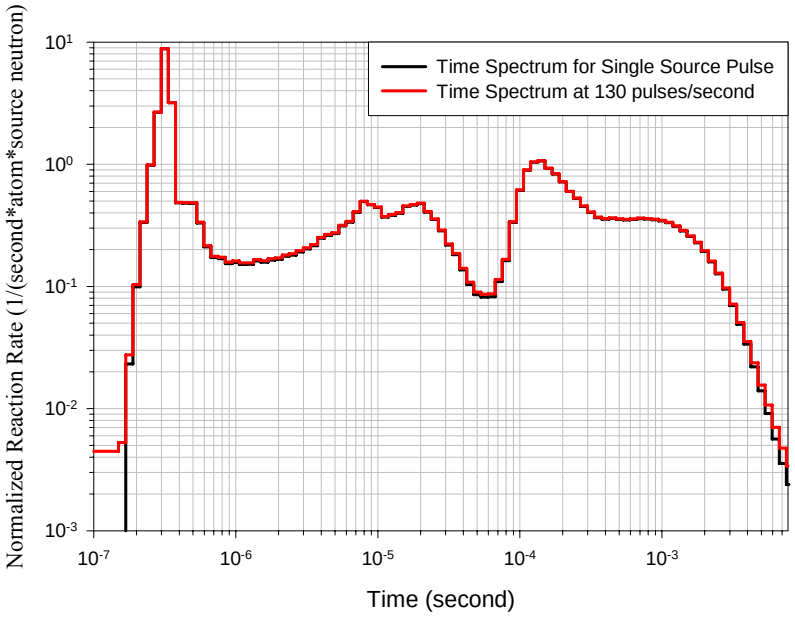

Figure 2-58. Pulse overlap effect at frequency 130 pulses/second on the Pu-239 time spectrum.

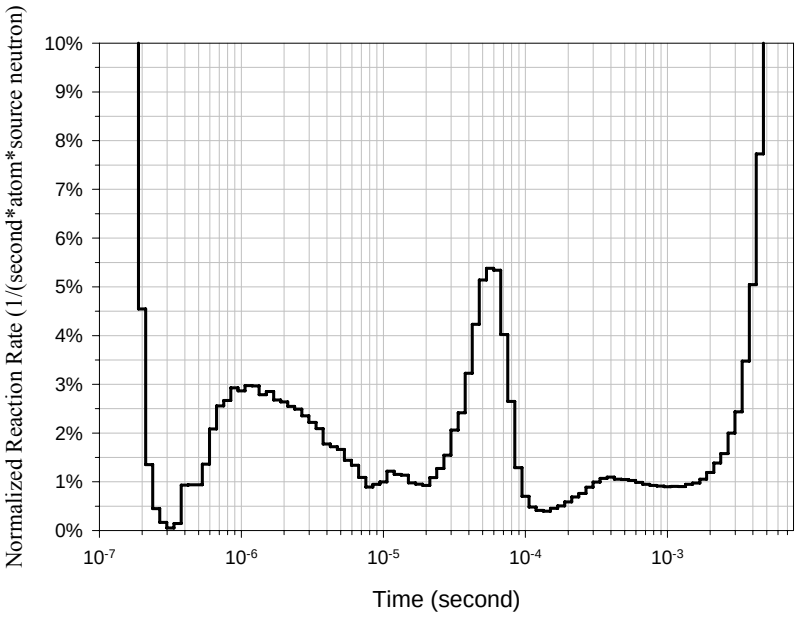

Figure 2-59. Pulse overlap percentage effect at frequency 130 pulses/second on the Pu-239 time spectrum.

2.6 Graphite thermal neutron scattering cross section libraries

The current thermal neutron scattering cross section for graphite was calculated based on the ENDF/ B-VI by using the LEAPR module of NJOY code, which was developed by MacFarlane in 1994[40]. In the case of graphite, the major input data of the LEAPR module is the phonon spectrum which describes the vibration mode of the Carbon atom in the crystalline structure. The graphite phonon spectrum currently used was developed by Young and Koppel in 1965 by fitting their model to the measured data [41]. A discrepancy between the current graphite thermal neutron cross section and the measured data below the Bragg-cutoff energy is shown in Figure 1-4 clearly.

In North Carolina State University, a new phonon spectrum for graphite was developed by using Ab Initio method (i.e. first principle) [42]. A new graphite thermal neutron cross section library, called "NCSU library" [7], was calculated by using NJOY code and based on the new phonon spectrum. Furthermore, to relax the incoherent approximation in the LEAPR module of NJOY code, the inelastic coherent one phonon term has been calculated and implement into the NCSU library, so called "NCSU-1P library" [7]. Figure 2-60 illustrates the total scattering cross sections in the three libraries compared to the measured data. As it can been seen in Figure 2-60, above the Bragg-cutoff energy, all of the three libraries match the experimental data. Below the Bragg-cutoff energy, only the NCSU-1P library [7] can match the Steyrel's measured data. More detail about the cross section below the Bragg-cutoff energy will be discussed in next chapter.

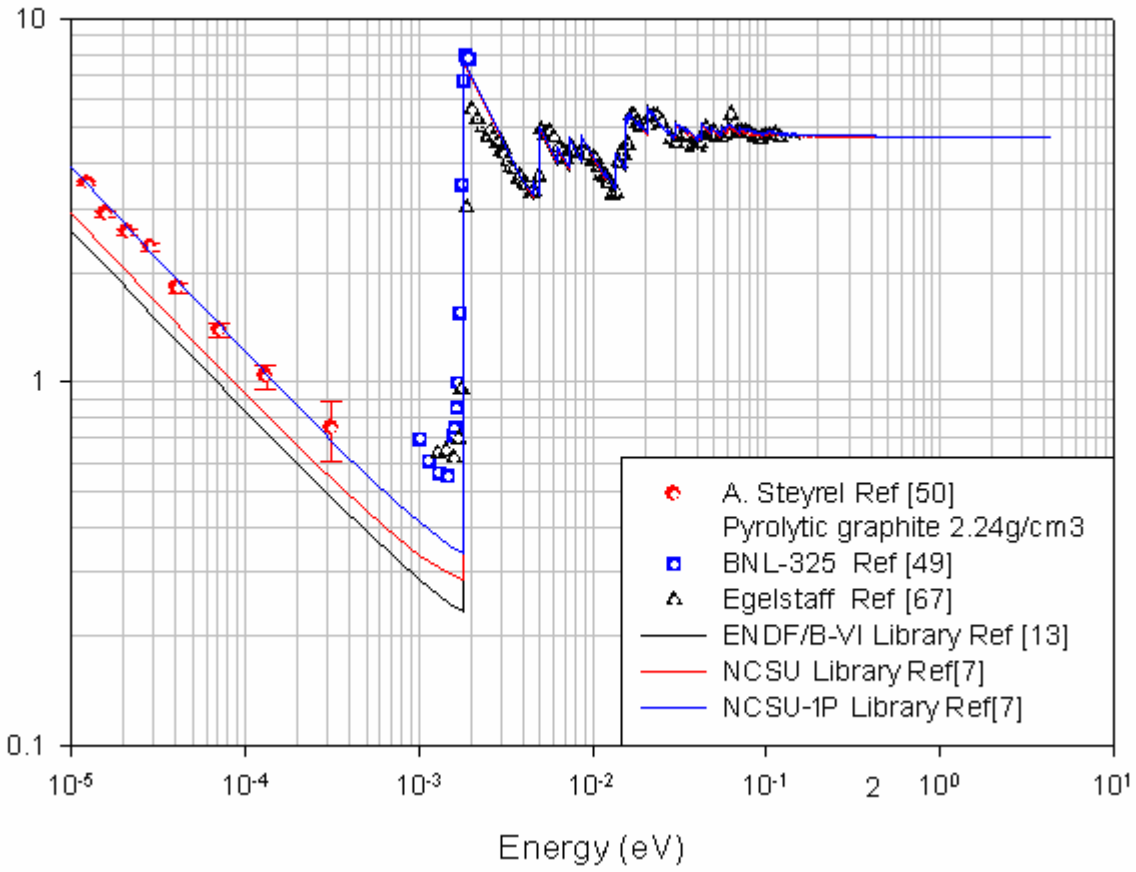

Figure 2-60. Three graphite total scattering cross section libraries compared to the measured data.

When a thermal neutron interacts with graphite atoms, it can be scattered elastically and inelastically, as described in Chapter One. A thermal neutron can be up scattered (gain energy) or down scattered (lose energy) inelastically, while it will keep the original speed when an elastic scattering happens. Although the total scattering cross sections of the three libraries are very close above the Bragg-cutoff energy, the inelastic and elastic cross sections are different, shown in Figure 2-61 and 2-62. And Figure 2-63 illustrates the percentage differences between NCSU, NCSU-1P libraries and ENDF/B-VI library on the inelastic and elastic scattering cross sections,

which are normalized by the total scattering cross section of ENDF/B-VI.

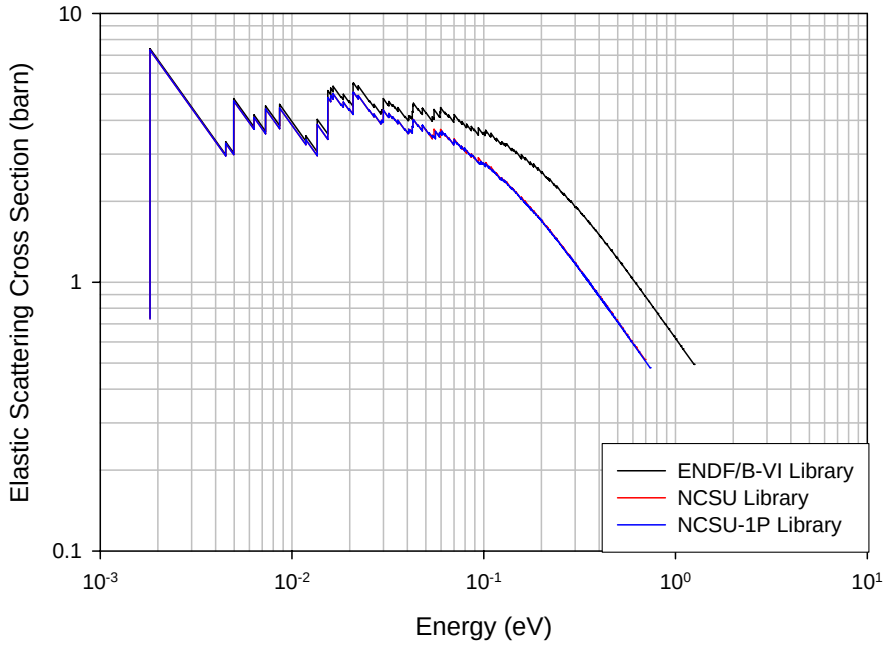

Figure 2-61. Three graphite elastic scattering cross section libraries.

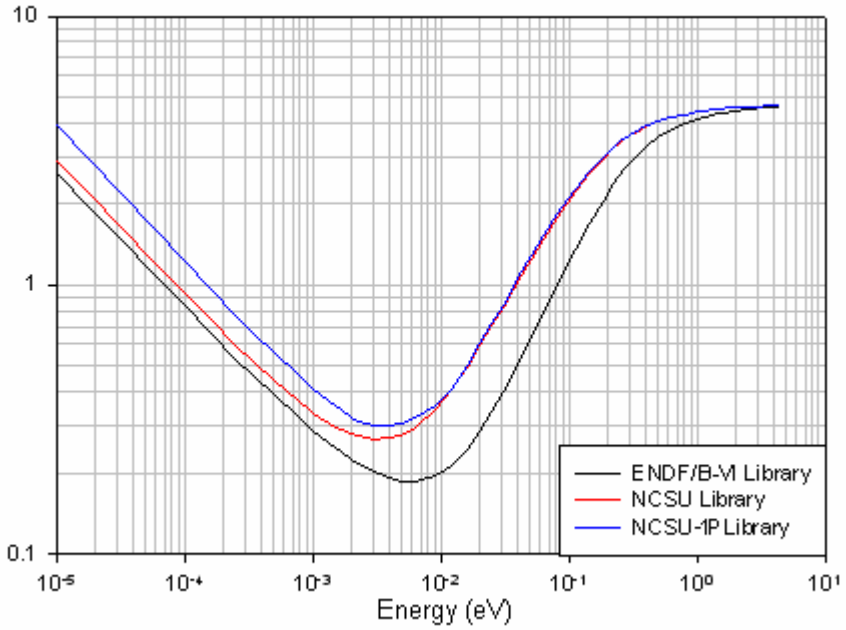

Figure 2-62. Three graphite inelastic scattering cross section libraries.

The time spectra were calculated based on the three different thermal neutron libraries by using the MCNP mode described in Figure 2-3. The percentage differences between the three time spectra are shown in Figure 2-64 and 2-65.

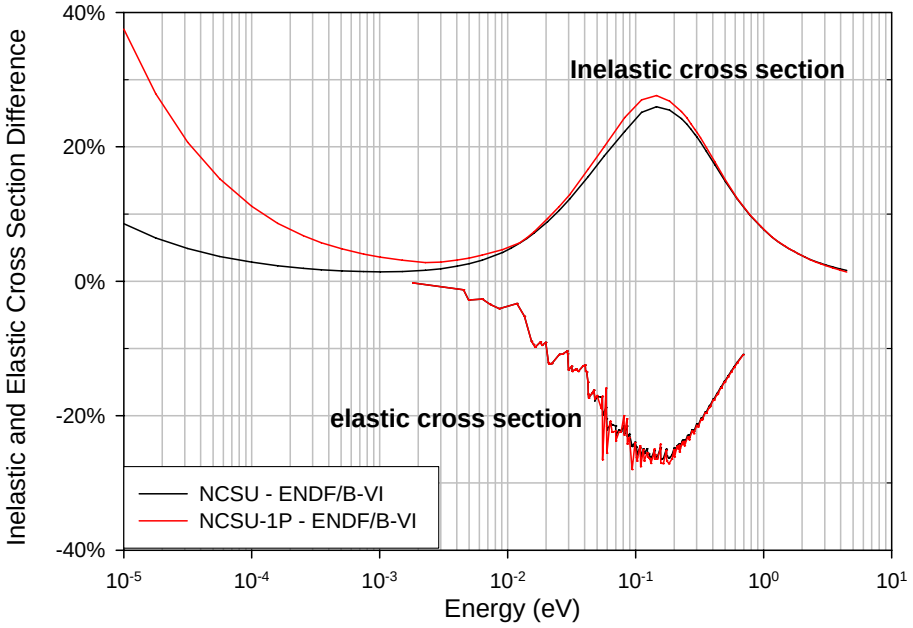

Figure 2-63. The differences between NCSU, NCSU-1P libraries and ENDF/B-VI library on the inelastic and elastic scattering cross sections normalized by the total scattering cross section of ENDF/B-VI.

As it can be seen in Figure 2-64 and 2-65, compared to the ENDF/B-VI library, the NCSU and NCSU-1P libraries [7] give the maximum difference 2% and 3% on the time spectra. To understand the differences on the time spectra, the modified MCNP5 perturbation code was utilized to analyze those results. The perturbation calculations performed so far, which show around 10% differences on the time spectra, were based on the 5% perturbation on the thermal neutron total scattering cross section. Apparently, the total scattering cross sections in the two new libraries are very close to the one in the ENDF/B-VI library and the measured data. That's

because that the differences on the inelastic and elastic cross sections have almost same value but different sign, shown in Figure 2-63.

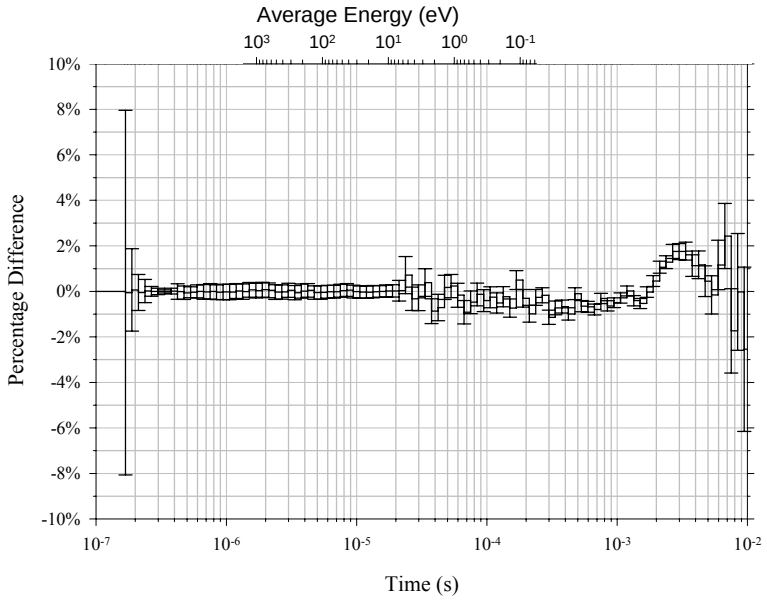

Figure 2-64. Percentage difference between the time spectra based on NCSU and ENDF/B-VI libraries.

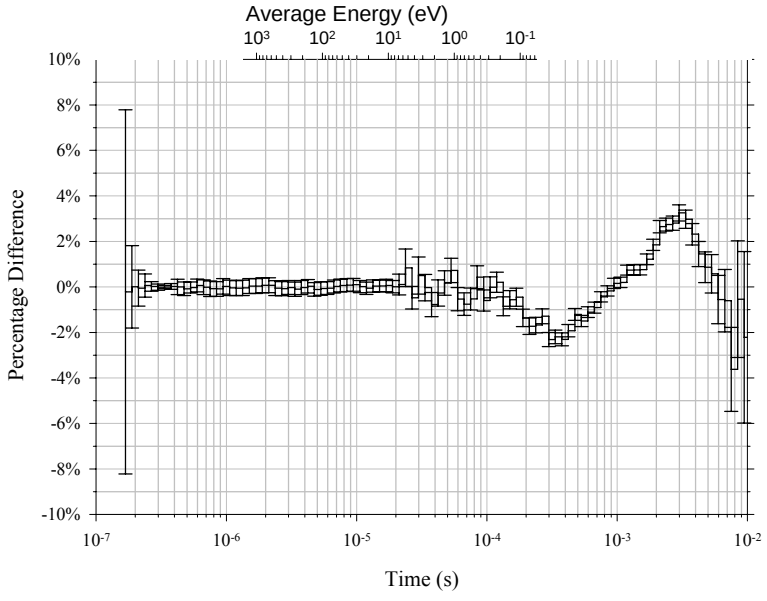

Figure 2-65. Percentage difference between the time spectra based on NCSU-1P [7] and ENDF/B-VI libraries.

Therefore, two perturbation calculations were performed. One is +5% on the inelastic cross section, the other is +5% on the elastic cross section. Figure 2-66 illustrates the results of the two perturbation calculations. As it can be seen, the effect on the time spectrum due to +5% perturbed inelastic cross section is different from the effect due to +5% perturbed elastic cross section. That's because the inelastic scattering allows neutron energy transferred while the elastic scattering does not.

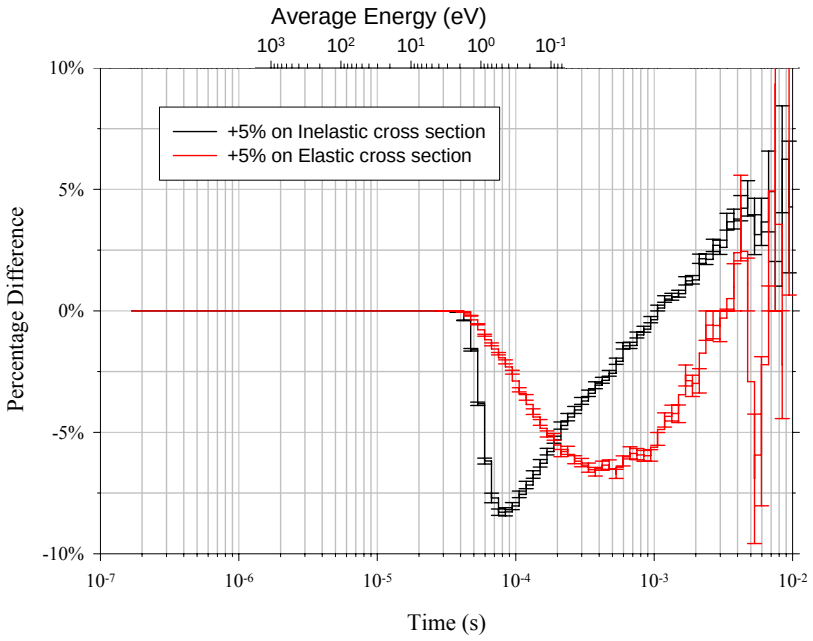

Figure 2-66. Perturbation calculations based on +5% difference on the inelastic and elastic cross section.

The perturbation calculations based on +5% perturbed inelastic cross section and -5% perturbed elastic cross section were combined and shown in Figure 2-67. If assuming the +5% perturbation on inelastic cross section and -5% perturbation on elastic cross section are independent, the combined perturbation calculation shown in Figure 2-67 should give similar result as the percentage differences on time spectra based on the three libraries shown in Figure 2-64 and 2-65.

However, the maximum difference in Figure 2-67 (around 7%) is much bigger than the other two. It can be explained by that the perturbation code does not take the differential inelastic cross sections into consideration, which are different in the three libraries. The differential inelastic cross sections contain the information of the secondary neutron energy distributions and angular distributions.

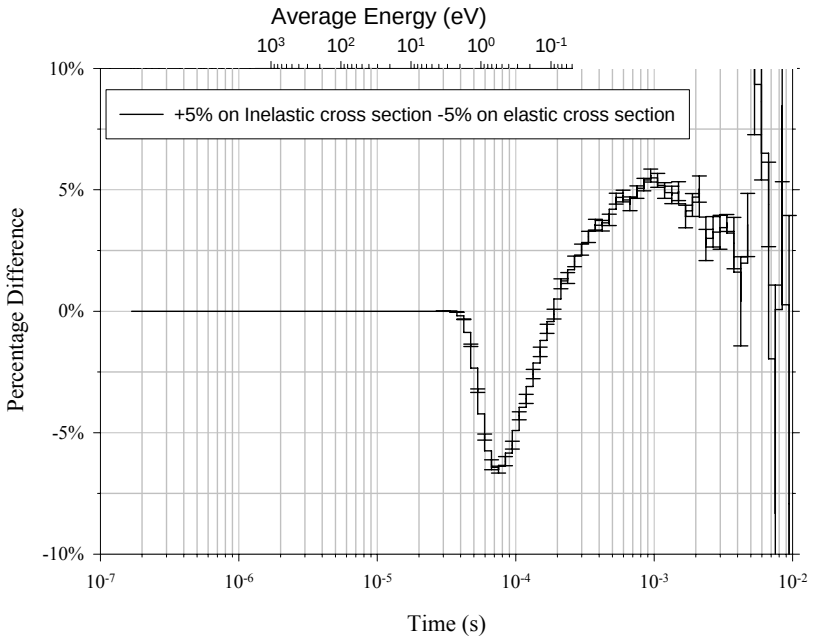

Figure 2-67. Combination of +5% perturbation on inelastic and -5% perturbation on elastic cross section.

An artificial thermal neutron cross section library was made by combining the differential inelastic cross sections in the ENDF/B-VI library and the inelastic and elastic cross sections in the NCSU-1P library [7]. In this way, the only differences between the artificial library and ENDF/B-VI library are the inelastic and elastic cross sections, which can be described by the perturbation calculations. The percentage difference on the time spectra due to those two libraries is shown in Figure 2-68. It can be seen by comparing Figure 2-68 and 2-67, the two curves are

very similar in term of shape and the maximum difference (15%) in Figure 2-68 is larger. That indicates two things. First, the perturbation calculations based on +5% inelastic and -5% elastic cross sections are reasonable if the differential inelastic cross sections are the same. Secondly, the differences in the differential inelastic cross sections can reduce the difference in the time spectra from 15% (Figure 2-68) to 3% (Figure 2-65). Therefore, the differential inelastic cross sections from ENDF/B-VI and NCSU libraries [7] are compared in Figure 2-69, 2-70 and 2-71 for certain incident energies.

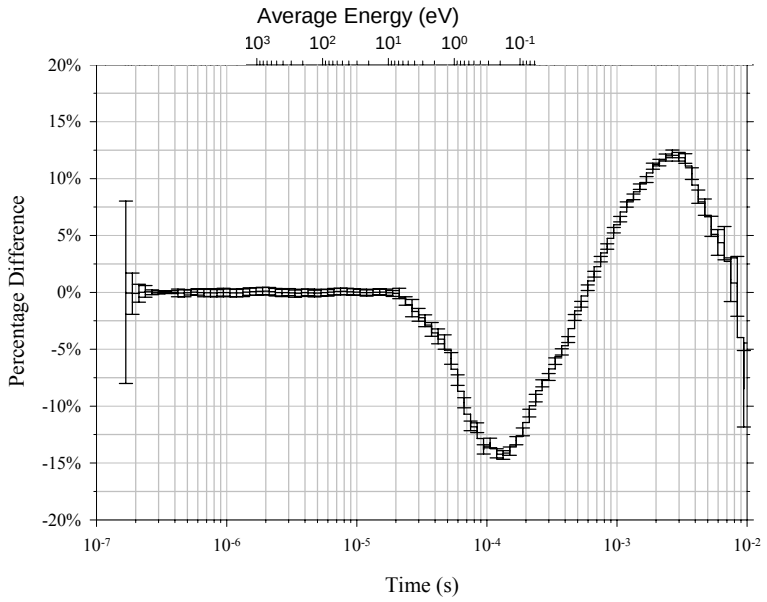

Figure 2-68. Percentage difference between the time spectra based on the artificial and ENDF/B-VI libraries.

As it can be seen in Figure 2-69, 2-70 and 2-71, the two libraries are mainly different by a sharp peak in the NCSU differential cross section, which is located on the energy of incident neutron. The width of this peak (distance between two peak shoulders) is around 0.024eV. This peak gives the probability that the incident neutron is up scattered (gain energy <0.012eV) or down scattered (lose energy <0.012eV).

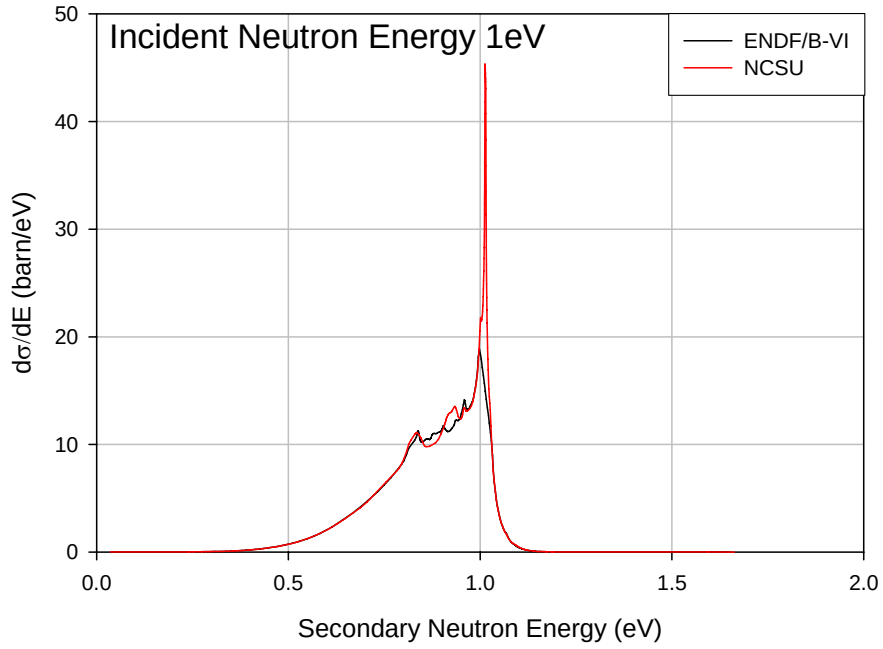

Figure 2-69. Differential inelastic cross sections in ENDF/B-VI and NCSU libraries for 1eV incident neutron.

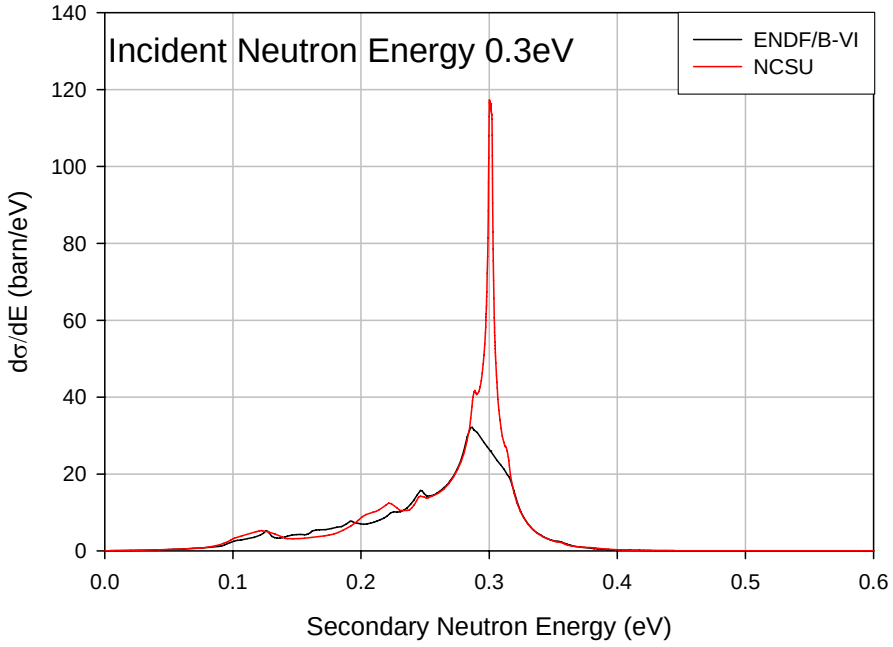

Figure 2-70. Differential inelastic cross sections in ENDF/B-VI and NCSU libraries [7] for 0.3eV incident neutron.

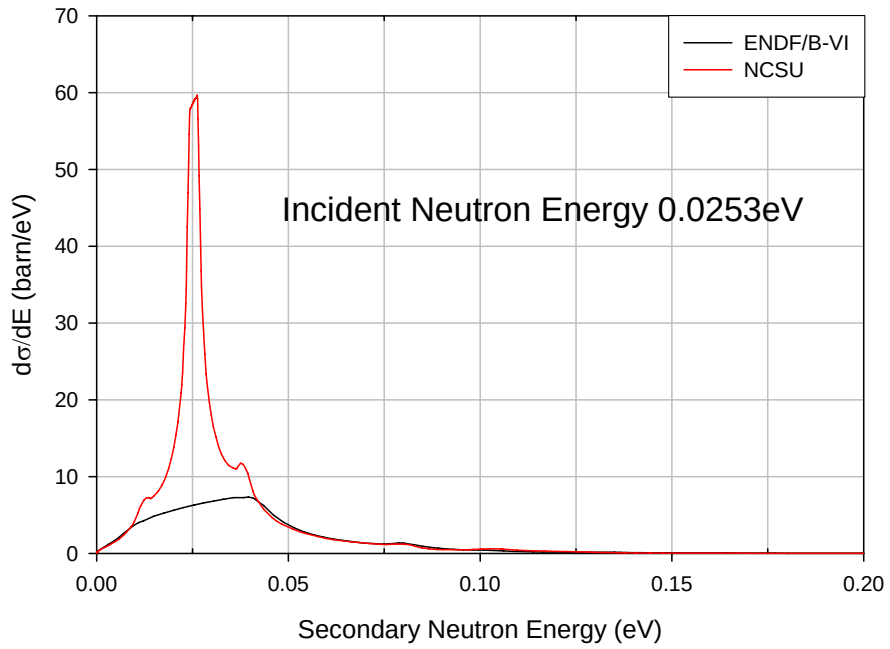

Figure 2-71. Differential inelastic cross sections in ENDF/B-VI and NCSU libraries [7] for 0.0253eV incident neutron.

Due to the limited energy resolution, this small energy transfer (~0.01eV) will not be detected by this Slowing-Down-Time experiment. The inelastic scattering with this small amount of energy transfer is a similar effect to the elastic scattering [43]. Consequently, comparing NCSU [7] and ENDF/B-VI libraries, the effect on the time spectrum due to the higher inelastic cross section will be minimized by the effect due to lower elastic cross section.

The integral of the differential inelastic cross section is equal to the inelastic cross section. In the thermal neutron library, which can be used by MCNP5 code (Acer format), the total area of the differential inelastic cross section is normalized to unit. As a result, in the artificial library we made before, the shape of the differential inelastic cross section is as same as the one in the ENDF/B-VI library but shifted up due to higher inelastic cross section in the NCSU-1P library [7].

Therefore, large energy transfer is allowed in the artificial library which is able to be detected by the Slowing-Down-Time experiment. And it gives a larger difference on the time spectrum (15%) shown in Figure 2-68.

The above analysis indicate that the Slowing-Down-Time experiment, although it's an integral measurement, can provide some information about not only the integral scattering cross section but also the differential scattering cross section, which is difficult to measure directly. So far, the libraries discussed above are the crystalline graphite thermal neutron scattering library. While in the measurement, reactor grade graphite will be utilized. More details about the difference between crystalline graphite and reactor grade graphite are discussed in the next chapter.

Chapter 3 Neutron Transmission Measurements in Graphite

3.1 Method

3.1.1 Theory

A thermal neutron can only gain or lose energy by inelastic scattering with the nuclei of the graphite moderator, while the coherent elastic scattering (known as Bragg elastic scattering) will only change the thermal neutron direction. Therefore, the neutron inelastic scattering cross-section of graphite is important to study the thermal neutron energy spectrum, such as in a thermal reactor case. Nevertheless, the neutron inelastic scattering cross-section is not easy to measure or benchmark in the energy region above the Bragg cutoff, because it is masked by the coherent elastic scattering cross-section ($\sigma_{\text{total}} = \sigma_{\text{elastic}} + \sigma_{\text{inelastic}}$). While below the Bragg cutoff energy (2meV for graphite), coherent elastic reaction is not possible ($\sigma_{\text{elastic}} = 0$). Thus, due to the negligible absorption cross-section of graphite, the total cross-section will be approximately equal to the inelastic cross-section. In addition, when inelastic scattering happens in a crystalline material, the thermal neutron will be scattered by an aggregate of nuclei to create or absorb phonons (i.e. lattice vibration). As a result, the neutron inelastic cross-section is related to the structure of the sample.

In this experiment, the majority of source neutrons have a wavelength of 0.89 nm. And its energy

is $E = \frac{h^2}{2m\lambda^2}$ =1.033meV, which is below the graphite Bragg cutoff energy (2meV), where h is Planck's constant, m is the electron mass and λ is the neutron wavelength. The total neutron cross-section at this energy was measured by performing a transmission experiment. The relation between the transmission and the total cross-section is shown by the well-known equation

$$\sigma_{total} = -\frac{1}{nx}\ln T = \frac{1}{\frac{\rho N_A}{M}x}\ln\frac{I}{I_0} \tag{3.1}$$

Where $n = \frac{\rho N_A}{M}$ is the atomic density; ρ is the mass density; N_A is the Avogadro Constant; M is the atomic mass number; x is the sample thickness; T is the transmission of the sample; I and I_0 are the neutron fluxes at the detector location with and without a sample in the neutron beam.

The measurement of the neutron total (i.e. inelastic) cross section at this energy will be used to compare to the available measured data and benchmark the different thermal neutron cross section libraries of graphite generated by different methodologies. This measurement is complimentary to the ORELA experiment which mainly provides the benchmark data at the energy above the Bragg cutoff energy.

Since the neutron source in this experiment is reflected by a monochromator out of a primary beam [44], all the neutrons which satisfy the Bragg condition (λ, λ/2, λ/3 and so on) will appear in the reflecting beam. There are two methods to measure the total cross-section by using this neutron source. One method is to chop the continuous neutron source into a pulsed neutron source and do a Time-Of-Flight measurement (the TOF transmission method). The neutrons with different wavelength can be separated by the different flight time in the measured time spectrum. The

transmission can be calculated from the ratio between 0.89 nm neutron peak areas of a beam with a sample (I) and an empty beam (I_0). A neutron chopper is needed for this type of measurement. Since a large amount of source neutrons are chopped, the counting rate will be dramatically lower than the measurement without a neutron chopper. The other method is to turn the neutron source into a monoenergetic source as much as possible by using filters to remove the neutrons with the wavelength other than 0.89 nm and perform a transmission measurement without the neutron chopper (the direct transmission measurement method). In the case that the neutron source is not perfectly monoenergetic even with filters, the measured transmission must be corrected later. This type of measurement can have relatively high counting rate, while some systematic error will be introduced by the correction for the neutrons with the wavelength other than 0.89 nm.

In this work, the TOF transmission method required a long measuring time, therefore the direct transmission measurement method was utilized. The source neutron energy spectrum was measured once by using the TOF method and was used to provide necessary information for the correction later. The systematic and statistic error were discussed as well.

3.1.2 Neutron facility and experimental setup

NCNR (NIST Center for Neutron Research) operates a 20MW D_2O-moderated research reactor which is able to provide cold neutron source. Fission neutrons, after being moderated by heavy water to thermal energies, can slow down to cold energies in the ellipsoidal shell of 5 liter of liquid hydrogen maintained at a temperature of 20K [45]. The scattering in liquid hydrogen can cool the neutrons down to around 40K. The cold neutrons exit from the reactor and travel through evacuated rectangular guides (15 cm tall and 6 cm wide, coated with ^{58}Ni) into the experimental

area at the end of the neutron guides 1 to 7 (NG1 to NG7) in the NCNR Guide Hall (Figure 3-1).

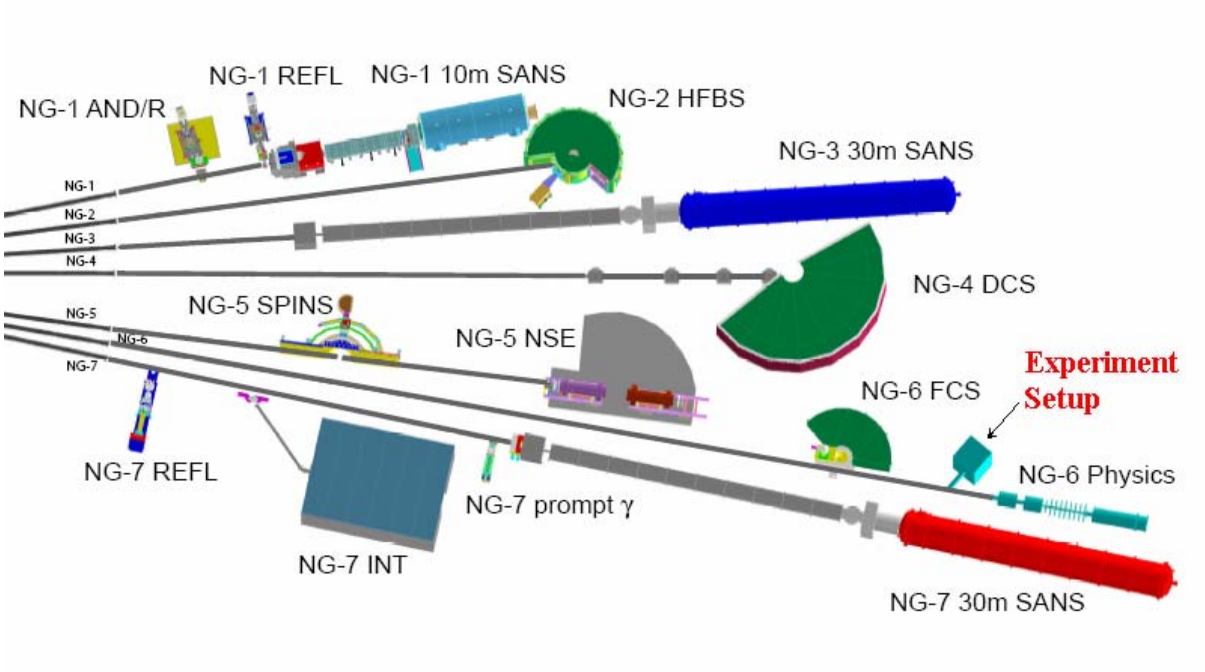

Figure 3-1. NCNR Guide Hall.

There is a 0.89 nm graphite monochromator in the beam at NG-6. The monochromator is constructed from nine tiled pieces of stage 2 potassium intercalated graphite with a mosaic spectacle between 1.1˚ and 2.1˚, reflectivity of 73-91% at 0.89nm, the neutrons with wavelength of 0.89 nm will be diffracted away from the primary beam (NG-6) at the angle of 60° into the experiment setup [46]. Some additional wavelengths are present in the beam beside 0.89 nm, the majority of which are $\lambda/2$=0.445 nm and $\lambda/3$=0.297 nm. The 0.89 nm neutron beam was utilized primarily to produce ultra cold neutrons for the neutron lifetime measurement [46]. In this experiment the 0.89 nm neutron beam was utilized as the neutron source, shown in Figure 3-1.

The neutrons in the beam with other than 0.89 nm wavelength could bring noise into the transmission measurement. In the neutron lifetime measurement, the $\lambda/2$ neutrons were reflected

out of the beam by placing a piece of 10-mm-thick HOPG (highly oriented pyrolytic graphite) with a mosaic spread of 2.2° between the neutron guide and 0.89nm monochromator. Giving the right angle, the HOPG piece (i.e. λ/2 filter) could reduce λ/2 neutrons by a factor more than 7. The reflection neutrons with the order higher than 2 (especially the λ/3 neutrons) were attenuated by a purified polycrystalline bismuth filter, which was placed in a vacuum chamber and cooled down to 90K. The bismuth filter could attenuate the λ/3 neutrons by 76% and the 0.89 nm neutrons by only 5%. [44]

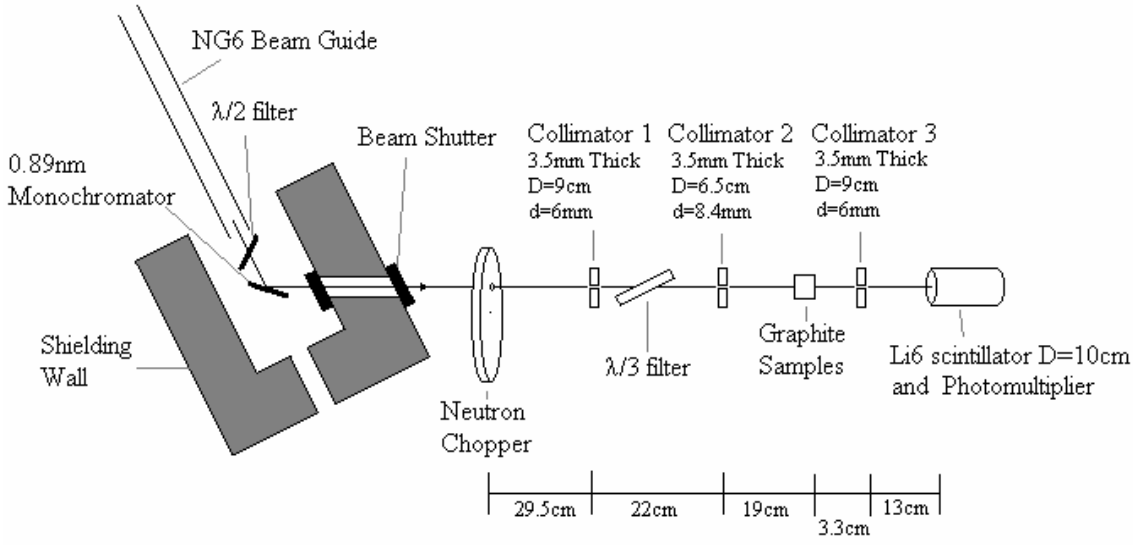

Figure 3-2. Experimental setup.

In this experiment, the λ/2 filter remained as shown in Figure 3-2. However, to simplify the experimental setup and keep the 0.89 nm source neutrons intact, the bismuth filter, the vacuum chamber and the cooling system were remove from the beam. Instead, another piece of HOPG (i.e. λ/3 filter) with 12.5 mm thickness was placed in the neutron path lane shown in Figure 3-2 to reduce most of the λ/3 neutrons. The angle between the beam and the λ/3 filter was optimized to give the maximum attenuation to the λ/3 neutrons.

The neutron energy spectrum of the beam can be obtained from the Time-Of-Flight measurement. Therefore, a neutron chopper with frequency 60Hz was placed right after the neutron beam shutter and before the λ/3 filter, shown in Figure 3-2, to chop the continuous neutron source into a pulsed neutron source. The TOF measurement can be performed with the chopper running. When the chopper was stopped and the aperture was lined up to the beam, the direct neutron transmission can be measured. There was a sample holder after the chopper and λ/3 filter. A Li-6 scintillation detector with a diameter around 10cm and a photomultiplier tube resided at the end. Three Li-6 collimators were placed between the chopper, λ/3 filter, sample holder and detector, shown in Figure 3-2.

3.1.3 Data acquisition instrumentation

A lithium 6 scintillator was used as the neutron detector. Its effective volume is 10 cm diameter and it is 1~2 mm thick. The low energy neutrons (meV range) can be stopped completely within this thickness in the scintillator. The detector was hooked up with a photomultiplier tube, on which a 1700V high voltage was applied. The signal from the photomultiplier, after a preamplifier, was amplified by an amplifier and went into a timing Single Channel Analyzer (SCA). The lower window of the timing SCA is set to eliminate most of the gamma background. After the timing SCA, the signal went to the Multi-Channel Scaler (MCS) computer. In the Time-Of-Flight measurement, the channel width in the MCS was set to be 4μs and the total channel number was set to be 4096. A typical measurement time of TOF varied from 7 to 12 hours. In the direct transmission measurement, the MCS worked as a counter. The channel width was set to be 1 second and the total channel number was set to be 600. The sweep number was set to be 1, which means 1x600=600 seconds measuring time. Since the typical counting rate

without the samples is about $7.5x10^3$ counts/second, enough counts can be collected within the 600 seconds measurement time.

3.1.4 Measurement samples

Alloy 6061 Aluminum samples were measured in this transmission experiment. Since the neutron total cross-sections of aluminum in the low energy region are well known, the measured total cross-section can be compared with the reference value and indicate whether the measurement and correction are proper or not. Two types of graphite samples were also measured in this experiment. The detail specifications of the samples are shown in Table 3-1.

Table 3-1. The samples used in the transmission measurement

Sample	Density (g/cm^3)	Thickness (inch)	Manufacturer info
aluminum	2.7	3/8	Alloy 6061
reactor grade graphite	1.66	1/4	
pyrolytic graphite	2.2	1/8	GE Advanced Materials

An X-ray diffraction experiment was performed using a pyrolytic graphite sample and a reactor grade graphite sample to examine the structure of the crystal graphite in the two samples. The diffraction measurement is shown in Figure 3-3. The radiation source is Cu Kα X-ray with wavelength of 1.542 Å. The samples were fixed in the holder, the detector was rotated, and diffraction X-ray was counted. The primary diffraction peak (corresponding to the family of planes 002) in Figure 3-3 happened at $2\theta=26.08°$ and $2\theta=26.4°$ for pyrolytic graphite and reactor grade graphite respectively. The distance between graphite layers can be calculated from equation (3.2), which is equal to 6.8Å for the two samples. Therefore, the measurements indicate that the crystalline graphite in pyrolytic graphite sample and reactor grade graphite sample has the

same structures.

$$c = 2d = 2\frac{\lambda}{2\sin\theta} = \frac{\lambda}{\sin\theta} \tag{3.2}$$

However, as mentioned in Chapter 1, it is known that reactor grade graphite contains a second phase of carbon that does not have the regular crystalline structure.

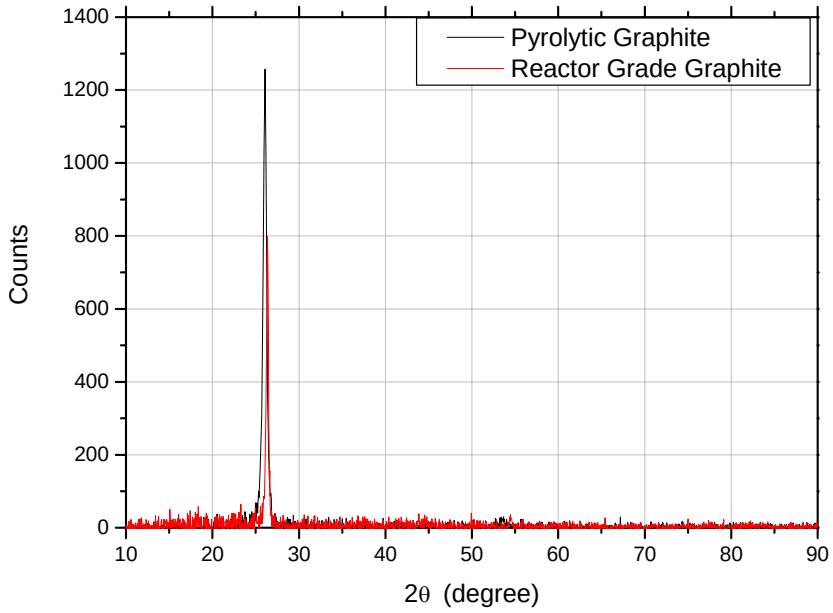

Figure 3-3. X-ray diffraction measurement using pyrolytic graphite and reactor grade graphite samples.

3.2 Data analysis

3.2.1 Typical corrections

3.2.1.1 Detector efficiencies for neutrons with different wavelengths

Neutron absorption cross sections of Li-6 for the λ=0.89 nm, λ/2 and λ/3 neutrons are 370, 180 and

120 barns respectively. The lithium glass in the detector is 2mm thick. The density of the lithium glass is around 2.5 g/cm^3. And the weight percentage of Li-6 in the lithium glass is around 5%. Thus the probabilities of neutron absorption in the detector can be calculated, which are 99.99%, 99.98% and 99.7% for the λ=0.89nm, $\lambda/2$ and $\lambda/3$ neutrons respectively. Therefore, one can say almost all the neutrons enter the detector will be absorbed in the lithium glass and the detector efficiencies for neutrons with different wavelengths are almost equal.

3.2.1.2 Experiment scheme and I_0

The neutron flux without samples in the beam (I_{01}) was measured first. Then one piece of sample was placed into the beam and the neutron flux (I_1) was measured. After that, another neutron flux without samples (I_{01}) was measured, followed by the two pieces of samples (I_2) measurement. After the measurement of four pieces of samples (I_4), the last I_{05} was measured and followed by the background measurement (I_B) with a 1/8" lithium filter in the beam to stop all the source neutrons. The background was subtracted from all the measured neutron fluxes.

Measurements were taken for Al, pyrolytic graphite and reactor grade graphite samples by using setup 1 (shown in Figure 3-2) continuously. The neutron flux without samples was measured five times at different moments for each type of sample. Therefore, in order to study the fluctuation of the neutron source, an I_0 profile can be made by putting all I_0 measurements at different moment together as shown in Figure 3-4. Measurements were also taken by using setup 2 (shown in Figure 3-21, mentioned in section 3.4.2) for samples of pyrolytic graphite and reactor grade graphite. The I_0 profile of experiment setup 2 is shown in Figure 3-5. As it can be seen in Figure 3-4 and 3-5, the fluctuation of I_0 can be significant.

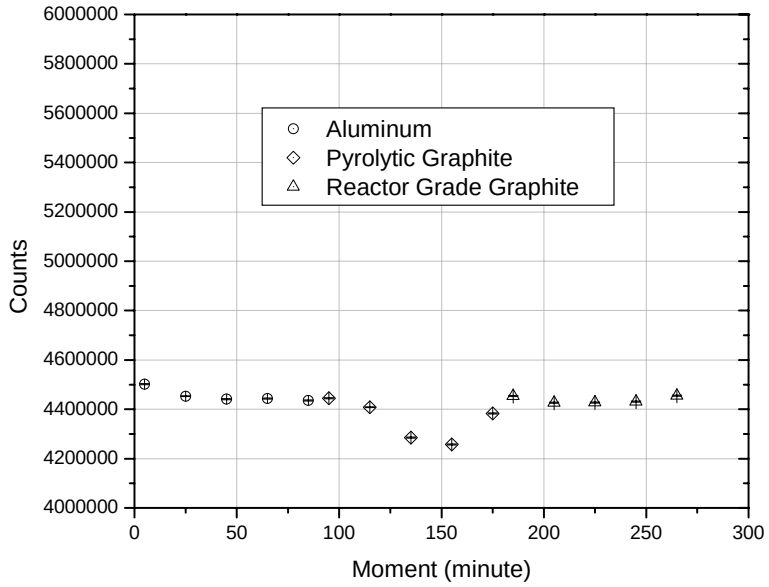

Figure 3-4. I_0 profile for experiment setup 1 measurements.

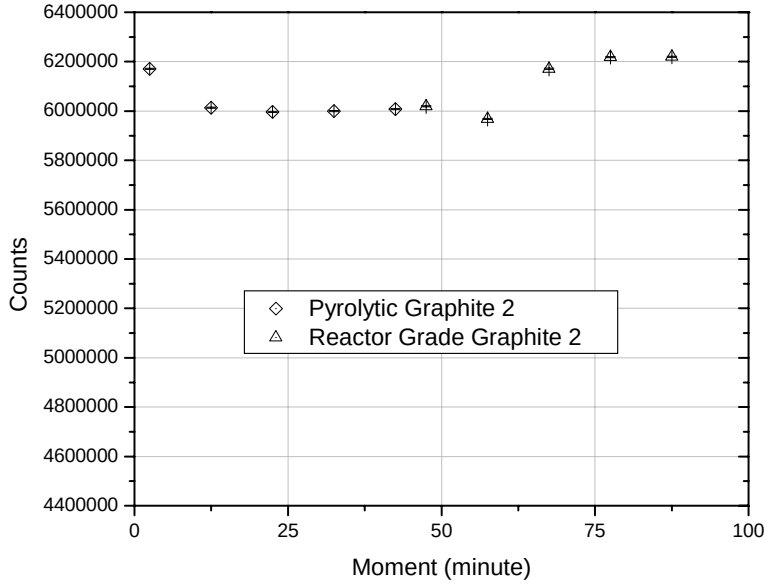

Figure 3-5. I_0 profile for experiment setup 2 measurements.

Since it's impossible to measure the true I_0 at the same moment when measuring a neutron flux with sample on the beam, the true I_0 corresponding to a certain sample measurement was estimated based on the I_0 profile. Furthermore, every sample measurement was taken place between two I_0 measurements. If the 5 times I_0 measurements are close to each other, the average value of them will be used to estimate the true I_0. The sample of Al and reactor grade graphite in setup1 fall into this catalog. If the fluctuation of five I_0 measurements is significant (the cases of pyrolytic graphite in experiment setup 1 and reactor grade graphite in experiment setup 2), one can not get a single estimate I_0 for all the sample measurements I_1, I_2, I_3, and I_4. In stead by assuming the neutron source intensity varies linearly, the true I_0 for the I_1 measurement can be estimated by the average of I_0 measurement before I_1 and one after ($\frac{I_{01} + I_{02}}{2}$). There is a special case of pyrolytic graphite in experiment setup 2, in which the first I_0 measurement (I_{01}) is way higher while the other 4 I_0 measurements are almost equal. In this case the first I_0 measurement (I_{01}) and the sample measurement I_1 were abandoned. The average value of the last four I_0 measurements was used to estimate the true I_0 for sample measurements I_2, I_3, and I_4. In this way, the estimated I_0s were used to normalize I_1, I_2, I_3, and I_4 and the transmission T_1, T_2, T_3, and T_4 were calculated. In addition, the statistical error and the fluctuation were both considered as errors for the estimated I_0s.

3.2.1.3 Detector dead time

The dead time of the Li-6 scintillation detector is in the order of 10^{-6} second [47]. Considering the typical counting rate (7.5×10^3 counts/second) in the measurements, the detector dead time will not have a big effect on the measurement. Therefore, no correction had been made for the detector dead time effect.

3.2.1.4 Non-0.89 nm neutron correction

By using the experimental setup described previously, the Time-Of-Flight neutron spectrum was measured for 12 hours without any samples in the beam, shown in Figure 3-6. As it can be seen, the neutron source is not a perfect monoenergetic source even after introducing and optimizing the λ/2 and λ/3 filters. It can be found that the neutrons in the 0.89 nm peak are about 85-90% of the total neutrons in the spectrum. To keep the source neutrons intact, no effort other than the λ/2 and λ/3 filters was made to remove non-0.89 nm neutrons from the beam further.

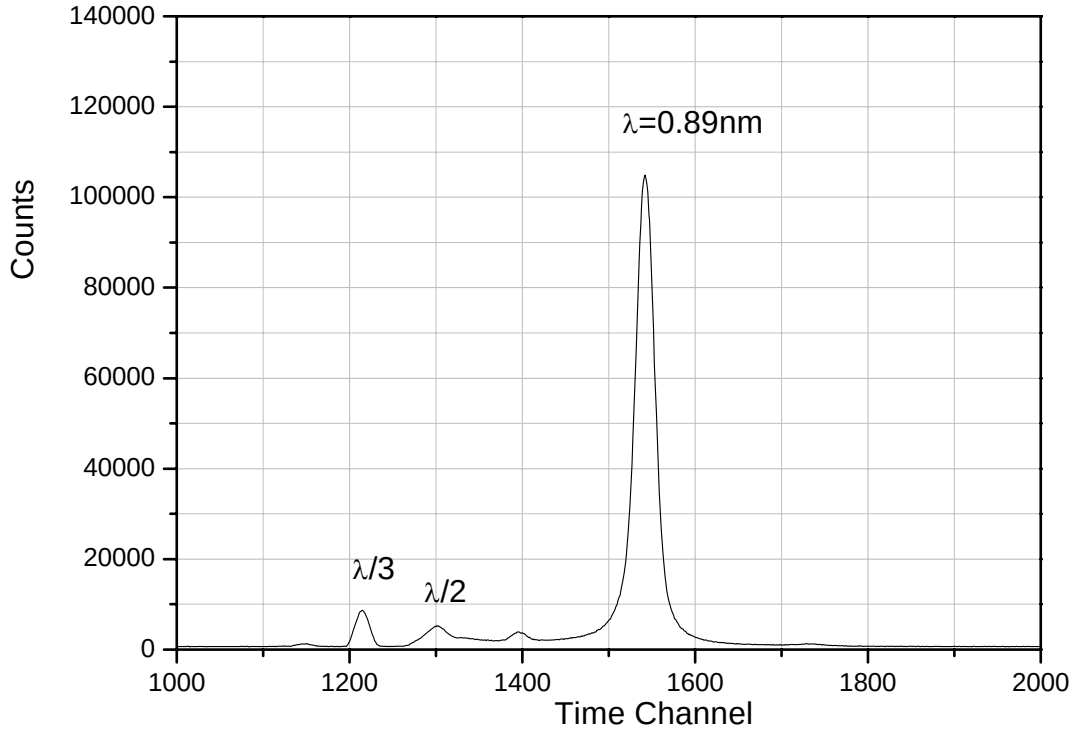

Figure 3-6. Neutron spectrum after 12 hours Time-Of-Flight measurement without sample.

A fitting program, called PeakFit version 4.12, was used to analyze the TOF measurement

spectrum as shown in Figure 3-7 and 3-8. As it can be seen in Figure 3-7, there are 7 peaks in the spectrum, two of which are very small (peak at the time channel 1147.5 and 1732.4) and ignored in this analysis. The Gaussian-Lorentzian Cross Product (Amplitude) function (equation 3.3), which is an approximation of the Voigt function, was chosen to fit these 7 peaks. The Voigt function was used to fit the X-ray diffraction spectrum in the past [48].

$$y = \frac{a_0}{1 + a_3\left(\frac{x - a_1}{a_2}\right)^2 \exp\left[(1 - a_3)\frac{1}{2}\left(\frac{x - a_1}{a_2}\right)^2\right]} \tag{3.3}$$

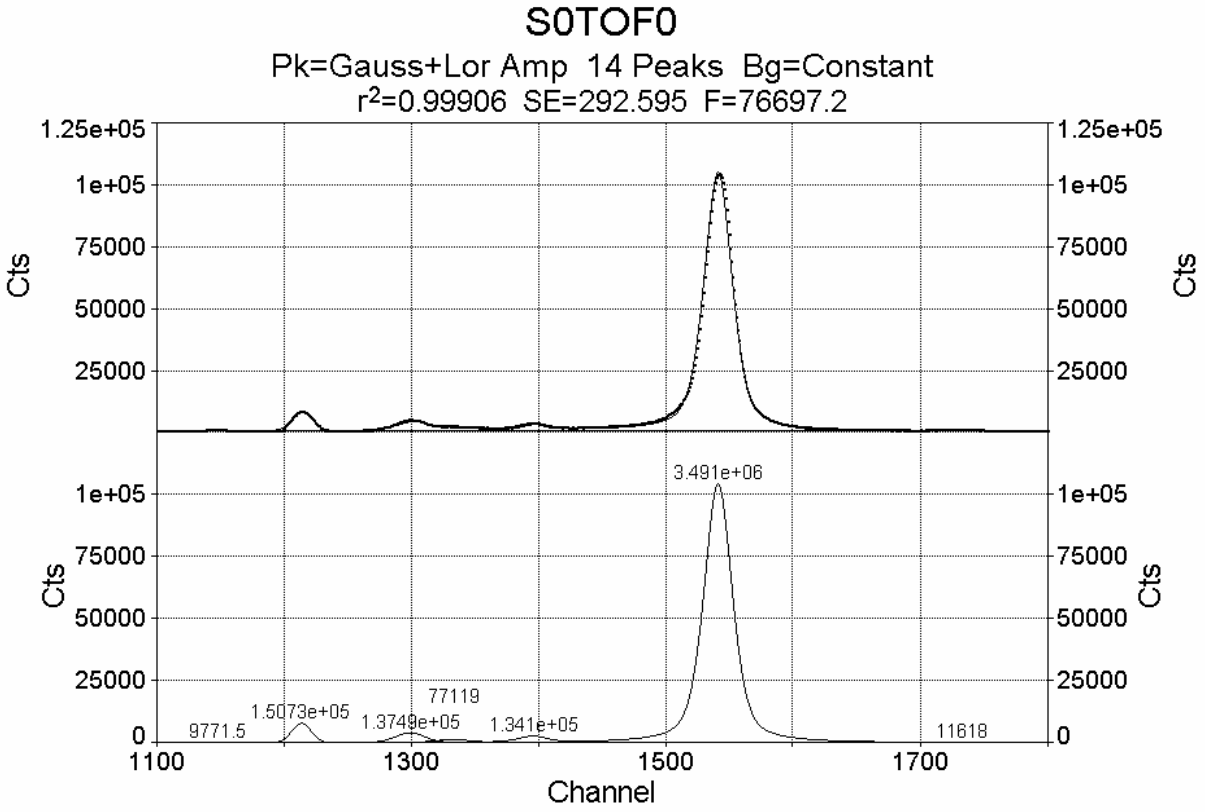

Figure 3-7. Fit to the TOF spectrum by using fitting program PeakFit v4.12. The upper figure is the comparison between the fitting (solid line) and the measurement (black dot), which shows a good agreement. The lower figure shows fitting line only with the net area under each peak.

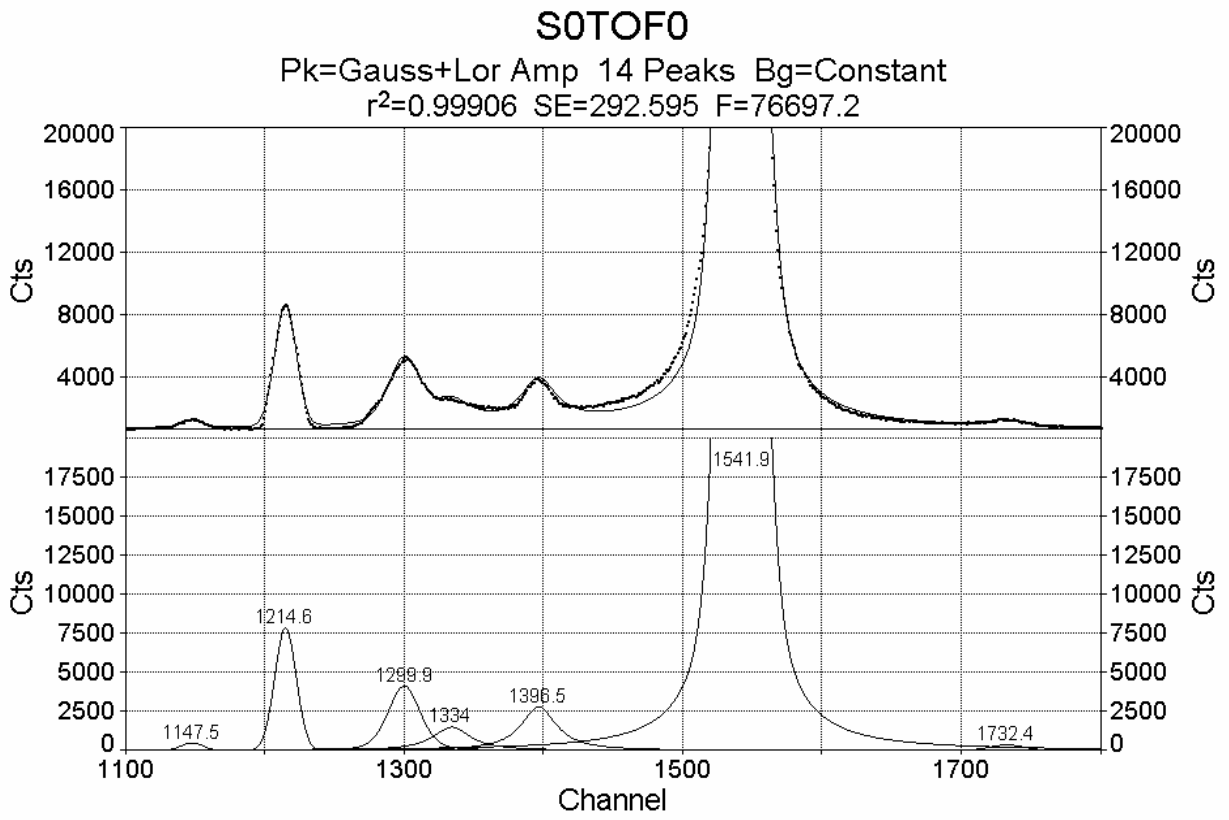

Figure 3-8. Zoom-in of the Figure 3-7. The lower figure shows channel numbers of each peak.

In the PeakFit program, the background was fitted by a constant. The square of the correlation between the TOF spectrum and the fitting curve r^2 had a value of 0.99906, which is very close to 1. Three of the 7 peaks in the TOF spectrum are known as λ, λ/2 and λ/3. Equation (3.4) was used to calibrate the neutron energy vs. flight time, where a and t_0 are fitting parameters. The three data points λ, λ/2 and λ/3 was fitted by equation (3.4) and then the neutron energy of the other peaks can be predicted by the fitting function, as shown in Figure 3-9.

$$E = \frac{1}{2}mv^2 = \frac{1}{2}m\left(\frac{d}{t - t_0}\right)^2 = \frac{a}{(t - t_0)^2} \tag{3.4}$$

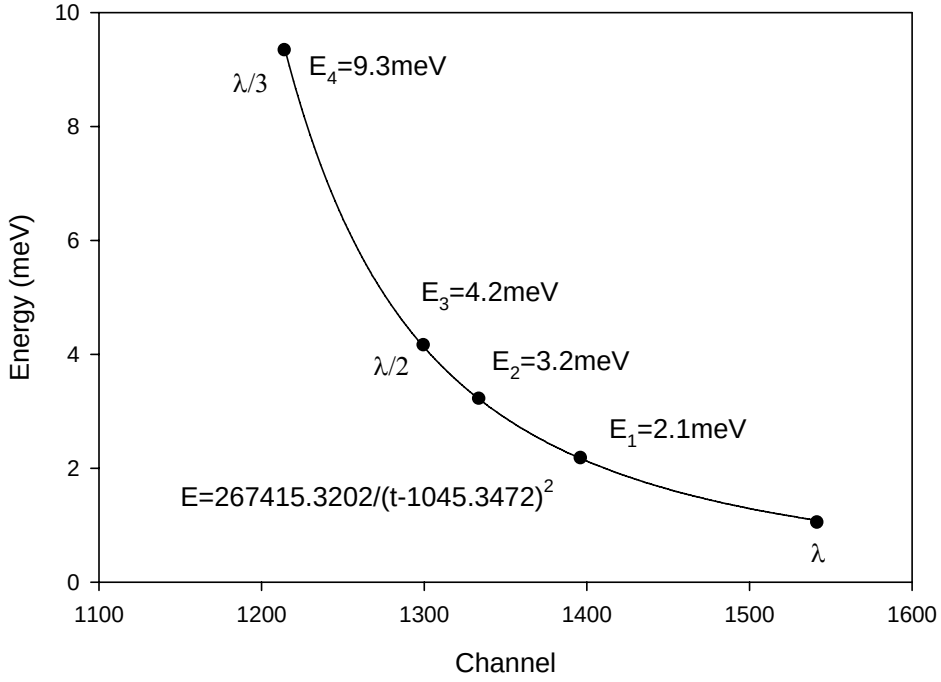

Figure 3-9. Calibration of the flight time and channel number.

After knowing the energies of the non-0.89nm neutrons in the beam, the total cross-sections can be tabulated from the available reference and were defined as $\Sigma_{E1}, \Sigma_{E2}, \Sigma_{E3}, \Sigma_{E4}$. The neutrons which peak at the timing channel 1214.6, 1299.9, 1334 and 1396.5 (Figure 3-8) are corresponding to E1, E2, E3 and E4 respectively. Based on the net peak area, the percentages of the neutrons with different energies can be calculated and defined as $P_{E1}, P_{E2}, P_{E3}, P_{E4}$. When measuring an empty beam I_0 (without samples), the counts corresponding to the λ=0.89nm neutrons can be corrected by using the functions:

$$I_0^{\lambda} = I_0 \times P_{\lambda} \tag{3.5}$$

Where P_{λ} is the percentage of the λ=0.89 nm neutrons in the beam. Define I is the measured counts after putting samples in the beam, in which the counts corresponding to the λ=0.89 nm

neutrons (I^{λ}) can be corrected as:

$$I^{\lambda} = I - I_0 \times \sum_{i=1}^{4} P_{Ei} \exp(-\Sigma_{Ei} x) \tag{3.6}$$

The corrected I^{λ} and I_0^{λ} were used to calculate the total microscopic cross section of the λ=0.89 nm neutrons.

3.2.2 Least Square Fitting

In the well-known transmission formula

$$T = \frac{I}{I_0} = e^{-\frac{\rho \cdot N_A}{M}\sigma \cdot x} \tag{3.7}$$

The known parameters are ρ, N_A and M and there are four sets of data of I/I_0 and thickness x measured in this experiment for each type of samples. After rearranging the formula, one can get

$$\ln(\frac{I_0}{I}) = \sigma \cdot \frac{\rho \cdot N_A}{M} \cdot x \tag{3.8}$$

Define

$$Y = \ln(\frac{I_0}{I}) \tag{3.9}$$

$$X = \frac{\rho \cdot N_A}{M} \cdot x \tag{3.10}$$

Then equation (3.8) can be rewritten as

$$Y=\sigma X \tag{3.11}$$

It becomes a simple linear fitting problem with four sets of data of Y and X, which can be solved by Least Squares Fitting.

Assume the linear system of fitting is

$$Y(X) = a + bX \tag{3.12}$$

The equation (3.12) is different from equation (3.11) by a fitting parameter "a". If the estimated I_0 is exactly equal to the real I_0, the parameter a will be zero. In the real case, the estimated I_0 is statistically equal to the real I_0. That means the expected value of parameter "a" should be very small and could be equal to zero within the error bar.

Assume the values of X are fixed and the values of Y have deviations. This assumption can stand for this experiment, because the x and ρ in $X = \frac{\rho \cdot N_A}{M} \cdot x$ can be measured very precisely by digital scale and caliper, for example for the reactor graphite x=0.635±0.0001cm and ρ=1.66583±0.00004g/cm^3, and N_A and M are the known constant. While the deviation of $Y = \ln(\frac{I_0}{I})$ comes from the statistic in the measurement, in which the deviations of I_0 and I are around 1% to 5% depending on the measuring time and the counting rate.

Define χ^2 as follow:

$$\chi^2 \equiv \sum \left[\frac{Y_i - Y(X_i)}{\sigma_i} \right]^2 = \sum \left[\frac{Y_i - a - bX_i}{\sigma_i} \right]^2 \qquad (3.13)$$

In which the σ_i is the deviation of Y_i. The parameters a and b can be found by minimizing χ^2 [49].

3.2.3 Error of Y

Due to the uncertainty of the reference cross section value, the non-0.89nm neutron correction will bring error to the result. Unfortunately, the available measured total cross-sections of graphite were not accompanied with the uncertainty. To be conservative, it was assume that the uncertainties on the referent total cross-section are 10% for aluminum and 20% for graphite, $\frac{\sigma_\Sigma}{\Sigma}$=10% or 20%.

After correction, one can get

$$Y = \ln(\frac{I_0^{\lambda}}{I^{\lambda}}) = \ln\left(\frac{I_0 \times P_{\lambda}}{I - I_0 \times \sum_{i=1}^{4} P_{Ei} \exp(-\Sigma_{Ei} x)}\right) \tag{3.14}$$

In which, I and I_0 are measured by the Li-6 detector and satisfy the Poisson distribution, the deviation is $\sigma = \sqrt{I}$. Therefore, one can get

$$\sigma_Y^2 = \left(\frac{\partial Y}{\partial I}\right)^2 \sigma_I^2 + \left(\frac{\partial Y}{\partial I_0}\right)^2 \sigma_{I_0}^2 + \sum_{i=1}^{4}\left[\left(\frac{\partial Y}{\partial \Sigma_{Ei}}\right)^2 \sigma_{Ei}^2\right] \tag{3.15}$$

Then

$$\sigma_Y^2 = \frac{\sigma_I^2}{\left(I^{\lambda}\right)^2} + \left(\frac{I}{I_0 \cdot I^{\lambda}}\right)^2 \sigma_{I_0}^2 + \left[\frac{x\left(I - I^{\lambda}\right)}{I^{\lambda}}\right]^2 \cdot \sum_{i=1}^{4} \sigma_{Ei}^2 \tag{3.16}$$

Therefore, the linear fitting coefficients a, which is the total cross-section value, and its deviation σ_a can be obtained as discussed above.

3.3 Control sample – Aluminum

The reference aluminum cross sections, which are from BNL data [50] are shown in Table 3-2. The measurement data were corrected by using the methodology described in the previous section, and shown in Table 3-3. After the Least Square Fitting, the aluminum total cross-section for the 0.89 nm neutron was calculated to be 1.41 ±0.02barns, which is shown in Figure 3-10. It is consistent to the BNL value 1.44barns [50] by considering the uncertainty on the BNL data. Therefore, this methodology to measure the neutron total cross-section is reasonable, and was utilized for the graphite sample.

Table 3-2. Reference aluminum total cross section

	E1	E2	E3	E4
Energy (meV)	2.1	3.2	4.2	9.3
σ (barn)	1.03	0.88	1.51	1.61
Σ_E (cm^{-1})	0.062027	0.052994	0.090932	0.096713

Table 3-3. The measurement of aluminum samples

	One piece of sample	Two piece of samples	Three piece of samples	Four piece of samples
$X = \frac{\rho \cdot N_A}{M} \cdot x$ ($barn^{-1}$)	0.0581123	0.1162246	0.1743369	0.2324492
$Y = \ln(\frac{I_0^\lambda}{I^\lambda})$	7.673731E-02	1.611062E-01	2.404401E-01	3.207012E-01
σ_Y	2.7645E-03	3.4327E-03	4.3073E-03	5.2869E-03

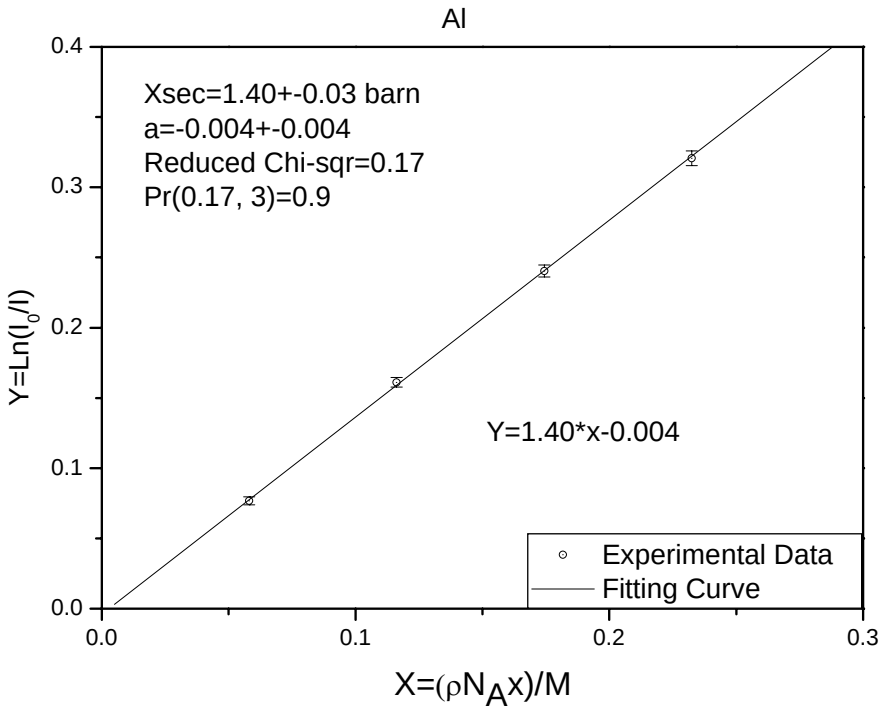

Figure 3-10. The fitted aluminum total cross section for the 0.89 nm neutron.

3.4 Graphite sample

3.4.1 Measurements

The reference total cross sections $\Sigma_{E1}, \Sigma_{E2}, \Sigma_{E3}, \Sigma_{E4}$ are from BNL data [50] and shown in Table 3-4, which were used in this calculation.

Table 3-4. Reference graphite total cross section

	E1	E2	E3	E4
Energy (meV)	2.1	3.2	4.2	9.3
σ (barn)	7.0	4.8	3.7	4.7
Pyrolytic Graphite Σ_E (cm^{-1})	0.772823	0.529936	0.408492	0.518896
Reactor Grade Graphite Σ_E (cm^{-1})	0.5851784	0.4012652	0.3093086	0.3929055

Measurements were taken by using the different type of graphite samples. The experimental setup was the same as aluminum sample measurements. The measured data are shown in Table 3-5 and 3-6, followed by the fitting curve Figure 3-11 and 3-12 for the pyrolytic graphite and reactor grade graphite samples respectively.

Table 3-5. The measurement of pyrolytic graphite samples

	One piece of sample	Two piece of samples	Three piece of samples	Four piece of samples
$X = \frac{\rho \cdot N_A}{M} \cdot x$ ($barn^{-1}$)	0.070768537	0.141537073	0.213520047	0.28649665
$Y = \ln(\frac{I_0^\lambda}{I^\lambda})$	4.986817E-02	6.603341E-02	1.212635E-01	1.759433E-01
σ_Y	3.8859E-03	5.3772E-03	5.9341E-03	5.8939E-03

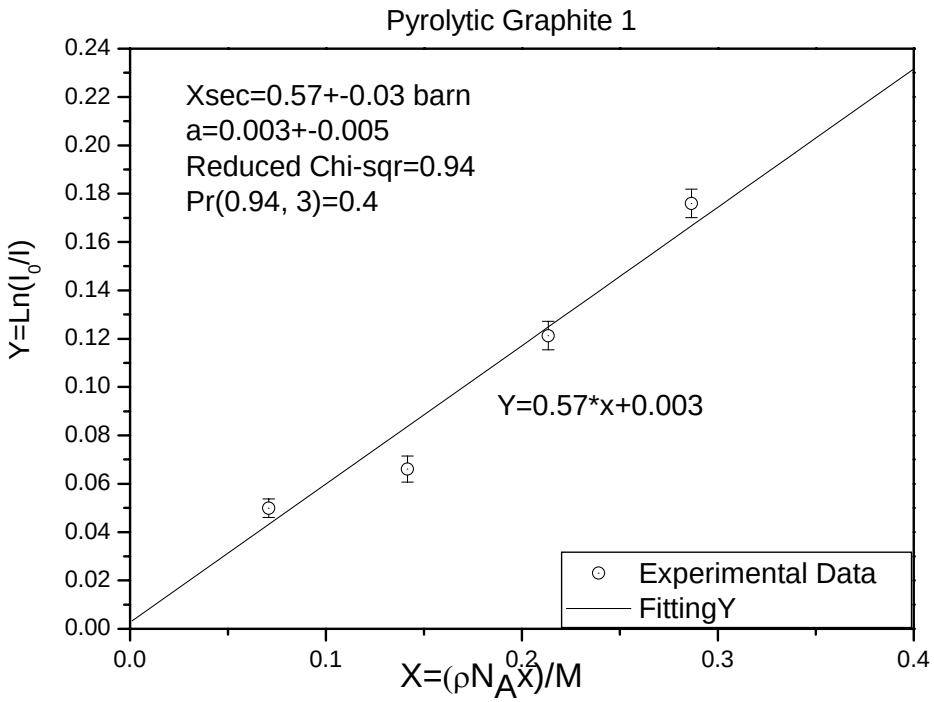

Figure 3-11. The fitted pyrolytic graphite total cross section for the neutron with wavelength 0.89 nm.

Table 3-6. The measurement of reactor grade graphite samples

	One piece of sample	Two piece of samples	Three piece of samples	Four piece of samples
$X = \frac{\rho \cdot N_A}{M} \cdot x$ (barn^{-1})	0.053334832	0.107087649	0.161091256	0.214760476
$Y = \ln(\frac{I_0^\lambda}{I^\lambda})$	8.647730E-02	1.840613E-01	2.928646E-01	4.049704E-01
σ_Y	3.5932E-03	5.6367E-03	7.0387E-03	7.9639E-03

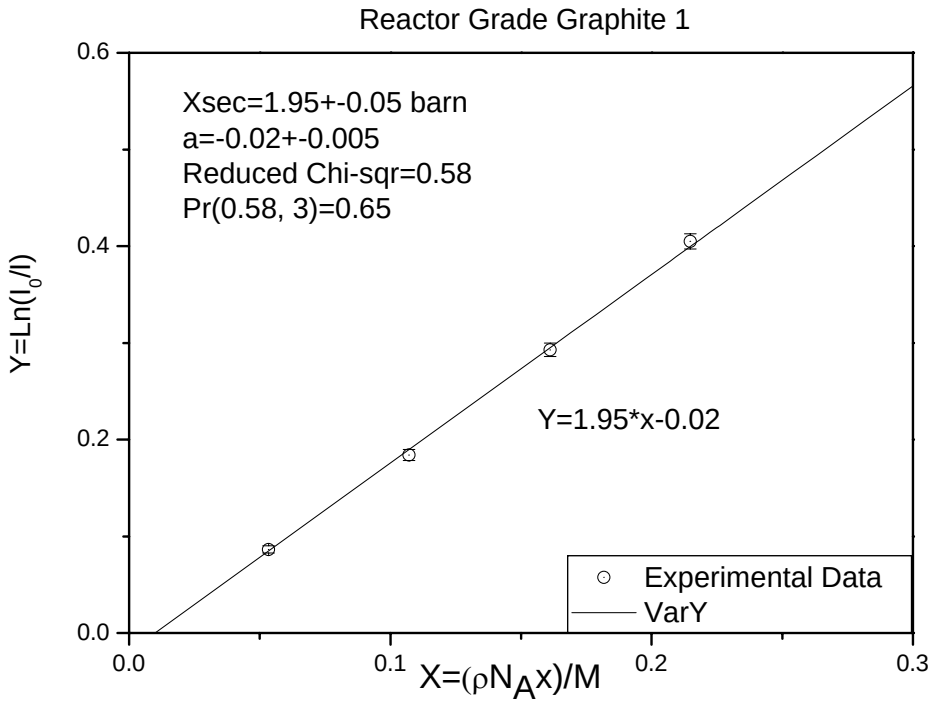

Figure 3-12. The fitted reactor grade graphite total cross section for the neutron with wavelength 0.89 nm.

Table 3-7. The measured total cross-section of samples with reference values

	Aluminum	Pyrolytic Graphite	Reactor Grade Graphite
Measured total neutron cross section at λ=0.89nm (barn)	1.40±0.03	0.57±0.03	1.95±0.05
Reference Value (barn)	1.44 [50]	0.37 [51]	0.66 [50] and 0.44 [52]

The measured total cross-sections of all the samples are shown in Table 3-7. As it can be seen, the measured total cross-section of pyrolytic graphite is larger than the referent value by about 100% and the measured total cross-section of reactor grade graphite is larger than the reference values by about 200% and 350%. These large discrepancies can be explained by that the small angle deflection neutrons were not taken into account in the measurement. Such small angle events

similar to X-ray , were discussed by Weiss [53].

3.4.2 Neutron small angle deflection in graphite

Graphite, depend on the type, does not always have the perfect crystalline structure. There are a large amount of pores distributed in reactor grade graphite samples, shown in Figure 3-13. Neutrons passing through a graphite sample can be refracted when they travel from matter into pores or to the opposite way. Ordinarily a neutron will cross a big number of pores when it travels though a graphite sample. Therefore, multiple refractions happen and neutrons can be removed from the original direction by a noticeable angle. The small angle deflection effect can be represented by a macroscopic cross-section, defined as Σ_{sad}. Therefore the total macroscopic cross-section of a graphite sample can be written by

$$\Sigma_t = \Sigma_s + \Sigma_a + \Sigma_{sad} \tag{3.17}$$

In equation (3.17), Σ_s is the nuclear scattering cross-section and Σ_a is the absorption cross-section. In this experiment, the nuclear cross-section $\Sigma_s + \Sigma_a$ is the essential parameter to measure. It's necessary to estimate the term Σ_s of different type of graphite samples.

Neutrons are refracted by matter in the same way as X-ray, and the theory and mathematics are completed and available. In 1984, the effect of neutron multi-refraction in ferromagnetic materials was studied and analyzed by A J Allen and D K Ross [54]. By following the same analysis, the effect of neutron multi-refraction in porous materials (for example, reactor grade graphite) can be studied.

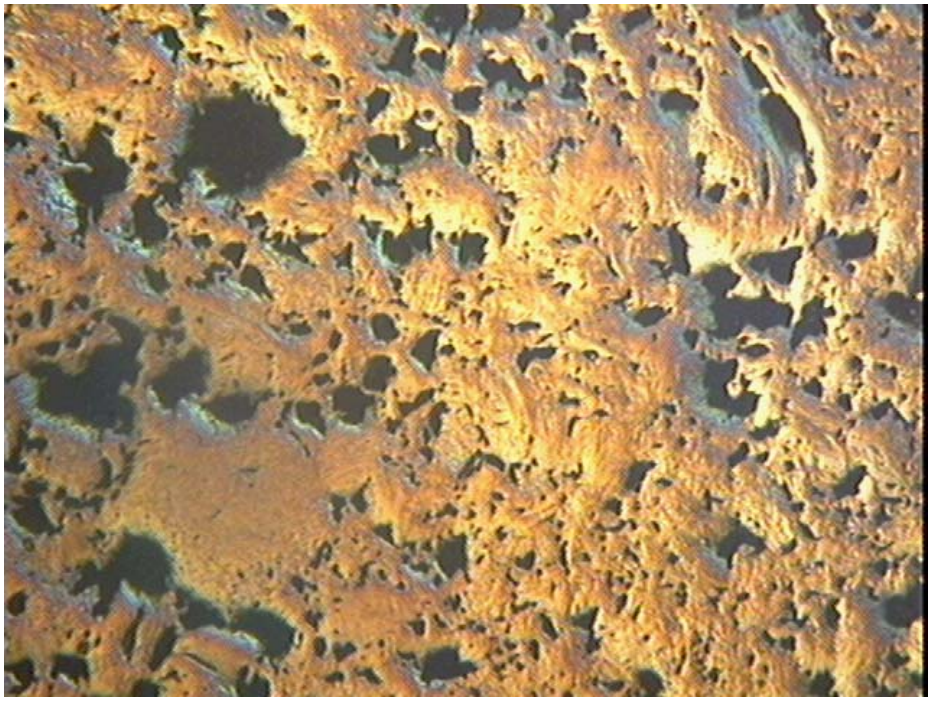

Figure 3-13. Reactor grade graphite sample surface picture taken by a scanning microscope at NCSU.

Refraction index of neutron can be written by [55]

$$n = 1 - \frac{\lambda^2 N}{2\pi}\bar{b} \tag{3.18}$$

Where,

$$\bar{b} = \sqrt{\frac{\sigma_{total}}{4\pi}} \tag{3.19}$$

Define:

$$\delta = \frac{\lambda^2 N}{2\pi}\bar{b} \tag{3.20}$$

Incident angle is i and refraction angle is r.

Then one can get

$$\sin i = (1-\delta)\sin r \tag{3.21}$$

Define:

$$r = i + \varepsilon \tag{3.22}$$

Assume the multi-refraction will give a Gaussian broadening effect. For a single refraction, ε will satisfy the Gaussian distribution with zero mean and σ_1 standard deviation. Consider neutron transmit through m number of uncorrelated pores, ε will satisfy the Gaussian distribution with zero mean and σ_m standard deviation, where

$$\sigma_m = m \times \sigma_1 \tag{3.23}$$

σ_1 can be written by [56]

$$\sigma_1^2 = <\varepsilon^2> = \frac{1}{2}\left[8\delta^2 - 3\delta^2 \ln\left(\frac{\delta}{2}\right) + \frac{9}{2}\delta^2\right] = \frac{\delta^2}{4}\left[25 - 6\ln\left(\frac{\delta}{2}\right)\right] \tag{3.24}$$

Thus, the standard deviation for multi-refraction can be written by:

$$\sigma_m^2 = \frac{m\delta^2}{4}\left[25 - 6\ln\left(\frac{\delta}{2}\right)\right] \tag{3.25}$$

Now, the standard deviations on x and y axes normal to the incident direction are

$$\sigma_{mx}^2 = \sigma_{my}^2 = \frac{1}{2}\sigma_m^2 = \frac{m\delta^2}{8}\left[25 - 6\ln\left(\frac{\delta}{2}\right)\right] \tag{3.26}$$

Therefore, after knowing δ and m, the Gaussian broadening effect of the beam can be calculated. For a sample of reactor grade graphite with density of 1.66 g/cm^3 in the 0.89nm neutron beam, δ can be calculated as:

$$\delta = \frac{\lambda^2 N}{2\pi}\bar{b} = \frac{\lambda^2 N}{2\pi} \cdot \sqrt{\frac{\sigma_{total}}{4\pi}} = \frac{\left(0.89 \times 10^{-7}\right)^2 \frac{1.67}{12} \times 6.022 \times 10^{23}}{2\pi} \cdot \sqrt{\frac{4.8 \times 10^{-24}}{4\pi}} = 6.53 \times 10^{-3} \tag{3.27}$$

Assume the pore size distribution in a graphite sample is

$$f(r) = \frac{dV(r)}{dr} \tag{3.28}$$

Where the volume of pores is V(r) and the radii of pores is r. The total volume of pores (V_p) in the sample can be written by

$$V_p = \int f(r)dr \tag{3.29}$$

Giving a graphite sample with a surface of A and a thickness of T, the volume of the sample V_s=A*T.

Look at the sample from the direction of incident neutrons shown in Figure 3-14. For the pores with radii $r_i \in (r, r+dr)$ i=1 to n, the number of a incident neutron across with pores is

$$dm = \frac{Total\_area\_of\_pores}{Sample\_area} = \frac{n \times \pi \cdot r^2}{A} = \frac{\frac{f(r)dr}{\frac{4}{3}\pi \cdot r^3} \times \pi \cdot r^2}{A} = \frac{3 \cdot f(r)}{4 \cdot A \cdot r} \cdot dr \tag{3.30}$$

Therefore,

$$m = \int dm = \frac{3}{4A}\int \frac{1}{r} \cdot f(r)dr = \frac{3T}{4V_s}\int \frac{1}{r} \cdot f(r)dr \tag{3.31}$$

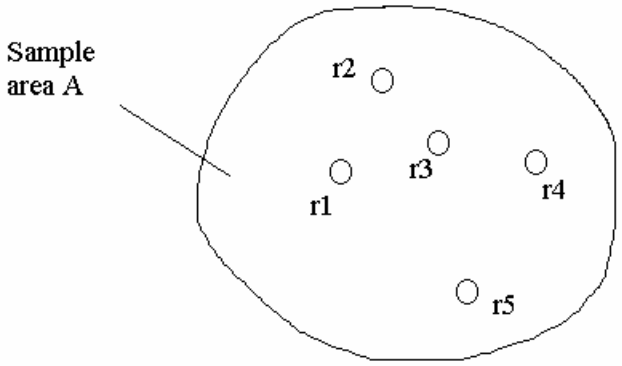

Figure 3-14. Porous sample.

The size distribution of pores in the range 20 to 300 Å in a graphite sample can be measured by using BJH method [57] from gas adsorption-desorption isotherms. Figure 3-15 is a typical pore

size distribution curve in this range for solid KC graphite [58]. Mercury porosimetry [59] can be used to study the pore size distribution in the range 350 to 100000 Å. Figure 3-16 is a porosimetry measurement of base graphite [60] in this range, in which the curve for AGOT was used in this work.

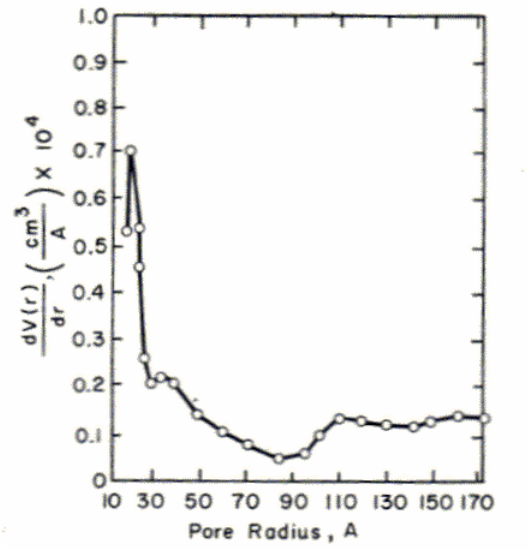

Figure 3-15. Pore size distribution curve in the range 10 to 300 Å [58].

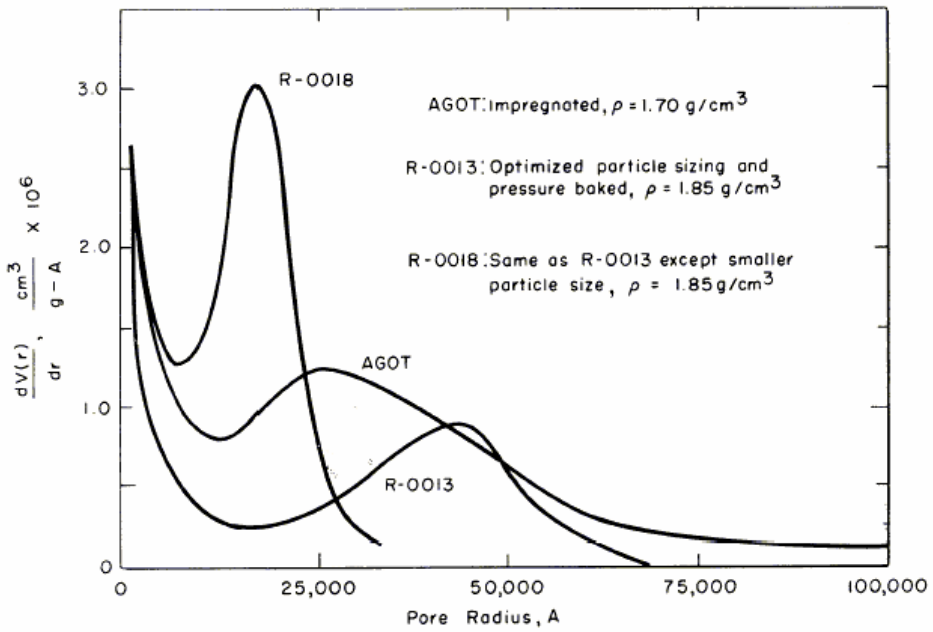

Figure 3-16. Porosimetry of base graphite [60].

The measured pore size distribution of reactor grade graphite can be obtained by combining the data points in Figure 3-15 and 3-16. Therefore, for a sample with a thickness of 2.569 cm, which is thickest in this experiment, the number of pores which an incident neutron can transmit can be calculated to be 3.4×10^{4}. And the standard deviation on the x axis of Gaussian broadening (σ^2_{mx}) can be calculated to be 1.58×10^{-3}. Therefore, σ_{mx} is equal to 2.3 degree. Figure 3-17 is the broadened beam with σ=2.3 degree. The effect of neutron multi-refraction depends on the pore size distribution in the sample. Thus the neutron beam will be broadened differently when passing through samples of reactor grade graphite and pyrolytic graphite.

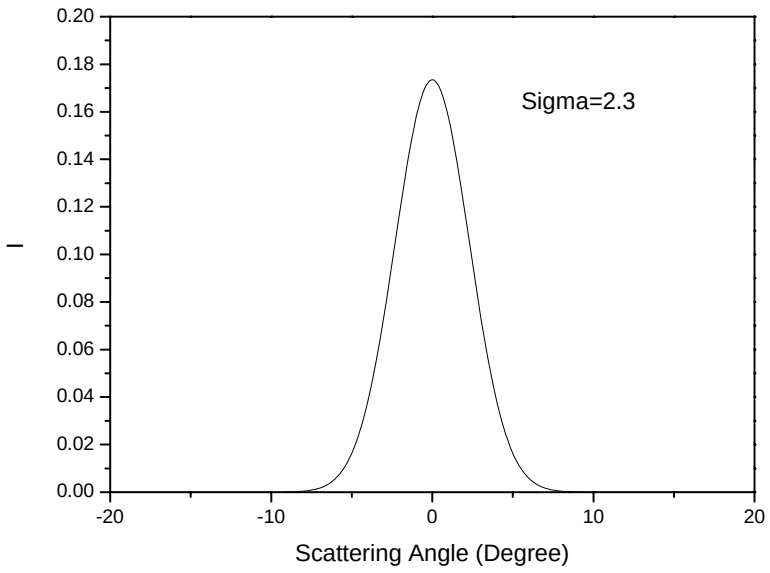

Figure 3-17. Neutron beam with multi-refraction broadening effect.

Beside the multi-refraction broadening effect, 1meV neutron passing through a graphite sample will be scattered inelastically. The NJOY99 code [40] was utilized to study the angular distribution of secondary inelastic scattering neutrons with 1meV incident energy, shown in Figure 3-18. The Young and Koppel phonon spectrum [41] was used as NJOY99 input, in a fashion

similar to that used for generating the standard MCNP libraries from ENDF data.

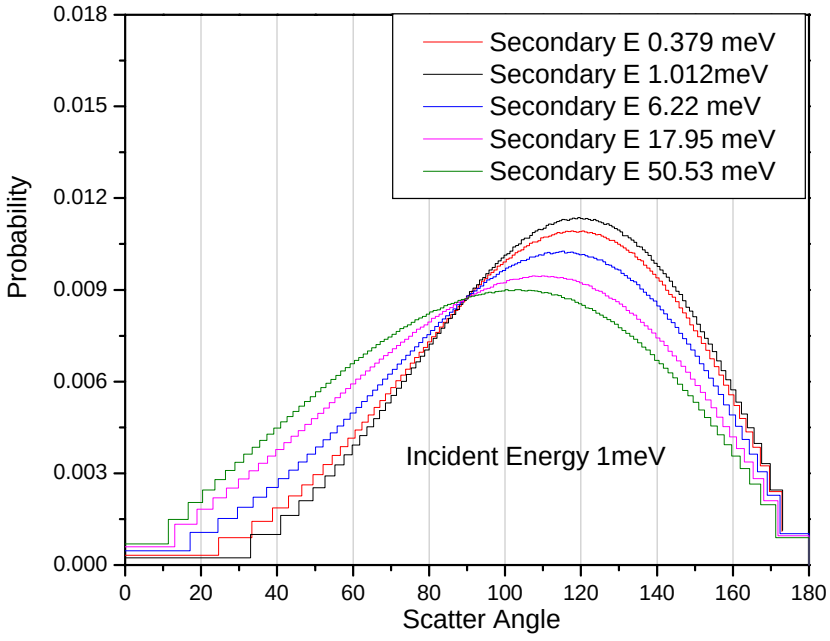

Figure 3-18. Angular distribution of inelastic scattering neutrons with different secondary energies.

As it can be seen in Figure 3-18, the scattering angle of a neutron suffered by inelastic scattering varies from 0 degree to 180 degree, but most of neutrons will have a scattering angle larger than 20 degree. On the other hand, the scattering angle of a neutron suffering multi-refraction effect is relatively small (less than 10 degree). As a result, the neutrons suffered by multi-refraction and inelastic scattering can be discriminated by the scattering angle. To measure the transmission only due to the inelastic scattering, the neutron beam divergence to the detector can be optimized so that most of the multi-refraction neutrons can be detected and most of the inelastic scattering neutrons can escape.

As discussed above, the geometry of the experimental setup was modified from Figure 3-2, given a name "Setup 2". The collimator 3 was replaced by another collimator with a larger opening aperture and placed closer to the sample holder, shown in Figure 3-19. The detector was moved closer to the sample holder also. Thus, the beam divergence at the detector is 0.34 steradians, which is 19.4 degree on axis. This beam divergence is consistent with the Steyerl's value (0.4 steradians) when he measured the total cross section of pyrolytic graphite for UltraCold neutrons in the 1970s [51].

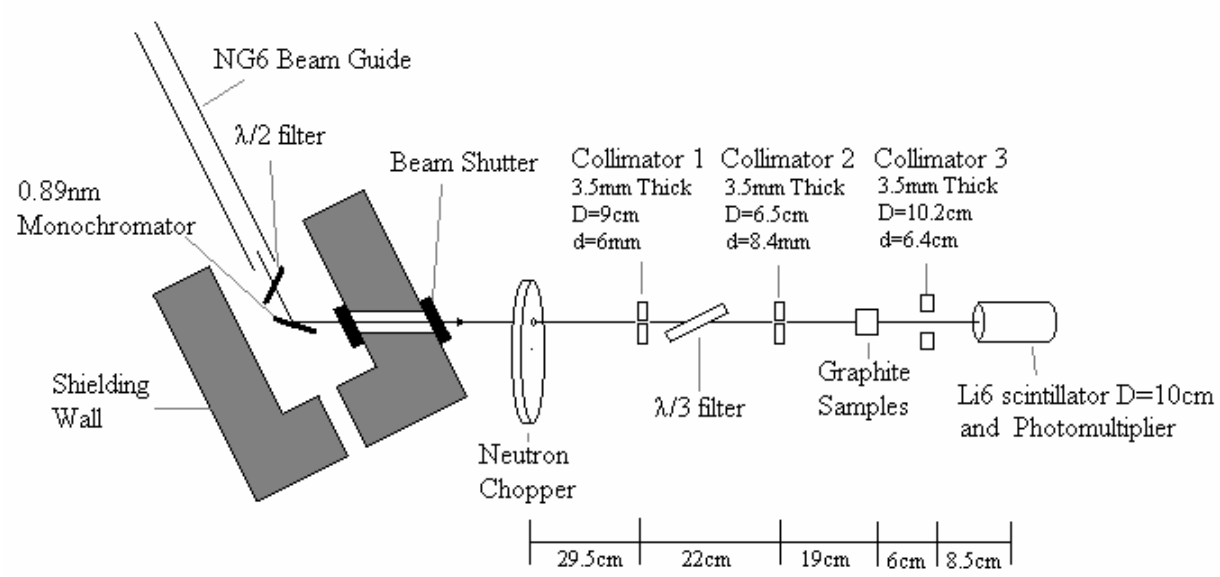

Figure 3-19. Experimental setup 2.

MCNP5 was used to simulate setup 2, shown in Figure 3-19, with 4 pieces of reactor graphite samples (2.59 cm thick). The number of neutrons which are scattered inelastically into the detector was estimated. The MCNP simulation gave the total neutron flux in the detector 0.6677±0.0006 (neutron/cm^2/source neutron), which include the uncollided neutrons and the small amount of scattering neutrons. While, the uncollided neutron flux in the detector is estimated to

be 0.6621±0.0006. Thus, the flux in the detector coming from the inelastic scattering neutrons is 0.0056±0.0008, which is 0.84±0.12% of the total neutron flux. Therefore, the transmission measured by using this experiment setup will be overestimated by less than 1%. However, the neutron multi-refraction effect will be removed.

3.4.3 Experimental setup 2 measurement results

The reference total cross sections $\Sigma_{E1}, \Sigma_{E2}, \Sigma_{E3}, \Sigma_{E4}$ shown in Table 3-4 were used to do the non-0.89nm neutron correction. Measurements were taken by using the different type of graphite samples. The corrected measurement data are shown in Table 3-8 and 3-9 for pyrolytic graphite and reactor grade graphite samples respectively. The fitting curves for pyrolytic graphite and reactor grade graphite samples are shown in Figure 3-20 and 3-21.

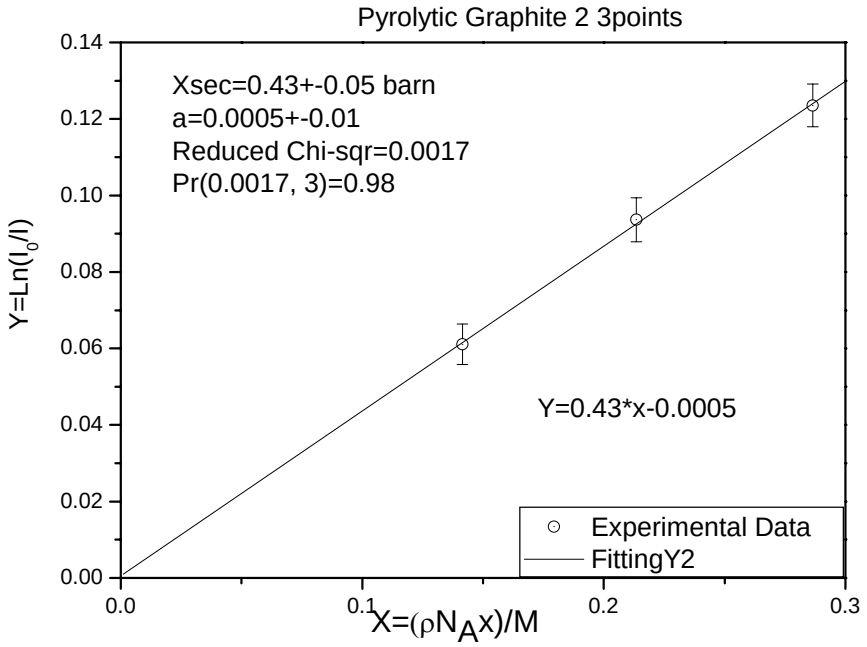

Figure 3-20. The fitted pyrolytic graphite total cross section by using the setup 2.

Table 3-8. The measurement of pyrolytic graphite samples by using the setup 2

	Two piece of samples	Three piece of samples	Four piece of samples
$X = \frac{\rho \cdot N_A}{M} \cdot x \quad (barn^{-1})$	0.141537073	0.213520047	0.28649665
$Y = \ln(\frac{I_0^\lambda}{I^\lambda})$	6.109085E-02	9.365663E-02	1.235426E-01
σ_Y	5.3398E-03	5.7626E-03	5.5842E-03

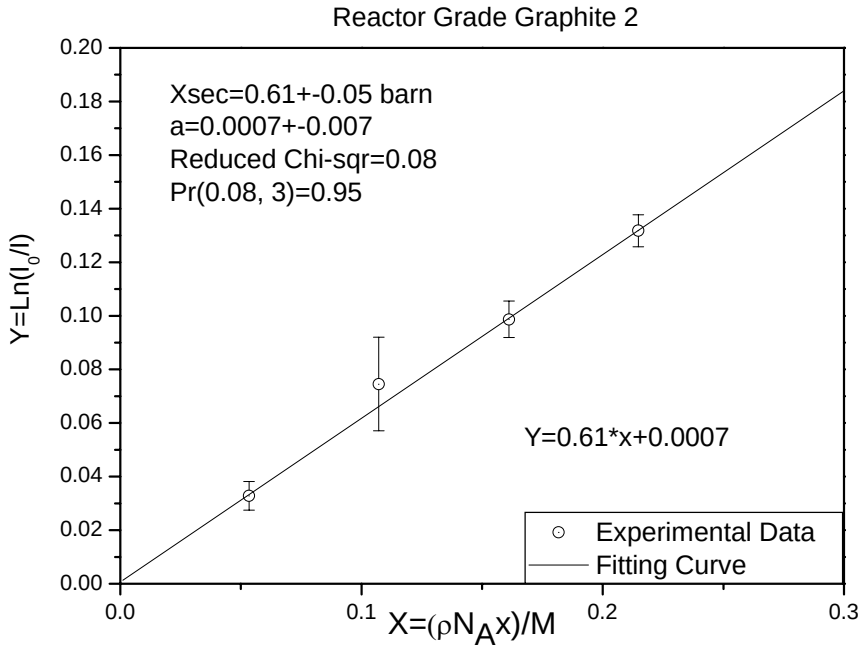

Figure 3-21. The fitted reactor grade graphite total cross section by using the setup 2.

Table 3-9. The measurement of reactor grade graphite samples by using the setup 2

	One piece of sample	Two piece of samples	Three piece of samples	Four piece of samples
$X = \frac{\rho \cdot N_A}{M} \cdot x \quad (barn^{-1})$	0.053334832	0.107087649	0.161091256	0.214760476
$Y = \ln(\frac{I_0^\lambda}{I^\lambda})$	3.283332E-02	7.450076E-02	9.869288E-02	1.317501E-01
σ_Y	5.3179E-03	1.7476E-02	6.8483E-03	5.9826E-03

3.5 Result

Table 3-10 shows the measurement results of the 0.89 nm neutron transmission experiment. The reference value of pyrolytic graphite is coming from the NCSU-1P Library [7] which matches the Steyerl's data [51], shown in Figure 3-22. As it can be seen in Table 3-10, the measured pyrolytic graphite total cross-section of neutrons with wavelength of 0.89 nm is consistent with the Steyerl's data and the NCSU-1P library [7]. For the reactor grade graphite sample, the measured total cross-section is consistent with the BNL325 data [50]. It's concluded that the type of sample in BNL325 measurement is reactor grade graphite. The measurements of this experiment are reasonable for the pyrolytic graphite and reactor grade graphite.

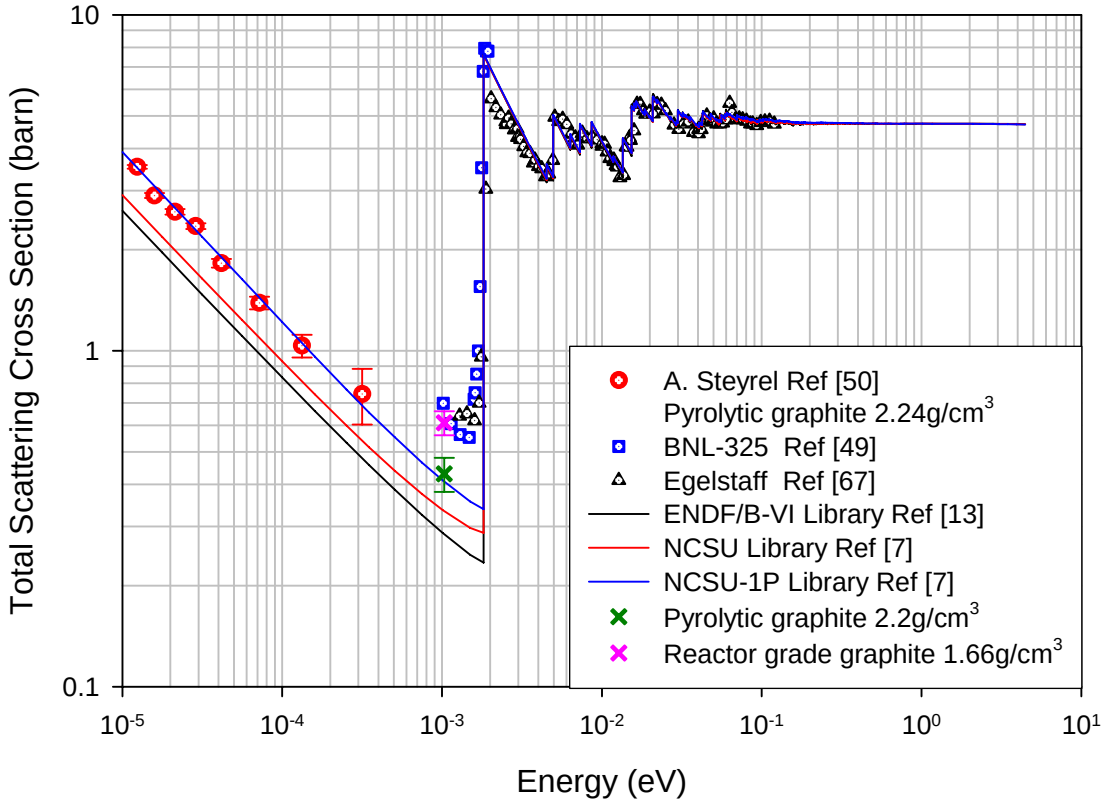

Figure 3-22. Transmission measurement results.

Table 3-10. The measured total cross-section of samples with reference values

	Aluminum	Pyrolytic Graphite	Reactor Grade Graphite
Measured total cross section at λ=0.89nm (barn)	1.40±0.03	0.43±0.05	0.61±0.05
Reference Value (barn)	1.44 [50]	0.37 [51]	0.66 [50] and 0.44 [52]

The thermal neutron inelastic scattering cross section depends on the structure of the graphite material. Pyrolytic graphite is a poly-crystalline material and each crystal piece has a graphite hexagonal structure. Reactor grade graphite is a porous and two-phase structure material, graphite crystal and binder carbons, which can be treated as amorphous-like carbon. The inelastic cross section of the carbon atoms in the graphite crystal is different from binder carbon. It is expected that the scattering properties of the binder carbon phase that is causing this difference in total cross section between pyrolytic and reactor grade graphite.

Chapter 4 Slowing-Down-Time Measurements at Room Temperature

4.1 Experiment setup

At room temperature, a 70x70x70cm graphite assembly was load on the furnace table. The furnace bell was not used in this case since heating was not needed. The detector located on the top was 45.9cm away from the surface of the graphite assembly. The detector located at the back was 45.2cm away from the surface of the graphite assembly. Measurements were taken with detectors on both locations. The graphite assembly and the detectors were enclosed by 5% boron polyethylene shielding board, as described in the chapter 2. To reduce gamma ray intensity in the beam, a 1/4 inch lead filter was load into the beam.

Three types of neutron detectors were utilized in the measurements. They are two lithium6 detectors and one uranium235 fission counter. The plutonium239 fission counter was not used due to its low counting rate. The major measurements were taken by using a lithium6 glass scintillator (GS20 [63]), which is made by Saint-Gobain Crystals & Detectors. The thickness of the lithium glass is 1mm and the diameter is 3 inches. The density is approximately 2.5g/cm^3. The total lithium in the detector is 6.6% and lithium6 enrichment is 95%. Another lithium6 detector is a ZnS(Ag) lithium detector (BC702 [64]), which has a 5 inches diameter and 6.35 mm thickness. The lithium content is around 11 mg/cm^3, in which ^{6}Li is enriched to 95%. The uranium235 fission counter is made by GE Power Systems Reuter Stokes. The fission counter

cylinder is 8 inches long with a 1 inch diameter and its sensitive length is 5 inches. The total quantity of uranium235 in the chamber is around 130mg.

Figure 4-1 illustrates the electronics connection of the data acquisition system. The parameters of the data acquisition system were setup as shown in Table 4-1. The ORELA accelerator was running at the frequency of 130 pulses/second, with a pulse width of 30ns. At the moment of a source neutron pulse, a negative square pulse is sent to the Multi Channel Scaler as a start signal. The Slowing-Down-Time spectra were measured in the Multi Channel Scaler and detector pulse height spectra were measured in the Multi Channel Analyzer.

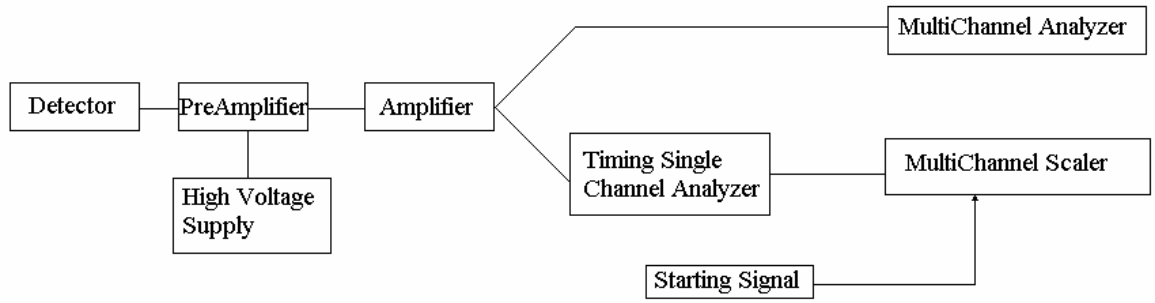

Figure 4-1. The data acquisition electronics connection.

Table 4-1 Parameters in the data acquisition system

Detector	Li-6 glass (GS20)	Li-6 ZnS (BC702)	U-235 fission counter
High Voltage	850V	700V	600V
Amplifier gain	0.55x100	0.7x10	0.7x50
Amplifier shaping time	1μs	1μs	1μs
Timing SCA window	0.9V ~ 4V	0.9V ~ 6V	0.9V ~ 6V
Timing SCA delay time	6μs	6μs	6μs
MCS channel number	8192	8192	8192
MCS dwell time	0.9μs	0.9μs	0.9μs
MCA channel number	2048	2048	2048

4.2 Measurements

A Slowing-Down-Time spectrum was measured by using the lithium6 glass scintillator (GS20) on

the back of the graphite assembly for 1 hour. At the same time, a detector pulse height spectrum was also measured in the Multi Channel Analyzer. The measured raw data are shown in Figure 4-2 and 4-3.

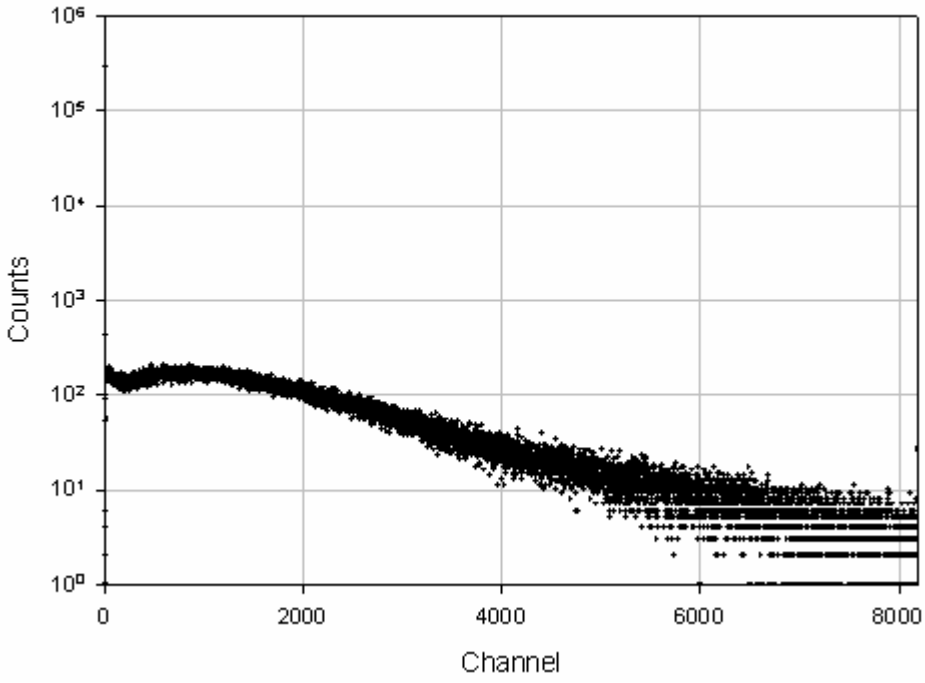

Figure 4-2. The measured SDT spectrum of the lithium6 glass scintillator on the back.

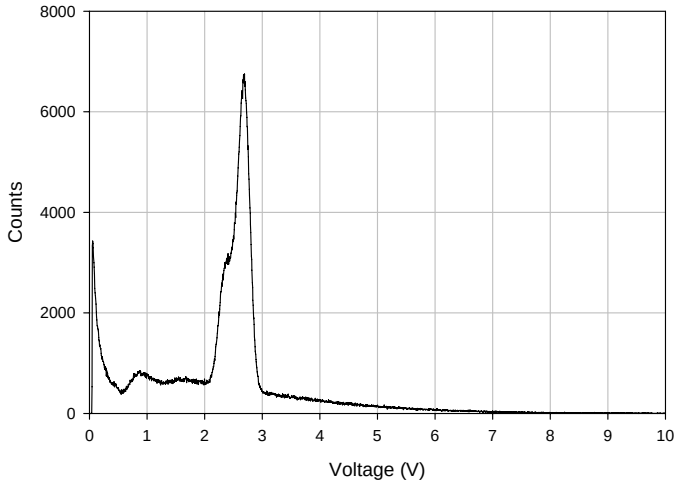

Figure 4-3. The detector pulse height spectrum of the lithium6 glass scintillator on the back.

By locating the lithium6 glass scintillator on the top of the graphite assembly, another measurement was taken for 1 hour. The two spectra measured in MCA and MCS are shown in Figure 4-4 and 4-5.

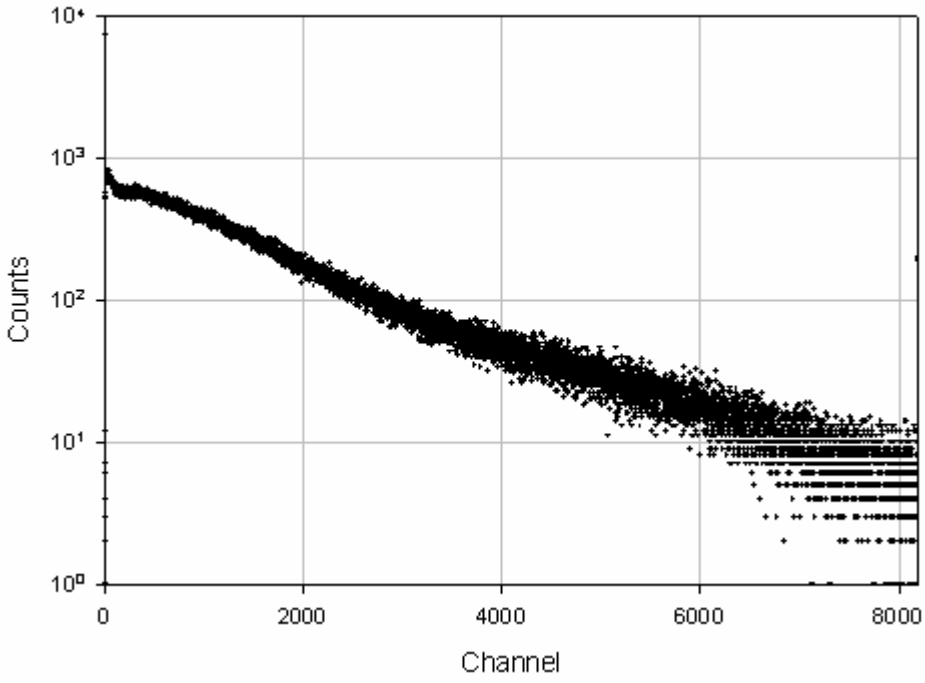

Figure 4-4. The measured SDT spectrum of the lithium6 glass scintillator on the top.

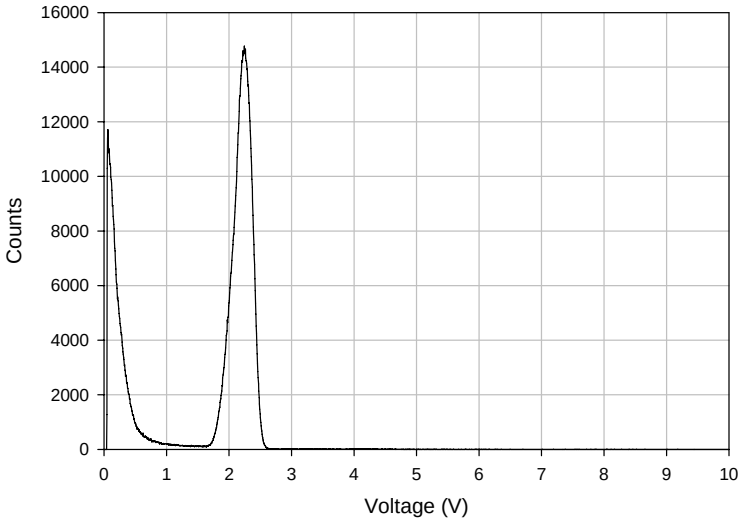

Figure 4-5. The detector pulse height spectrum of the lithium6 glass scintillator on the top.

In the detector pulse height spectra of the lithium6 glass scintillator on the top (Figure 4-5), the neutron peak is separated clearly from the gamma background due to the large Q-value (4.78MeV) of the (n,α) reaction in ^{6}Li. The discriminating window in the Timing Single Channel Analyzer was set to 0.9V to 4V, which discriminate most of the gamma background from the time spectrum. However, the detector pulse height spectrum of the lithium6 glass scintillator on the back looks not as clean as the spectrum on the top. That's because of the large intensity gamma flash in the neutron beam, which passes through the detector on the back. The energy of the gamma rays is in MeV range and large intensity can produce lots of pile-up in the photomultiplier. It's possible to have some pulses with large amplitude due to gamma. As a result, by setting up the discriminating window in the Timing SCA to 0.9~4V will not discriminate the gamma background completely from the time spectrum for the detector on the back. Nonetheless, these high-intensity gamma flash in the beam are generated at the moment when neutrons are generated, which happens within 30ns after each starting signal. The gamma flash travel from the target to the detector at the speed of light and its flight time is $t = \frac{10m}{c} = 0.03\mu s$. Therefore, the gamma flash will only contribute to the first channel in the Slowing-Down-Time spectrum, in which the dwell time is 0.9μs. However, these high intensity gamma rays will cause the photomultiplier to be saturated in the short period of time after each source neutron source. It takes several microseconds for the photomultiplier to recover. Consequently, there is a drop-down in the first tens channel of the time spectra with detector on the back (shown in Figure 4-10).

A measurement was also taken by using the uranium235 fission counter on the top of the graphite assembly. Since there are some resonance peaks in the uranium235 fission cross section from 1keV down to 0.3eV, the structures in the measured Slowing-Down-Time spectrum can be used to

calibrate the neutron energy and time. The measuring time was 4 hours due to the low counting rate of the uranium235 fission counter. The two spectra in the MCA and MCS are shown in Figure 4-6 and 4-7. The discriminating level in the Timing SCA was set to 0.9~6V, which eliminate most of the alpha noise.

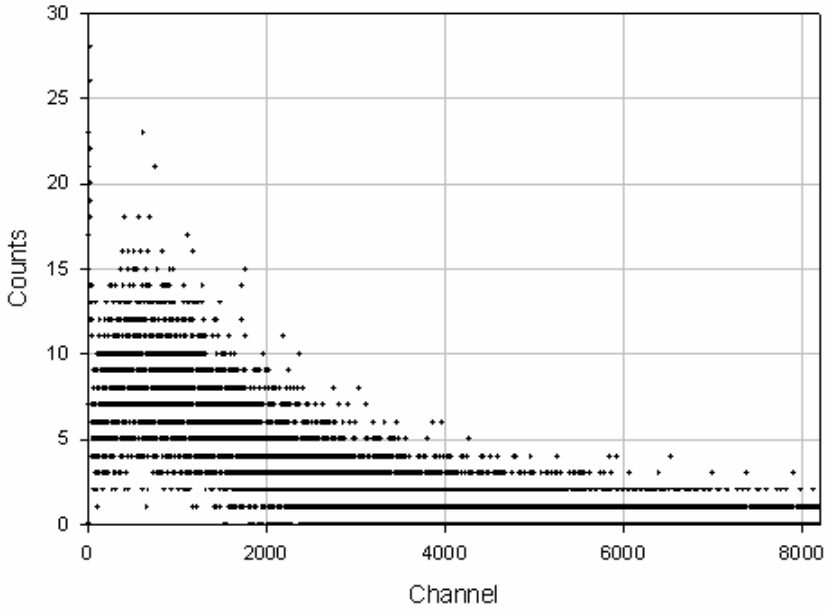

Figure 4-6. The measured SDT spectrum of the uranium235 fission counter on the top.

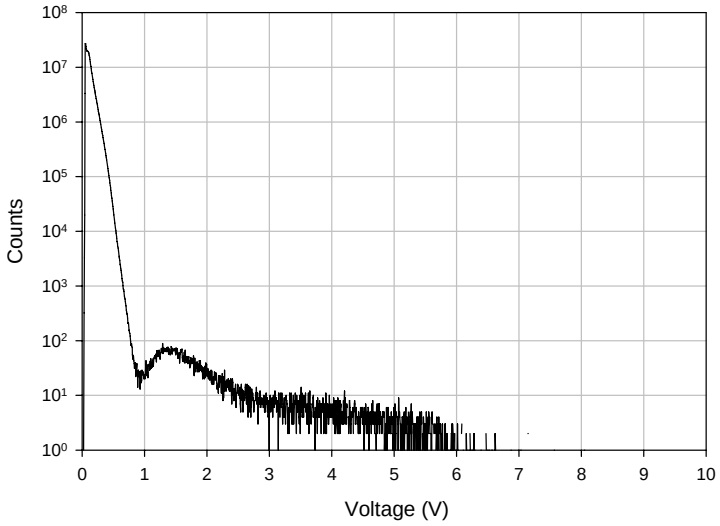

Figure 4-7. The detector pulse height spectrum of the uranium235 fission counter on the top.

4.3 Data analysis

4.3.1 MCNP simulation

The MCNP5 code was utilized to simulate the Slowing-Down-Time experiment. The MCNP model consist of a 70x70x70cm graphite assembly, a furnace table, a shielding system and a concrete room, which are described in Chapter 2. There is no furnace bell in the model since it's a room temperature measurement. The detector holders and a beam barrel, which are made from steel, are also included in the model. Figure 4-8 and 4-9 illustrate the MCNP model.

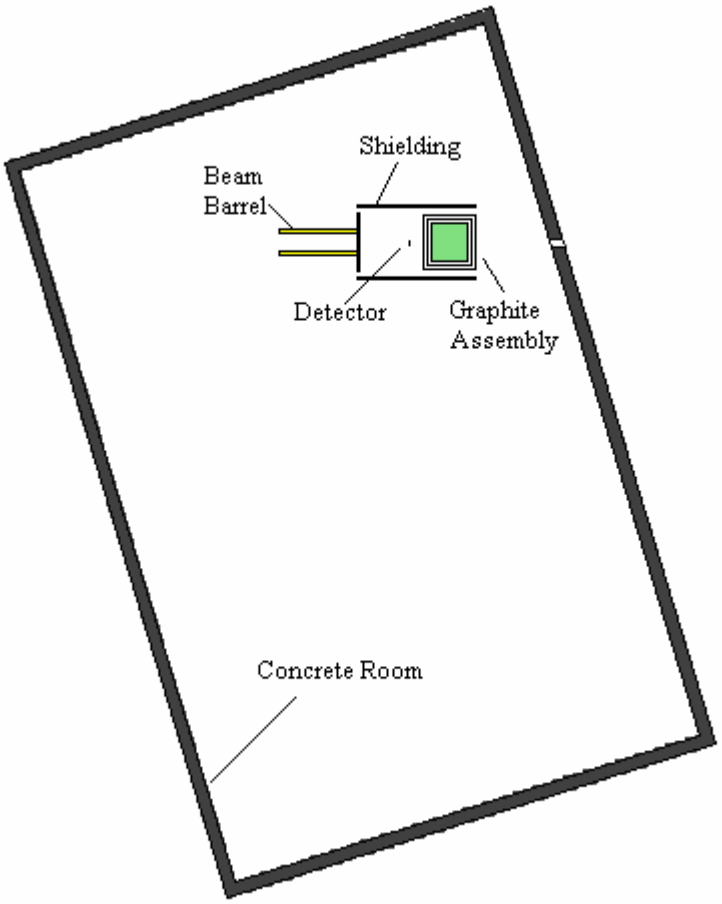

Figure 4-8. Top view of the MCNP model of the Slowing-Down-Time experiment at room temperature.

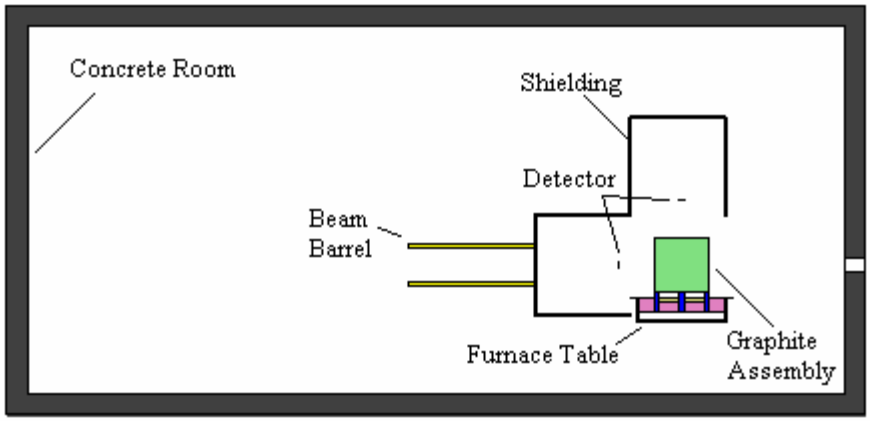

Figure 4-9. Side view of the MCNP model of the Slowing-Down-Time experiment at room temperature.

The data which the lithium6 scintillator measured is neutron reaction rate in the detector, which can be written by

$$R = \int \Phi(E)\Sigma(E)dE \qquad (4.1)$$

In which, Φ(E) is neutron flux in the detector. In the realistic case, the neutron flux will be disturbed by the detector itself. To simulate this situation, instead using a point detector, the lithium6 scintillator was included in the MCNP model and the neutron flux in the scintillator was tallied by using track-length estimator (F4 tally). In this case, the tallied neutron flux is multiplied by the ^{6}Li absorption cross section in order to calculate the reaction rate. The calculated time spectrum is compared to the measured time spectrum after normalization.

The time sweeping in the Multi Channel Scaler was setup to $0.9\mu s \times 8192 channel = 7.3728 ms$, which is slightly smaller than the time interval of the source neutron pulse $\frac{1}{130} = 7.6923 ms$. In

the MCNP model, the time bins are equal spaced in the log time scale, from 10^{-7} to 10^{-2} second. The total number of time bins is 100, i.e. 20 time bins in each decade. In order to get the reaction rate per log time and compare the measured time spectrum to the calculated one, the measured data were grouped into the equal space log time bins. In the case that a single measured time bin has contribution to two or more MCNP time bins, the data will be divided into several parts and each part is proportional to its time interval. A Visual Basic Application (VBA) code was developed for this job and can be found in the Appendix C.

4.3.2 MCNP calculations compared to experimental measurements

The measured data were grouped into the equal space log time bins and normalized by the time bin width. Figure 4-10 and 4-11 illustrate the measured data with a unit of counts/second and the spectra calculated by MCNP5 code. The calculated spectra were normalized in order to have same total counts in the fast neutron region, 9.46×10^{-6} to 4.22×10^{-5} second, as measured spectra. It's reasonable because the fast neutron cross sections of graphite in the ENDF/B-VI library are free carbon atom cross sections which are well measured and tested. And the spectra in the fast neutron region should be predicted by MCNP calculation very well. As it can be seen in Figure 4-10 and 4-11, the calculations agree with the measured spectra in the time region earlier than around 7×10^{-5} second, in which neutron energy is above 4eV. However, in Figure 4-10, the calculated spectrum does not agree with the measured spectrum in the time region earlier than 7×10^{-6} second. That's because the high intensity gamma rays come at very early time and contribute into the first channel (0.9μs) and cause the photomultiplier to be saturated for a well (around 7μs).

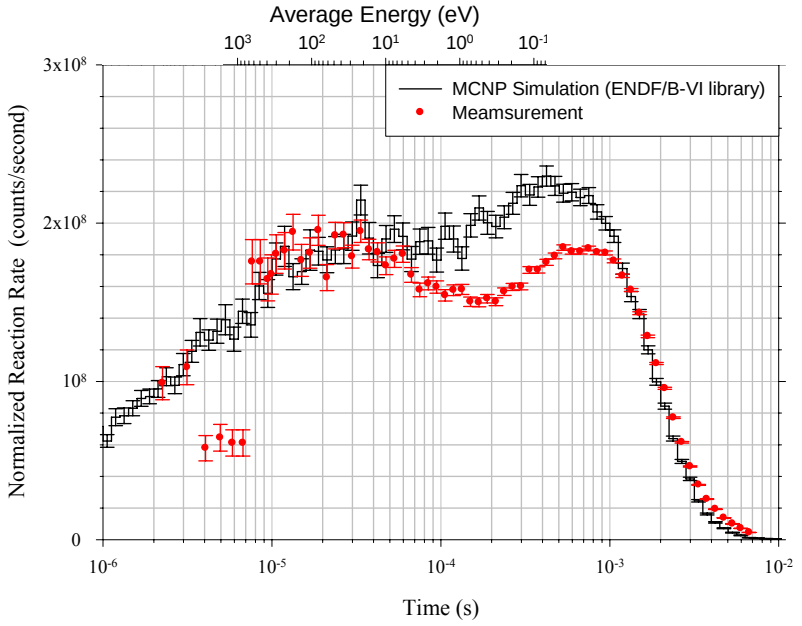

Figure 4-10. Simulated and measured time spectra of Li-6 glass scintillator on the back of the graphite assembly, the number of counts in each time bin was normalized by the time bin width.

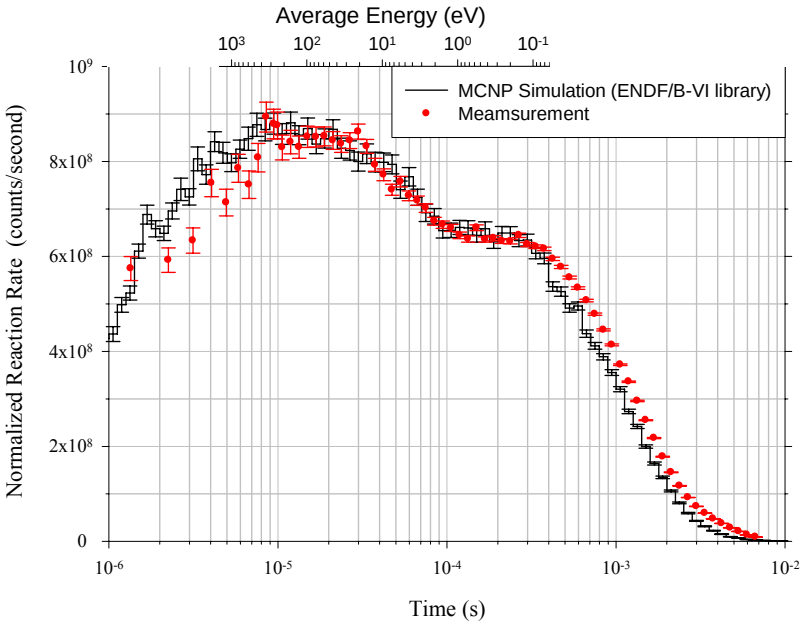

Figure 4-11. Simulated and measured time spectra of Li-6 glass scintillator on the top of the graphite assembly, the number of counts in each time bin was normalized by the time bin width.

Neutrons are slow down into thermal energy around $7x10^{-5}$ second later than every source neutron pulse. In this thermal neutron region, the calculated spectra begin diverge from the measurements in different behaviors for the detectors on the top and to the back. The differences between the calculations and measurements can be as large as 30 to 40% as shown in Figure 4-12.

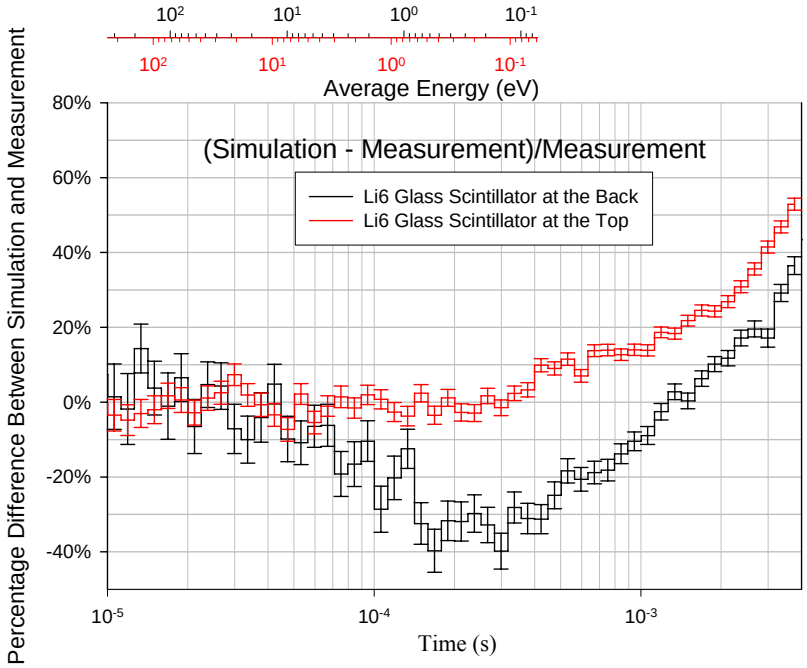

Figure 4-12. Percentage difference between the MCNP simulation based on ENDF/B-VI library and measurements for the Li-6 glass scintillator on the back and top of the graphite assembly.

The measured data grouped into the equal log time bins without normalized by the time bin width are time spectrum per log time. The unit becomes counts instead of counts/second. Figure 4-13, 4-14, 4-15 and 4-16 illustrate the measured time spectra per log time compared to the calculated spectra in log-log and semi log scale. In this way, the statistical errors on the measurement become explicable (the lower the spectrum, the higher statistical error) and the agreements on the fast neutron region between the measurements and calculations become obvious.

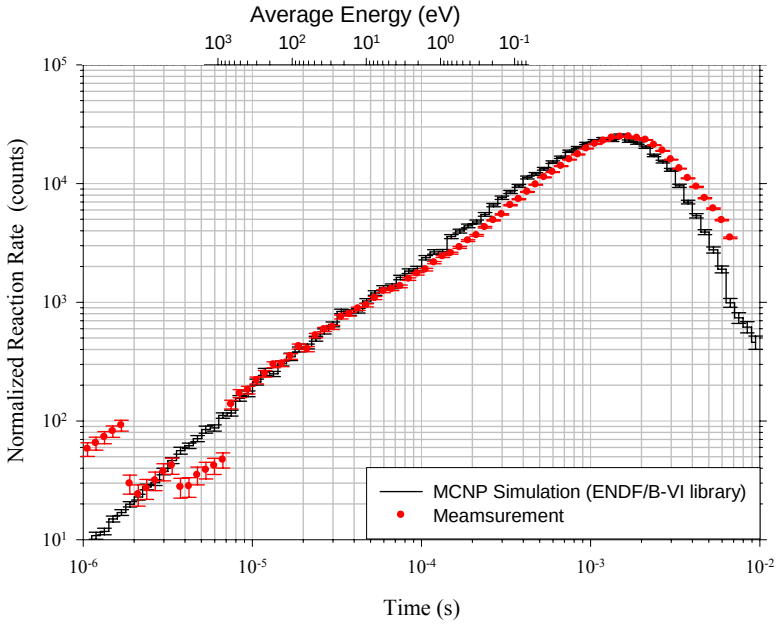

Figure 4-13. Simulated and measured time spectra per log time of Li-6 glass scintillator on the back of the graphite assembly, the statistical error of the measured data in the normalization region is 1.23%.

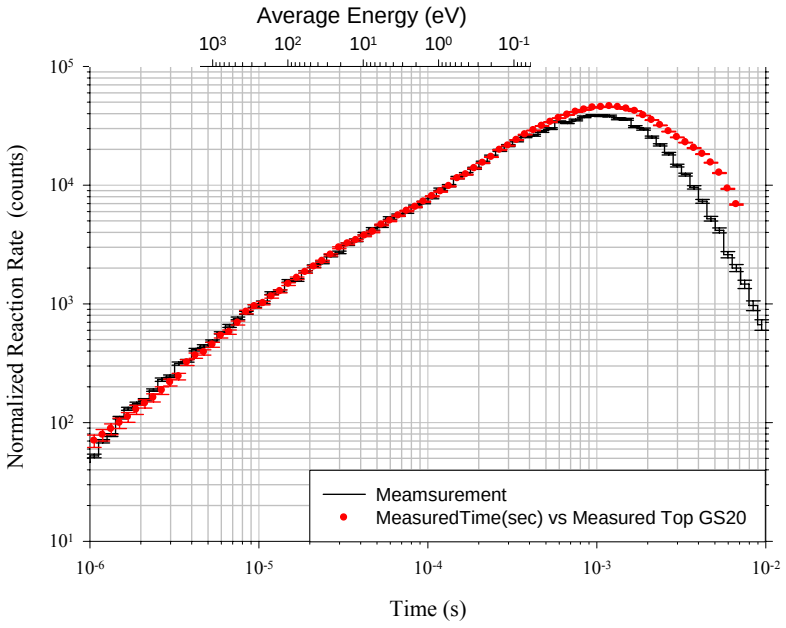

Figure 4-14. Simulated and measured time spectra per log time of Li-6 glass scintillator on the top of the graphite assembly, the statistical error of the measured data in the normalization region is 0.58%.

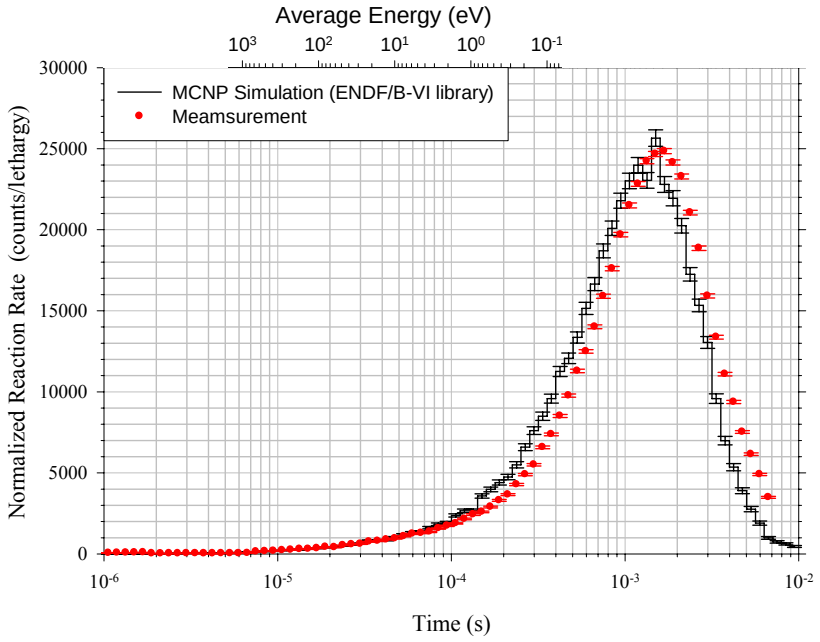

Figure 4-15. Simulated and measured time spectra per log time of Li-6 glass scintillator on the back of the graphite assembly.

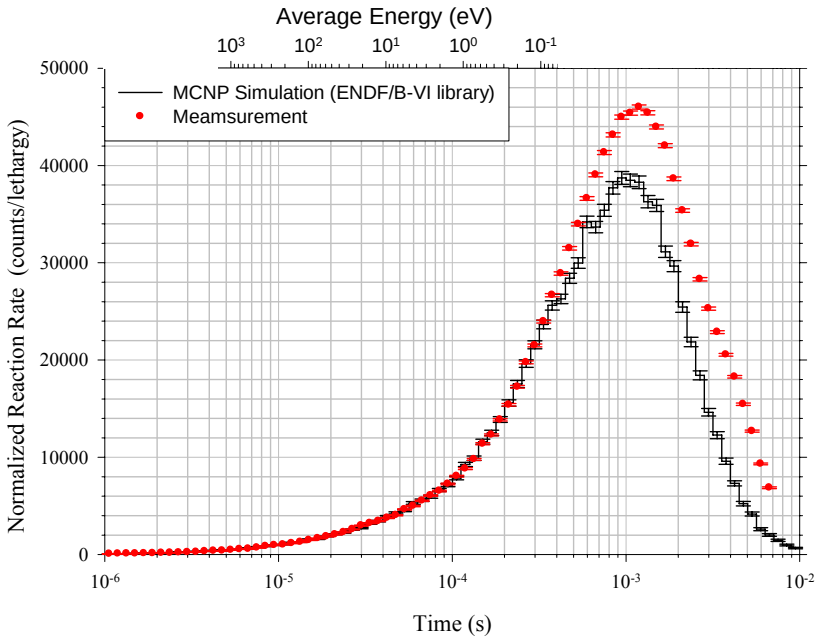

Figure 4-16. Simulated and measured time spectra per log time of Li-6 glass scintillator on the top of the graphite assembly.

4.3.3 Slowing-down-time and neutron energy correlation

The neutron absorption cross section of Li-6 has 1/v behavior for thermal neutron and there is no resonance peak in the absorption cross section. As a result, the spectra measured by using Li-6 detector are smooth curves without structure. There's no way to check the correlation between slowing-down-time and neutron energy by using Li-6 detector. However, in the U-235 fission cross section, there are tons of resonance peaks for the epithermal neutron and few resonance peaks for thermal neutron. Thus, the spectrum measured by using U-235 fission counter on the top can be used to check the time and energy correlation.

Figure 4-17 illustrates the measured U-235 time spectrum on the top normalized by the time bin width and the calculated spectrum. The counting rate of the U-235 fission counter is 2 orders of magnitude lower than the Li-6 scintillator, around 1.3 counts/second. The statistic is limited by the total measuring time, which is 4 hours. The measured total counts in the normalization region, 9.46×10^{-6} to 4.22×10^{-5} second, are 483.1 and the statistic error is 4.55%. The uranium235 fission cross section was also plotted in the same figure. The resonance peaks at 4 eV and 1eV can be noticed on the calculated and measured spectra and they agree with each other, while the resonance peak at 0.3eV is hardly noticeable. That means the calculated neutron energy and slowing-down-time correlation is consistent with the measurement with the detector on the top.

The time spectrum measured by using U-235 fission counter on the top also shows disagreement with the calculated spectrum, which is consistent with the Li-6 scintillator measurement on the top in Figure 4-11. Apparently, this disagreement between measurement and calculation is detector independent.

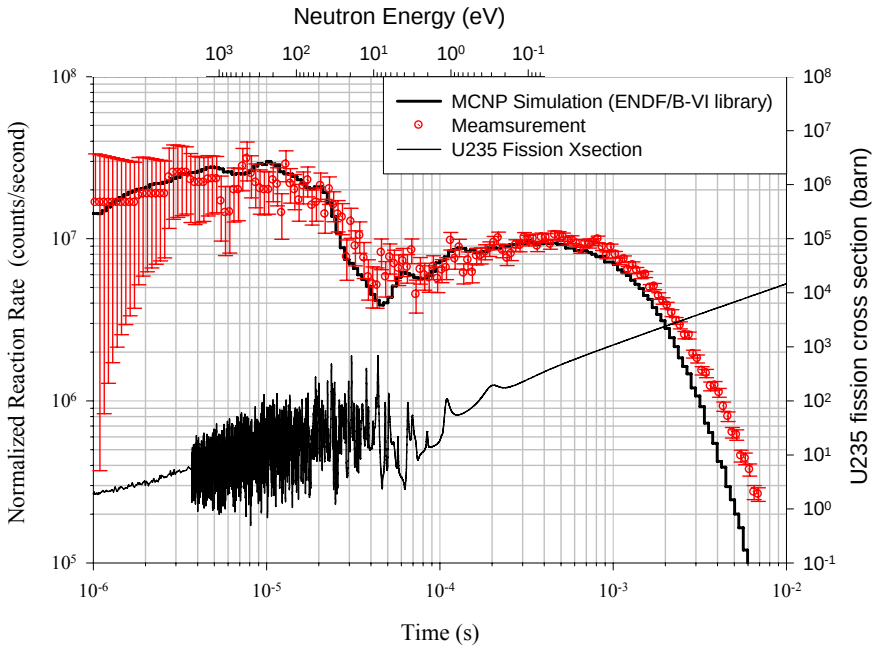

Figure 4-17. Simulated and measured time spectra of uranium235 fission counter on the top of the graphite assembly, the number of counts in each time bin was normalized by the time bin width.

4.3.4 Analysis of statistical error and systematic bias

The statistical errors of the measurements can be calculated based on Poisson distribution and are shown in Figures 4-10 to 4-17. In the thermal neutron region of the Li-6 scintillator measured spectra, the statistical error is as small as less than 1%, while for the spectrum by using U-235 fission counter the statistical error is as good as 4.5%.

The impurities in the reactor graphite pile, especially hydrogen, boron and so on, could cause a systematic bias on the measurements. To examine the effect of the impurities, a piece of reactor graphite sample was send to Shiva Laboratory (www.shivatec.com) and elemental concentration analysis was performed and attached in Appendix A. Two MCNP cases were calculated: one was

based on the pure reactor graphite pile, the other included all the elements with concentration larger or equal to 0.01 ppm (by weight). The percentage difference on the two time spectra is shown in Figure 4-

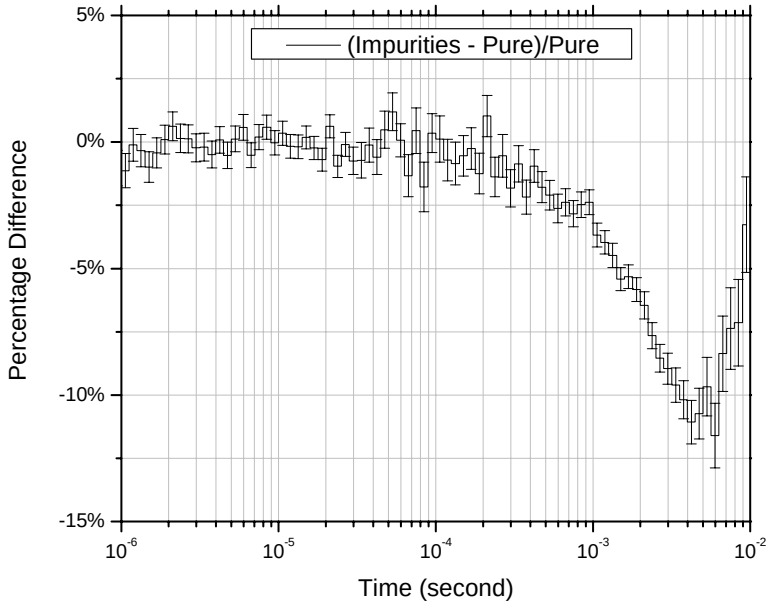

Figure 4-18. Percentage difference on the time spectra between the case with impurities in the pile and the case with pure graphite pile.

As it can be seen in Figure 4-18, the effect due to the impurities in the graphite pile is less than 2.5% before the SDT 10^{-3} second. After the SDT of 10^{-3} second, the impurities cause a drop in the time spectrum at the thermal energy. That can be explained by the fact that the impurities in the graphite pile will absorb some thermal neutrons. Considering the impurities will make the difference between the measurements and simulations (shown in Figure 4-12) even bigger.

The distance from a detector to the graphite assembly was measured directly by a tape ruler with around 2 mm uncertainty and the detector is aligned to the center of the assembly and neutron

beam. Assume the neutron beam is on X axis, the uncertainty on the X axis will be as small as 2 mm and uncertainty on the Y and Z axis could be around 1 cm. The uncertainty on the time spectrum due to the uncertainty on the measurement of detector position can be calculated. Three MCNP simulation cases were used to study this uncertainty. In the first case, the detector was place 27.5 cm away from the graphite assembly with the center right in the source neutron beam. In the second case, the detector was moved 1cm off from the center of the source neutron beam and kept the same distance away from the assembly. In the last case, the detector was in the center of the source neutron beam and was moved 1 mm close to the assembly. The relative difference between the first and second cases is shown in Figure 4-19 and the relative difference between the first and third cases is shown in Figure 4-19. As it can be seen in Figure 4-19 and 4-20, the bias on the time spectrum due to the 1 cm radial uncertainty is around 0.5% and independent to the slowing-down-time. The bias due to the 2 mm axial uncertainty is around 1% and also independent to the slowing-down-time. Apparently, uncertainties on the detector position are within the measurement statistical error.

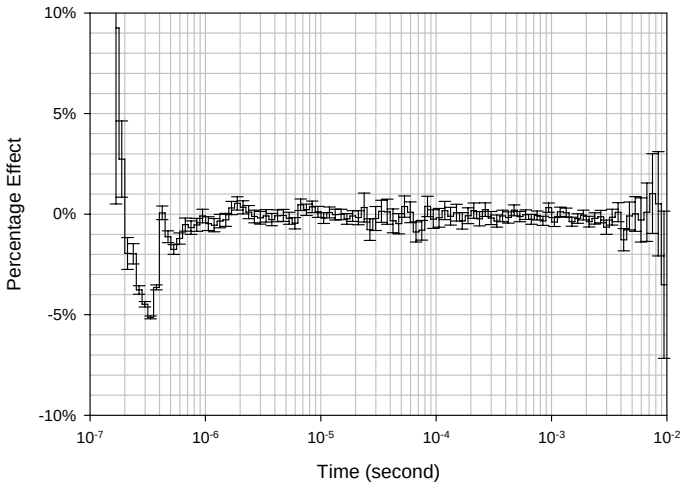

Figure 4-19. Relative difference on the time spectrum due to the detector 1 cm off from the center of the source neutron beam.

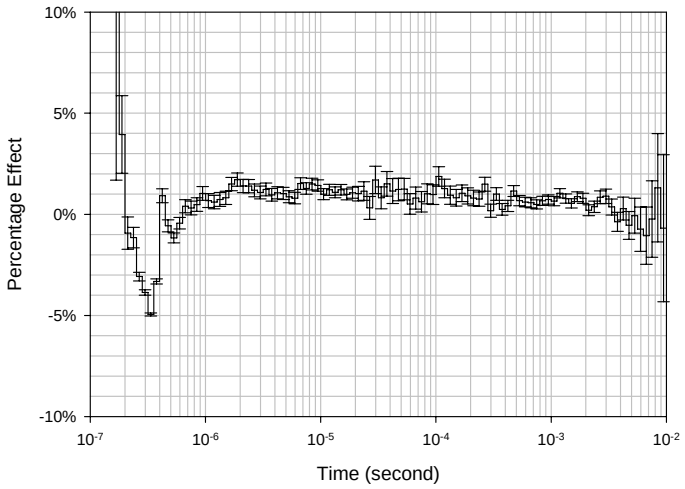

Figure 4-20. Relative difference on the time spectrum due to the detector 2 mm closer to the graphite assembly.

The uncertainty on the thickness of the Li-6 glass scintillator can cause a systematic bias in the measured time spectrum which can not be corrected by normalization. The thickness of the Li-6 glass disc used in the calculation is 1 mm. The maximum uncertainty on it is 20% [65]. Assuming the thickness is a normal distribution, the maximum uncertainty is approximately equal to 3σ. Therefore, the standard deviation is equal to 6.7%. Then the neutron flux in the detector can be calculated as:

$$\Phi_{\text{bias}} = \Phi_{\text{original}} \cdot \frac{\left(1 - e^{-\Sigma X}\right)}{\left(1 - e^{-\Sigma(X+\Delta X)}\right)} \tag{4-2}$$

For the neutron with energy 0.0253eV, the ratio $\frac{\Phi_{\text{bias}}}{\Phi_{\text{original}}}$ can be calculated to be 1.0277. For the neutrons with energy 100eV, which are in the normalization region, the ratio $\frac{\Phi_{\text{bias}}}{\Phi_{\text{original}}}$ can be calculated to be 1.0666. Therefore, after normalization the bias can be calculated to be

$1-\frac{1.0277}{1.0666}=3.65\%$. That means the uncertainty on the thickness of Li-6 glass scintillator can cause the thermal neutron region in the time spectrum shifted up or down by approximate 3.65% for both of the back and top detector measurements. Consequently, the disagreement between the calculations and measurements can not be explained by the uncertainty of the detector thickness.

The background due to the pulse overlap effect and scattering neutrons from the concrete room and other materials also can not be corrected completely by normalization. Since the measurements were taken at the pulse frequency 130 pulses/second, the pulse overlap effect is very small and is almost a constant at every moment, as described in Chapter 2. When plot the reaction rates of Li-6 scintillator per second instead of per log time, as shown in Figure 4-10 and 4-11, it can be seen that the tails of the spectra drops down to zero. The background is very small compared to the measured spectra except the tail. Therefore, the large difference between calculation and measurement in the time region later than $5x10^{-3}$ second can be partly made up by the background.

There are some materials close to the detector which may be able to scatter neutrons into the detector and cause some systematic bias, which are detector holders, beam barrel and stainless steel structure in the furnace table. Although the effects to the time spectrum cause by those materials are trivial, they are modeled by MCNP5 code properly.

4.3.5 Discussion of thermal neutron scattering cross section library

Based on what is discussed above, the disagreements between the measured time spectra and calculated time spectra can not be explained by the statistical error of the measurements. The disagreements can not be explained by the Li-6 scintillator efficiency because U-235 fission

counter shows the similar disagreement. The disagreements can not be explained by the uncertainty of the detector location. The disagreements can not be explained by the background. It's convincing that the disagreements are coming from the improper thermal neutron scattering cross sections of the reactor grade graphite which were used in the MCNP simulation.

It can be seen clearly in Figure 3-24 that the thermal neutron cross section in the ENDF/B-VI are smaller than the measured value below the Bragg cutoff energy. That means the inelastic scattering cross section of graphite in the ENDF/B-VI library is improper, which determined how neutron gain or lose energy by reacting with carbon atoms. As a result, the time spectra calculated based on the ENDF/B-VI library will not agree with measured time spectra. The NCSU-1P library [7], which was generated by North Carolina State University, agree with the crystalline graphite (pyrolytic graphite) on the total neutron cross section below the Bragg cutoff energy. Based on the analysis in Chapter 2, the difference between the calculated time spectra based on ENDF/B-VI library and the NCSU-1P library [7] is only around 3%, shown in Figure 2-68. Apparently, the disagreements between the calculations and measurements will not be released by using this new cross section library. That can be explained by that the thermal neutron scattering cross sections of reactor grade graphite are different from pyrolytic graphite, shown in Figure 3-24. The difference could be coming from the graphite binder structures in reactor grade graphite, which is considered to have an amorphous-like structure.

The total cross sections of amorphous-like carbon are close to the carbon free gas model [61]. Therefore, the easiest way to model amorphous-like carbon is to use free gas model. Assume in the reactor grade graphite, 10% carbon atoms are amorphous-like atom and 90% carbon atoms are

crystalline graphite. The average total cross section will match the measured reactor grade graphite cross section in Figure 3-24. In term of the slowing-down-time experiment, a new MCNP model was made by putting 10% amorphous-like carbon into the 70x70x70 cm graphite pile. The thermal neutron scattering cross sections for the 10% amorphous-like carbon atoms are from the free gas model and the NCSU-1P library [7] is used for the other 90% carbon atoms. The calculated time spectra based on the combined libraries were compared to the calculated time spectra based on the ENDF/B-VI library. The relative differences of the detector reaction rates on the top and back are as large as around 5%, shown in Figure 4-21. This combined library still does not make up the 30 to 40% difference between the calculations based on the ENDF/B-VI library and the measurements.

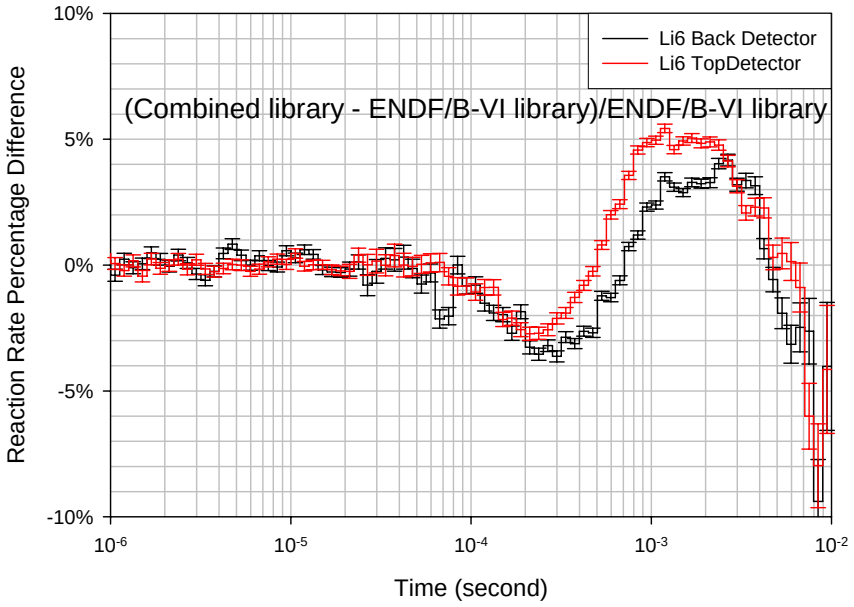

Figure 4-21. Percentage differences between the Li-6 detector reaction rate as a function of slowing-down-time based on the ENDF/B-VI library and the combined library (10% amorphous-like and 90% NCSU-1P [7]) for the detector on the top and back.

As it can be seen in Figure 4-21, the calculated reaction rate of the Li-6 detector on the back was

moved down by using the combined library in the time region 10^{-4} to $6x10^{-4}$ second (valley) and moved up after $6x10^{-4}$ second (peak). This trend makes the calculated reaction rate closer to the measurement. For the top detector, the difference on the valley becomes smaller than the back detector. Moreover the reverse of the reaction rate difference of the top detector happens earlier than the back detector and the difference on the peak becomes larger. This behavior is also consistent with the measurements. Imaging if the reaction rates for the top detector were calculated based on the correct cross section library, the valley becomes even smaller and close to zero, the reverse happens much earlier and the peak becomes even larger, in this way, the calculated reaction rates will become closer to the measurements. The reaction rate of Li-6 detector was calculated by using the equation (4.1). The increasing of the reaction rate can be caused by increasing neutron flux and a softer neutron flux (lower average neutron energy) due to the 1/v behavior of the Li-6 absorption cross section. Further investigation of this approach is needed.

In order to get a preliminary library, the differential cross sections were calculated by using LEAPR module in NJOY99 code, with a measured density of state [66] as an input. The normalized differential cross section was inserted into a thermal neutron library with the total cross section equal to the free gas model, which matches the measured total cross section of amorphous-like carbon. The new library was used to simulate the slowing-down-time experiment and calculate reaction rates of Li-6 detector on the top and back, shown in Figure 4-22 and 4-23 as a red line. As it can be seen, the calculate Li-6 reaction rates by using 10% amorphous-like carbon latest library match the measured data better in some region. Nevertheless, the calculations still do not agree with the measurements over the whole region.

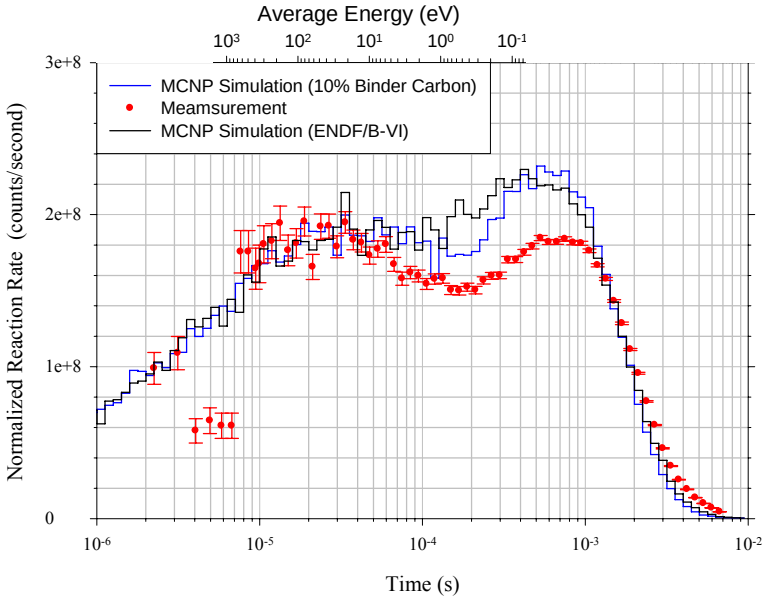

Figure 4-22. Simulated and measured time spectra of Li-6 glass scintillator on the back of graphite assembly.

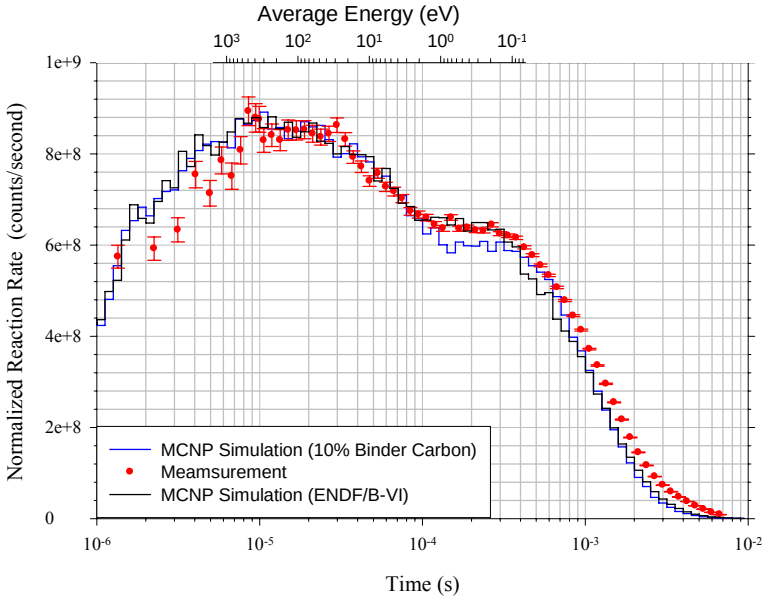

Figure 4-23. Simulated and measured time spectra of Li-6 glass scintillator on the top of the graphite assembly.

Chapter 5 Conclusions and Future Work

5.1 Conclusions

A graphite Slowing-Down-Time (SDT) experiment at room and high temperatures has been designed and setup at the Oak Ridge National Lab. The setup includes a 70x70x70 cm graphite assembly, the heating system (furnace), the shielding system, the valve controlling and data acquisition systems. Additional graphite elements to make 1x1x1 m and 50x50x50 cm assemblies were also prepared. A number of MCNP5 models were created to analyze the neutron flux as a function of slowing-down time and energy. A Finite Element Analysis code, ANSYS, was utilized to perform the design of the heating system. A LabView code was developed to control the valve system and to monitor the temperatures.

The MCNP5 version 1.30 code was modified to enable perturbation calculation for the point detector (Tally 5) problem. A benchmark MCNP model was designed to test the modified MCNP5 perturbation code. The perturbation result calculated by the modified code was compared to the result of original MCNP5 Tally4 calculations and direct calculations. Very good agreement was observed. The modified MCNP5 perturbation code was utilized to perform sensitivity analysis of the SDT experiment which helped to optimize the experimental design.

Three different graphite thermal neutron scattering cross section libraries were used in the MCNP5 code to simulate the SDT experiment. The first is the ENDF/B-VI library which is currently used in the latest MCNP5 code. The second is the NCSU library which was developed by using Ab

Initio (i.e. first principle) method [7]. The last is the NCSU-1P library generated by relaxing the Incoherent Approximation that was used in the first two libraries. The two later libraries were developed at North Carolina State University in 2006 [7]. Differences in the simulated SDT spectra were not found to be significant compared to the expected uncertainty of the measurement. After analyzing the libraries and SDT simulations, it was concluded that this due to the fact that at thermal energies a major fraction of the differences in cross section is within a small energy band around the incoming neutron energy which could be difficult to observe considering the resolution of the SDT experiment.

However, the graphite used in the SDT experiment is reactor grade graphite while the three graphite thermal neutron scattering cross section libraries assume crystalline graphite. Furthermore, after performing a slow neutron transmission experiment for different type of graphite samples at NIST, it was found that the thermal neutron inelastic scattering cross section depends on the type of the graphite sample. Reactor grade graphite has a different inelastic cross section compared to crystalline graphite (pyrolytic graphite). This can be explained by noting that reactor grade graphite is a two-phase material which contains graphite crystals and amorphous-like carbon binders.

The Slowing-Down-Time experiment of reactor grade graphite was performed at room temperature. Measurements were taken by using different type of detectors at different locations. The measured slowing-down-time spectra contained information in the energy range above the Bragg-cutoff energy. After grouping into equal log time bins, the measured data were compared to the MCNP simulations directly. The fast neutron region in the measured time spectrum was

utilized to normalize the MCNP simulation, by assuming that the free atom cross section library is correct. Below 1eV, the measurements show a significant difference from the MCNP simulations which were based on the graphite ENDF/B-VI library. The disagreements can not be explained by any systematic bias or statistical error in the measurement. It's concluded that the disagreement is caused by the graphite thermal neutron cross section library used in the MCNP simulations. However, by including the effect of binder graphite in the simulation (as a 10% weight factor), the results showed an improved agreement with the experimental SDT data.

In the slow neutron transmission experiment at NIST, the total cross section was measured for the neutrons with energy around 1meV. This neutron energy is less than the graphite Bragg-cutoff energy, therefore elastic scattering is not allowed. The total cross section is equal to the inelastic scattering cross section (the absorption cross section is extremely small). At this energy, the measured neutron total cross section is 0.61±0.05 barn for reactor grade graphite and 0.41±0.05 barn for pyrolytic graphite (crystalline). These results confirmed that the two phase reactor grade graphite is significantly different from the crystalline graphite used in the libraries.

5.2 Future work

An accurate thermal neutron scattering cross section library for binder carbon needs to be developed and needs to be benchmarked by the measurements in this work. The Slowing-Down-Time experiment at high temperatures (1000 °C) needs to be carried out. The setup of the high temperature measurement at Oak Ridge National Lab is ready. However execution still awaits final maintenance of ORELA.

In terms of the transmission experiment at NIST, the measurement error can be improved. The statistical errors on the result are coming from two major sources. One is the statistical error of the detector counting; the other is errors on the reference neutron cross-section for the energy above the Bragg cutoff. To improve the statistic, one can measure the transmission by using the Time-Of-Flight method for over 12 hours per case. In this way, the non-0.89 nm neutron correction can be omitted. In case of graphite foam, measurement can be taken by using a thicker sample to increase attenuation and enhance signal.

References

[1] J. A. Lake, "Foundations for the fourth generation nuclear power", *Nuclear energy*, 2001 vol **40** issue 3 pg153

[2] U.S. DOE Nuclear Energy Research Advisory Committee and Generation IV International Forum, "A Technology Roadmap for Generation IV Nuclear Energy Systems: Executive Summary" March 2003

[3] E. Fermi, "The Development of the first chain reaction pile". *Proceedings of the American Philosophy Society* **90**: 20-24, 1946

[4] J. Chen, "On-Line Interrogation of Pebble Bed Reactor Fuel Using Passive Gamma-Ray Spectrometry", Ph.D. thesis, University of Cincinnati, 2004

[5] W. M. Stacey, "Nuclear Reactor Physics", Wiley-Interscience Publication, 2001

[6] Department of Nuclear Engineering, MIT, "Pebble Dynamics in PBMR: Experiments and Modeling", Spring, 2002.

[7] I.I. Al-Qasir, "Thermal Neutron Scattering in Graphite," Ph.D. dissertation, North Carolina State University 2007.

[8] J. J. Duderstadt, L. J. Hamilton "Nuclear Reactor Analysis," 1976, John Wiley&Sons, INC.

[9] R. E. Nightingale, "Nuclear Graphite", Academic Press, 1962

[10]C. L. Mantell, "Carbon and Graphite Handbook," Interscience Publishers, New York, 1986

[11]J. M. Hutcheon, "Modern Aspects of Graphite Technology," ed. L.C.F. Blackman, Academic Press, London, 1970, pp.49-78.

[12]S. Ragan and H. Marsh, "Review: science and technology of graphite manufacture," *J. Mater. Sci.* 1983, **18**, 3161-3176

[13] ENDF/B-VI libraries in MCNP5 code

[14] R. E. MacFarlane, “New Thermal Neutron Scattering Files for ENDF/B-VI, Release 2”, LA-12639-MS, Los Alamos National Laboratory (1994).

[15]F.C. Difilippo, J.P. Renier, " Effects of the Laurent and Taylor expansions on the calculations of the thermal neutrons inelastic scattering cross sections for crystalline moderators," *Annals of Nuclear Energy* **32** (2005) 1323–1336.

[16] A. I. Hawari, B. W. Wehring, H. R. Radulescu, and N. M. Abdurrahman, “Feasibility of using a graphite slowing-down-time spectrometer in the nondestructive assay of nuclear materials,” *Nuclear Instruments and Methods in Physics Research*, A**422** (1999) 846-851

[17] A.A. Bergman, et al., “A neutron spectrometer based on measuring the slowing-down-time of neutrons in lead,” *Proc. Int. Conf. Peaceful Uses of Atomic energy*, Vol. **4**, 1955, pp.135–146.

[18] H. Krinninger *et al.*. *Nucl. Instr. and Meth.* **73** (1969), p. 13.

[19] H. Krinninger *et al.*. *Nucl. Instr. and Meth.* **117** (1974), p. 61.

[20] M. Sawan and R.W. Conn. *Nucl. Sci. Eng.* **54** (1974), p. 127.

[21] N.M. Abdurrahman *et al.*. *Nucl. Sci. Eng.* **115** (1993), p. 279.

[22] F. Maekawa and Y. Oyama. *Nucl. Instr. and Meth. A* **372** (1996), p. 262.

[23] F. Maekawa and Y. Oyama. *Nucl. Sci. Eng. A* **125** (1997), p. 205.

[24] K. H. Beckurts and K. Wirtz, “Neutron Physics”, Springer-Verlag, 1964

[25] A. I. Hawari, et al, “Monte Carlo Assessment of Time Dependent Spectral Indexes for Benchmarking Neutron Transport in Iron” *Proc. of ISRD*, Brussals Belgium 2002

[26] D. E. Parks, J. R. Beyster, and N. F. Wikner “Thermal neutron spectra in graphite”, *Nucl. Sci. Eng.* **13**, 306-324 (1962)

[27] K. H. Guber, et al., "Fission, Total and Neutron Capture Cross Section Measurements at

ORELA for 233-U, 27-Al and Natural Chlorine," pp. 1726-29, Vol. 2, in *Proc. Intnatl. Conf Phys. of Nucl. Sci. & Tech*, Long Island, NY, (October 1998).

[28] K. H. Guber, L. C. Leal, R. O. Sayer, R. R. Spencer, P. E. Koheler, T. E. Valentine, H. Derrien, and J. A. Harver, "Neutron Cross Section Measurements for Light Elements at ORELA and Their Application in Nuclear Criticality and Astrophysics," Proceedings of the Bologna 2000 – Structure of the Nucleus at the Dawn of the Century, Bologna, Italy, 2000.

[29]J A. Harvey, "The keV neutron total cross section measurements at ORELA" AEC Natl. Topical Meeting on New Develop., Reactor Phys. and Shielding, Book 2 p 1075-1086 (SEE N74-11480 02-22); United States; 1972

[30] ORELA http://www.phy.ornl.gov/orela/orela.html/.

[31] S. Raman, private communication, Physics Division, Oak Ridge National Laboratory (2002).

[32] X-5 Monte Carlo Team, "MCNP – A General Monte Carlo N–Particle Transport Code, Version 4C," LA-UR-03-1987, Los Alamos National Laboratory (2003).

[33] M. C. G. Hall, "Cross-Section Adjustment with Monte Carlo Sensitivities: Application to the Winfrith Iron Benchmark", *Nucl. Sci. Eng.*, **81**, 423 (1982)

[34] G. W. McKinney, "A Monte Carlo(MCNP) Sensitivity Code Development and Application," MSc Thesis, University of Washington (1984)

[35] R. L. Perel, "Monte Carlo Calculation of Point-Detector Sensitivities to Material Parameters", *Nucl. Sci. Eng.*, **124**, 197-209 (1996)

[36] http://www.yokogawa.com/daq/mv/daq-mv_01.htm

[37] http://www.ni.com/labview/

[38] http://www.fieldpoint.net/

[39] http://www.ansys.com

[40] R. E. Macfarlane, and D. W. Muir, "The NJOY Nuclear Data Processing System, Version 91," LA-12740-MS, Los Alamos National Laboratory (1994).

[41] J. A. Young, J. U. Koppel, *J. Chem. Phys.*, **42**, 357 (1965).

[42] A. I. Hawari, I.I. Al-Qasir, V.H. Gillette, B. H. Wehring, T. Zhou, "*Ab initio* generation of thermal neutron scattering cross sections," Proceedings of the PHYSOR 2004: The Physics of Fuel Cycles and Advanced Nuclear Systems - Global Developments, p 551-560 (2004).

[43] D. E. Parks et al., "SLow Neutron Scattering and Thermalizations," Benjamin (1970)

[44] C.E.H. Mattoni, C.P. Adams, K.J. Alvine, J.M. Doyle, S.N. Dzhosyuk, R. Golub, E.Korobkina, D.N. McKinsey, A.K. Thompson, L. Yang, H. Zabel, P.R. Huffman, "A long wavelength neutron monochromator for superthermal production of ultracold neutrons," *Pysica B*, **344**, 343-357 (2004).

[45] R. Williams, http://rrdjazz.nist.gov/coldgains.

[46] J. S. Nico, M. Arif, M. S. Dewey, T. R. Gentile, and D. M. Gilliam, P. R. Huffman, D. L. Jacobson and A. K. Thompson, "The Fundamental Neutron Physics Facilities at NIST," *J. Res. Natl. Inst. Stand. Technol.* **110**, 137-144 (2005)

[47] P. R. Huffman, private communication, Department of Physics, North Carolina State University.

[48] F. Sanchez-Bajo and F. L. Cumbrera, "The Use of the Pseudo-Voigt Function in the Variance Method of X-ray Line-Broadening Analysis", *J. Appl. Cryst.* (1997). **30**, 427-430

[49] P. R. Bevington and D. K. Robinson, "Data Reduction and Error Analysis for the Physical Sciences", WCB/McGraw-Hill, 1992

[50] D. J. Hughes and R. B. Schwartz, "Neutron Cross Section," BNL 325, Brookhaven National Laboratory, Upton, New York

[51] A. Steyerl and W. D. Trustedt, “Experiments with a Neutron Bottle,” *Z. Physik*, **267**, 379-388 (1974).

[52] Shamasandar, Ph.D. Thesis, Georgia Institute of Technology, 1974

[53] R. J. Weiss, *Phys. Rev.* **83**, 379-89, 1951

[54] A J Allen and D K Ross “The effects of multiple refraction on cold neutron radiographs of ferromagnetic materials and application to measurement of grain size”, *J. Phys. D: Appl. Phys.*, **17**(1984) 99-107

[55] G. E. Bacon “Neutron Diffraction”, Clarendon Press . Oxford, 1975

[56] A. J. C. Wilson “Refraction Broadening in Powder Diffractometry”, 1962 *Proc. Phys. Soc.* **80** 303

[57] E. P. Barrett, L. G. Joyner and P. P. Halenda, *ibid.*, **73**, 363 (1951)

[58] C. N. Spalaris, “The Micropore Structure of Artificial Graphite”, *J. Phys. Chem.*, **60**:1480-1483 (1956)

[59] H.L. Ritter and L.C. Drake, “Pore-Size Distribution in Porous Materials-Pressure Porosimeter and Determination of Complete Macropore-Size Distributions,” *Ind. Eng. Chem., Anal. Ed.*, **17**: 782-786 (1945)

[60] W.P. Eatherly et al., “Physical Properties of Graphite Materials for Special Nuclear Applications,” *Proceeding of the Second United Nations International Conference on the Peaceful Uses of Atomic Energy*, Geneva, 1958, Vol. **7**, pp. 389-401, United Nations, New York, 1959

[61] J. Hove, and A. Smith, *Phys. Rev.*, **104**, 892(1956)

[62] M. Iizumi and S. Ayao, "Total Cross Section of Glassy Carbon from 0.001to 0.01eV," *J. Nuc. Sci. Tech.* **5**, p649 (1968)

[63]http://www.detectors.saint-gobain.com/Media/Documents/S0000000000000001004/SGC%2

0Glass%20Scintillator%20Data%20Sheet%200105.pdf

[64]http://www.detectors.saint-gobain.com/Media/Documents/S0000000000000001004/SGC%20BC702%20DataSheet%200105.pdf

[65] K.A.Blackmon, private communication, Saint-Gobain Crystals and Detector.

[66] C. Z. Wang and K. M. Ho, "Structure, dynamics, and electronic properties of diamondlike amorphous carbon," *Phys. Rev. Lett.* **71**, 1184 (1993)

[67] P. A. Egelstaff, "Thermal neutron scattering," London, New York, Academic Press, 1965.

Appendix

Appendix

Appendix A. Reactor Grade Graphite Elemental concentration analysis

SHIVA TECHNOLOGIES
6707 Brooklawn Parkway
Syracuse, New York 13211

GDMS
ANALYTICAL REPORT

Telephone (315)431-9900
FAX (315) 431-9800
E-mail info@shivatec.com

Customer: **North Carolina State University** *P.O.#*
Date: 8-Dec-03 *Job #* UM4083

Customer ID: **Graphite**
reactorgradegraphite *Shiva ID:* U031203007

Element	Concentration [ppm wt]	Element	Concentration [ppm wt]
Li	0.63	Ag	< 0.1
Be	< 0.005	Cd	< 0.1
B	0.22	In	< 0.1
C	Matrix	Sn	< 0.01
F	< 0.5	Sb	< 0.01
Na	0.39	Te	< 0.01
Mg	< 0.05	I	< 0.01
Al	0.72	Cs	< 0.01
Si	34	Ba	< 0.01
P	0.44	La	< 0.01
S	35	Ce	< 0.01
Cl	0.89	Pr	< 0.01
K	0.4	Nd	< 0.01
Ca	14	Sm	< 0.01
Sc	< 0.01	Eu	< 0.01
Ti	0.94	Gd	< 0.01
V	15	Tb	< 0.01
Cr	< 0.1	Dy	< 0.01
Mn	0.007	Ho	< 0.01
Fe	1.5	Er	< 0.01
Co	< 0.005	Tm	< 0.01
Ni	0.13	Yb	< 0.01
Cu	< 0.05	Lu	< 0.01
Zn	< 0.1	Hf	< 0.01
Ga	< 0.1	Ta	< 5
Ge	< 0.1	W	< 0.01
As	< 0.1	Re	< 0.05
Se	< 0.1	Os	< 0.01
Br	< 0.1	Ir	< 0.01
Rb	< 0.01	Pt	< 0.01
Sr	0.29	Au	< 0.05
Y	< 0.05	Hg	< 0.5
Zr	0.02	Tl	< 0.01
Nb	< 0.01	Pb	< 0.01
Mo	< 0.05	Bi	< 0.01
Ru	< 0.05	Th	< 0.005
Rh	< 0.05	U	< 0.005
Pd	< 0.05		

Appendix B. Ansys input file for the heat transfer calculation

```
/PREP7
!*
ET,1,SOLID90
!*
BLOCK,-0.35,0.35,-0.35,0.35,-0.35,0.35,          !graphite pile
BLOCK,-0.4,0.4,-0.4,0.4,-0.4,0.4,                !gap
BLOCK,-0.456,0.456,-0.4,0.456,-0.456,0.456,      !heater
BLOCK,-0.576,0.576,-0.576,0.576,-0.576,0.576,    !insulation
BLOCK,-0.576,0.576,-0.576,-0.4,-0.576,0.576,     !bottom insulation
BLOCK,-0.35,-0.27,-0.576,-0.35,-0.35,0.35,       !support brick
BLOCK,-0.04,0.04,-0.576,-0.35,-0.35,0.35,        !support brick
BLOCK,0.27,0.35,-0.576,-0.35,-0.35,0.35,         !support brick
BLOCK,-0.35,0.35,-0.456,-0.35,-0.35,0.35,        !bottom heater
BLOCK,-0.58,0.58,-0.58,0.58,-0.58,0.58,          !Al
BLOCK,-0.834,0.834,-0.834,0.834,-0.834,0.834,    !AIR
BLOCK,-0.86,0.86,-0.86,0.86,-0.86,0.86,          !polyethylene
vovlap,all
vdele,19
vdele,20
vdele,29
TREF,300
MPTEMP,,,,,,,,
```

MPTEMP,1,300

MPDATA,DENS,1,,1700

MPTEMP,,,,,,,,

MPTEMP,1,300

MPTEMP,2,500

MPTEMP,3,800

MPTEMP,4,1400

MPDATA,C,1,,710

MPDATA,C,1,,1250

MPDATA,C,1,,1670

MPDATA,C,1,,1880

MPTEMP,,,,,,,,

MPTEMP,1,300

MPTEMP,2,500

MPTEMP,3,800

MPTEMP,4,1400

MPDATA,KXX,1,,156

MPDATA,KXX,1,,118

MPDATA,KXX,1,,73

MPDATA,KXX,1,,36

MPTEMP,,,,,,,,

MPTEMP,1,300

MPDATA,KXX,2,,0.72

```
MPTEMP,,,,,,,,
MPTEMP,1,300
MPDATA,C,2,,1047
MPTEMP,,,,,,,,
MPTEMP,1,300
MPDATA,DENS,2,,2179
MPTEMP,,,,,,,,
MPTEMP,1,300
MPDATA,KXX,3,,205
MPTEMP,,,,,,,,
MPTEMP,1,300
MPDATA,C,3,,900
MPTEMP,,,,,,,,
MPTEMP,1,300
MPDATA,DENS,3,,2700
MPTEMP,,,,,,,,
MPTEMP,1,533.15
MPTEMP,2,1088.706
MPTEMP,3,1644.261
MPDATA,KXX,4,,1.124977533
MPDATA,KXX,4,,1.081709166
MPDATA,KXX,4,,1.139400322
MPTEMP,,,,,,,,
```

MPTEMP,1,300

MPDATA,C,4,,1047

MPTEMP,,,,,,,,

MPTEMP,1,300

MPDATA,DENS,4,,2274.6218

MPTEMP,,,,,,,,

MPTEMP,1,300

MPDATA,DENS,5,,496.57

MPTEMP,,,,,,,,

MPTEMP,1,533.15

MPTEMP,2,810.928

MPTEMP,3,1088.706

MPTEMP,4,1366.483

MPDATA,KXX,5,,0.13

MPDATA,KXX,5,,0.17

MPDATA,KXX,5,,0.21

MPDATA,KXX,5,,0.25

MPTEMP,,,,,,,,

MPTEMP,1,300

MPDATA,C,5,,1047

MPTEMP,,,,,,,,

MPTEMP,1,300

MPDATA,C,6,,1047

MPTEMP,,,,,,,,

MPTEMP,1,533.15

MPTEMP,2,810.928

MPTEMP,3,1088.706

MPTEMP,4,1366.483

MPDATA,KXX,6,,0.06

MPDATA,KXX,6,,0.10

MPDATA,KXX,6,,0.15

MPDATA,KXX,6,,0.22

MPTEMP,,,,,,,,

MPTEMP,1,300

MPDATA,DENS,6,,272.314

MPTEMP,,,,,,,,

MPTEMP,1,300

MPDATA,DENS,7,,1.2

MPTEMP,,,,,,,,

MPTEMP,1,300

MPDATA,C,7,,720

MPTEMP,,,,,,,,

MPTEMP,1,300

MPDATA,KXX,7,,0.026

MPTEMP,,,,,,,,

MPTEMP,1,300

```
MPDATA,DENS,8,,950
MPTEMP,,,,,,,,
MPTEMP,1,300
MPDATA,C,8,,1850
MPTEMP,,,,,,,,
MPTEMP,1,300
MPDATA,KXX,8,,1
!
SMRT,3                          !graphite pile
MSHAPE,1,3D
MSHKEY,0
VMESH,26
!
SMRT,6
TYPE,1                          !Set element type attribute pointer to 1
MAT,2                           !Set element material attribute pointer to 2
REAL                            !Set element real const set attribute pointer
ESYS,0                          !Set the element coord sys attribute pointer
VSEL,S,VOLU,,13,18
VSEL,A,VOLU,,21,22
VSEL,A,VOLU,,24
VMESH,ALL                       !support brick
VSEL,ALL
```

```
!
TYPE,1                    !Set element type attribute pointer to 1
MAT,3                     !Set element material attribute pointer to 2
REAL                      !Set element real const set attribute pointer
ESYS,0                    !Set the element coord sys attribute pointer
VMESH,33                    !Al
!
SMRT,6
TYPE,1
MAT,4
REAL
ESYS,0
VSEL,S,VOLU,,27
VSEL,A,VOLU,,23
VSEL,A,VOLU,,25
VMESH,ALL                   !heater
VSEL,ALL
!
TYPE,1
MAT,5
REAL
ESYS,0
VMESH,30                    !bottom insulation
```

```
!
TYPE,1
MAT,6
REAL
ESYS,0
VMESH,28                !wall and ceiling insulation
!
TYPE,1
MAT,7
REAL
ESYS,0
VMESH,31                !air
!
SMRT,6
TYPE,1
MAT,8
REAL
ESYS,0
VMESH,32                !polyethylene
!
!
!SFA,67,1,CONV,12,,300   !Apply film coefficient and bulk temperature
!SFA,68,1,CONV,12,,300
```

```
!SFA,69,1,CONV,12,,300
!SFA,70,1,CONV,12,,300
!SFA,71,1,CONV,12,,300
!SFA,72,1,CONV,12,,300
!
FINISH
/SOL
!*
ANTYPE,4
!*
TRNOPT,FULL
LUMPM,0
!*
SOLCONTROL,ON,0,
!*
STEF,0.56704E-07
TOFFST,0
RADOPT,0.5,0.1E-01,0,1000,0.5,0.5
SPCTEMP,1,300
!
TUNIF,300
!
ASEL,S,AREA,,4,6
```

```
ASEL,A,AREA,,131,132
ASEL,A,AREA,,105
ASEL,A,AREA,,109
SFA,ALL, ,RDSF,0.85,1,
ASEL,ALL
ASEL,S,AREA,,7,8
ASEL,A,AREA,,10,12
ASEL,A,AREA,,108
ASEL,A,AREA,,112
!DA,ALL,TEMP,1200
SFA,ALL, ,RDSF,0.95,1,
ASEL,ALL
!
VSEL,S,VOLU,,27
VSEL,A,VOLU,,23
VSEL,A,VOLU,,25
BFV,ALL,HGEN,450000                    !heater
VSEL,ALL
!
TIME,36000
AUTOTS,-1
DELTIM,300,300,700,1
KBC,1
```

```
!*
TSRES,ERASE
!
OUTRES,BASIC,ALL,                    !Write to file at every step
SAVE
```

Appendix C. The code for grouping experimental data into equal log time bins

The code was written in MBA (Microsoft Basic Application) as a macro, which can be called in a Microsoft Excel file. To use the code, create a Microsoft Excel file and arrange data in the format as follow:

- First column is channel number in MultiChannel Scaler, from 1 to 8192. First channel appear in the third row.
- Second column is experimental time bins, which is equal to the dwell time (0.9us) times the channel number.
- Third column is experimental values in each channel.
- Fourth column is equal log time bins, into which the experimental data will be grouped.
- And fifth column will contain the grouped data after running the macro code.

```
Sub TimeBinCollaps()
'
' TimeBinCollaps Macro
' Macro recorded 1/18/2005 by Tong Zhou
'
' Keyboard Shortcut: Ctrl+t
'
    Dim n, m As Long
```

```
    Dim i As Long
    Dim j As Long
    Dim data, LowerBound As Double
    Dim LinearBin As Double
    Dim a, b As Long


'number of channel
    n = 8192
'number of Collapsed Time Bins
    m = 100
'width of the linear time bin
    LinearBin = 0.0000009

    data = 0


    For i = 3 To m + 3

        a = Int(Worksheets("TimeBin").Cells(i - 1, 4).Value / LinearBin) + 2
        b = Int(Worksheets("TimeBin").Cells(i, 4).Value / LinearBin) + 2
        If b > 8192 + 2 Then
        Exit For
```

```
        End If


        If a = b Then
            Worksheets("TimeBin").Cells(i, 5).Value = Worksheets("TimeBin").Cells(a + 1,
3).Value * (Worksheets("TimeBin").Cells(i, 4).Value - Worksheets("TimeBin").Cells(i - 1,
4).Value) / (Worksheets("TimeBin").Cells(a + 1, 2).Value - Worksheets("TimeBin").Cells(a,
2).Value)
        Else
            data = Worksheets("TimeBin").Cells(a + 1, 3).Value *
(Worksheets("TimeBin").Cells(a + 1, 2).Value - Worksheets("TimeBin").Cells(i - 1, 4).Value) /
(Worksheets("TimeBin").Cells(a + 1, 2).Value - Worksheets("TimeBin").Cells(a, 2).Value)
            If b > a + 1 Then
            For j = a + 2 To b
                data = data + Worksheets("TimeBin").Cells(j, 3).Value
            Next j
            End If
            data = data + Worksheets("TimeBin").Cells(b + 1, 3).Value *
(Worksheets("TimeBin").Cells(i, 4).Value - Worksheets("TimeBin").Cells(b, 2).Value) /
(Worksheets("TimeBin").Cells(b + 1, 2).Value - Worksheets("TimeBin").Cells(b, 2).Value)
            Worksheets("TimeBin").Cells(i, 5).Value = data
        End If
    Next i
End Sub
```

Appendix D. The code for reading flux tally from an MCNP output file and calculate the average energies at each moment

This code was written in MBA (Microsoft Basic Application) as a macro, which can be called in a Microsoft Excel file. To use the code to read flux tally from a MCNP output file and calculate average neutron energies, do the following:

- In an MCNP input file, specify neutron energy bins from 10-9 MeV to 20 MeV with equal log energy bins and total bin number of 103. Specify time bins from 10 shakes to 106 shakes with equal log time bins and total bin number of 100. Tally neutron flux in the detector as a function of energy and time.
- Copy the tallied neutron flux data block from the MCNP output file, and save it as a new txt file.
- Open the saved txt file by Microsoft Excel, name the sheet as "tally5". Create a new sheet with name "total".
- Copy the time bins into the first row of "total" sheet, starting from the second column. Copy the energy bins into the first column of "total" sheet, starting from the third row.
- Run "readflux" macro to get the tallied neutron flux in "total" sheet.
- In the row 107, calculate the total flux at each moment by equation "SUM(B3:B106), SUM(C3:C106), …"
- Run "average_E" macro to get the average neutron energies at each moment in the row 108 of "total" sheet.

```
Sub readflux()
'
```

```
' readflux Macro
' Macro recorded 2/12/2003 by Tong Zhou
'
' Keyboard Shortcut: Ctrl+r
'
    Dim k As Long
    Dim i As Long
    Dim j As Long
    Dim NE, NT1, NT2 As Long

' Number of energy bins
    NE = 104
' Number of time bins is equal to NT1 times NT2
    NT1 = 20
    NT2 = 5

    For i = 1 To NT1
        For j = 3 To NE + 2
            For k = 1 To NT2
                Worksheets("total").Cells(j, 5 * (i - 1) + k + 1).Value =
Worksheets("tally5").Cells(108 * (i - 1) + j, k * 2).Value
            Next k
        Next j
```

```
    Next i


End Sub
Sub average_E()
'
' average_E Macro
' Macro recorded 2/12/2003 by Tong Zhou
'
' Keyboard Shortcut: Ctrl+e
'
    Dim i As Long
    Dim j As Long
    Dim temp As Double
    Dim NE, NT As Long
' Number of energy bins
    NE = 104
' Number of time bins is equal to NT1 times NT2
    NT = 101


    For i = 2 To NT + 1
        temp = 0
        For j = 3 To NE + 2
        temp = temp + Worksheets("total").Cells(j, 1).Value * Worksheets("total").Cells(j,
```

```
i).Value
        Next j
        If temp = 0 Then
            Worksheets("total").Cells(108, i).Value = 0
        Else
            Worksheets("total").Cells(108, i).Value = temp / Worksheets("total").Cells(107,
i).Value
        End If
    Next i
End Sub
```

Appendix E. The formatting of the thermal neutron scattering cross section libraries in MCNP5 code

The thermal neutron scattering cross section libraries in MCNP5 code are called thermal S(α,β) tables or thermal treatment. The first 12 records (lines) contain miscellaneous information [32]. After that, there are four data blocks in the table.

- ITIE Block: contains the energy-dependent inelastic scattering cross sections. The first record is the number of inelastic energies. The following records are the energy bins. The corresponding inelastic cross sections are following the energy bins.
- ITCE Block: contains the energy-dependent elastic scattering cross sections. The first record is the number of elastic energies.
- ITXE Block: contains couples energy/angle distributions for inelastic scattering. For every incident energies in the ITIE Block, there are number of equally-likely outgoing

energies. And each of outgoing energy is followed by number of equally-likely outgoing angular cosine value. The number of outgoing energies and cosines are 64 and 16 by default in MCNP5 libraries. However, in this work all the graphite thermal neutron libraries are generated with 256 outgoing energies and 16 angular cosine bins.

- ITCA Block: contains angular distributions for elastic scattering.

Refer the reference number 32 for more details.